

FIB PATTERNED TEMPLATES FOR GUIDED NANOSTRUCUTRE FORMATION

by

Hao Wang

B.E., Tsinghua University, 2005

M.S., Tsinghua University, 2007

Submitted to the Graduate Faculty of

Swanson School of Engineering in partial fulfillment

of the requirements for the degree of

Doctor of Philosophy

University of Pittsburgh

2013

UNIVERSITY OF PITTSBURGH
SWANSON SCHOOL OF ENGINEERING

This dissertation was presented

by

Hao Wang

It was defended on

March 1, 2013

and approved by

Guangyong Li, PhD, Assistant Professor, Department of Electrical and Computer Engineering

Jung-Kun Lee, PhD, Assistant Professor, Department of Mechanical Engineering and

Materials Science

Qing-Ming Wang, PhD, Professor, Department of Mechanical Engineering and Materials

Science

Dissertation Director: John A. Barnard, PhD, Professor, Department of Mechanical

Engineering and Materials Science

Copyright © by Hao Wang

2013

FIB PATTERNED TEMPLATES FOR GUIDED NANOSTRUCTURE FORMATION

Hao Wang, PhD

University of Pittsburgh, 2013

There are many factors that limit significant advances in device technology, including the ability to arrange materials at shrinking dimensions and the ability to successfully integrate new materials having better properties with silicon. Methods for self-assembly of quantum dots are greatly desired for new devices which have smaller sizes, lower energy consumption, higher performance, and new functionality. To create such devices, a patterning method must be used that can arrange quantum dots at the appropriate length scales. A focused ion beam (FIB) is one method of laterally arranging nanosized islands of dissimilar materials on silicon by creating template patterns on the Si substrate with nanoscale resolution. The templates utilize surface topography features or chemical/compositional variations in the near surface region to promote self-assembly of nanostructures. During FIB milling, surface topography is created as material removed, however, implanted Ga is added which can form clusters or nanocrystals upon heating.^{1,2} Both processes are of potential interest for lateral positioning of nanostructures.

For example, if large enough amounts of Ga are implanted near the surface, Ga surface islands could result upon annealing with the potential to be converted to Ga-based compounds, such as GaN, on Si through chemical reactions. GaN is a direct band gap material and of interest LED and photodetectors.³⁻⁶ However, growth of GaN directly on silicon, the most technologically important substrate, is a challenge due to the thermal expansion coefficient mismatch between the GaN and Si substrate.

We have used two approaches in our studies. The first approach would be to understand the conditions that may induce Ga nucleation on the surface of FIB patterned Si substrates upon annealing. In the second case, the as-formed patterns could be used as topography templates. The templates could be potentially used to influence the growth of strain-induced nanoislands that form when strained SiGe is deposited on Si substrates. In our initial experiments, we have explored ex-situ FIB patterning and magnetron sputtering to deposit SiGe on FIB patterned Si substrates. The goal of these experiments is to understanding how the FIB patterning conditions and SiGe deposition conditions influence surface island formation in this system.⁷

TABLE OF CONTENTS

TABLE OF CONTENTS	VI
LIST OF TABLES	IX
LIST OF FIGURES	X
PREFACE.....	X
1.0 INTRODUCTION.....	1
1.1 MOTIVATION.....	1
1.2 BACKGROUND.....	3
1.2.1 Methods of producing quantum dots	3
1.2.2 Ga and GaN quantum dots	4
1.2.3 Nucleation of Ga clusters.....	6
1.2.4 Deposition of SiGe on Si substrates	8
1.3 APPLICATION OF GAN.....	11
1.3.1 High-efficiency light-emitting diodes (LEDs)	11
1.3.2 Short wavelength laser diodes (LDs)	12
1.3.3 UV Photo-detectors	13
1.4 SIGE QUANTUM DOTS.....	14
1.5 GERMANIUM QUANTUM DOTS.....	16
2.0 EXPERIMENTAL TECHNIQUES	18
2.1 FOCUSED ION BEAM (FIB)	19
2.2 FIB PATTERNING PROCESS	21

2.3	SUBSTRATE CLEANING PROCEDURES	24
2.4	PHYSICAL VAPOR DEPOSITION (MAGNETRON SPUTTERING).....	27
2.5	REFLECTION HIGH-ENERGY ELECTRON DIFFRACTION (RHEED)...	30
2.6	ATOMIC FORCE MICROSCOPY	32
2.7	TRANSMISSION ELECTRON MICROSCOPY.....	34
2.8	TEM SAMPLE PREPARATION.....	36
2.8.1	TEM Plan View Samples Created by Mechanical Thinning and Chemical Etching	36
2.8.2	Nonporous Amorphous Silicon Membrane	38
2.8.3	TEM Plan View Samples Created by FIB	39
3.0	GALLIUM NANOISLAND FORMATION.....	40
3.1	OVERALL EXPERIMENTAL DETAILS.....	40
3.2	GALLIUM TEMPLATES USING DIFFERENT DOSE	42
3.3	GALLIUM TEMPLATES USING DIFFERENT TRENCH WIDTH	44
3.4	GALLIUM TEMPLATES PATTERNED ON AMORPHOUS SI TEM WINDOWS	46
3.5	GALLIUM TEMPLATES WITH SQUARE SHAPE.....	50
3.6	EFFECT OF ACCELERATING DOSE IN FIB PATTERNING	59
3.7	DOT ARRAYS GALLIUM TEMPLATES ON SI SUBSTRATE.....	63
3.8	CONCLUSIONS FOR THE GALLIUM NANODOTS FORMATION	64
4.0	NITRIDATION PROCESS OF GALLIUM NANOISLANDS	66
4.1	NITRIDATION PARAMETERS.....	67
4.2	RESULTS WITH DIFFERENT NITROGEN/ARGON RATIO.....	68
4.2.1	N ₂ /Ar gas ratios as 1:1	68
4.2.2	N ₂ /Ar gas ratios as 2:1 and 1:2.....	72
4.3	CONCLUSION FOR GALLIUM NITRIDE FORMATION.....	75

5.0	SIGE QUANTUM DOTS FORMATION.....	76
5.1	HIGHLIGHTS IN SILICON-GEMANIUM QUANTUM DOTS FORMATION PROCEUDES	77
5.2	SILICON BUFFER GROWTH	79
5.3	SIGE QUANTUM DOTS GROWTH ON SI WAFERS.....	81
5.3.1	10 nm Si_{0.7}Ge_{0.3} growth on 6.5 nm Si buffer layer at 500 °C and 0.5 Å/s..	81
	5.3.1.1 10nm Si_{0.7}Ge_{0.3} growth on 6.5nm Si buffer layer at different conditions.....	84
5.3.2	RHEED results for 10nm Si_{0.7}Ge_{0.3} growth on 6.5 nm Si buffer layer at 500 °C and 0.5 Å/s	85
5.4	GROWTH CONDITIONS LEAD TO REFERED QUANTUM DOTS GROWTH.....	88
5.5	GEMANIUM QUANTOM DOTS ON SI SBUSTRATE.....	90
5.6	CONCLUSIONS FOR SIGE NANOISLANDS.....	93
6.0	SUMMARY AND FUTURE WORK.....	95
6.1	SUMMARY OF RESULTS AND CONCLUSIONS.....	95
6.2	FUTURE WORK.....	97
	6.2.1 Formation of Gallium Nitride with different structure and different reaction gas	98
	6.2.2 GaN optical characterization	100
	6.2.3 SiGe and Ge quantum dots growth	100
	APPENDIX A. SI BUFFER LAYER, SIGE, GE GROWTH CONDITIONS	102
	BIBLIOGRAPHY	106

LIST OF TABLES

Table 5.1 Hydrocarbons peak height from RGA data at different temperatures.	79
--	----

LIST OF FIGURES

Figure 1.1 Ga nanodots on SiO ₂ surface fabricated by FIB with different dosages. ²⁹	7
Figure 1.2 AFM 2 μm x 2 μm images of 20 nm Si _{0.7} Ge _{0.3} film grown at 550 °C and 0.9 Å/s on a 7 nm Si buffer layer for patterned region within the FIB array. ¹³	10
Figure 2.1. General experimental procedure in the FIB assisted nanostructure formation.	19
Figure 2.2 Focused Ion Beam System. ⁶⁸	21
Figure 2.3 FIB pattern diagrammatic sketch (no to scale).....	22
Figure 2.4 FIB pattern used for SiGe quantum dots growth.....	23
Figure 2.5 AFM image of FIB dot array pattern Si substrate. Dosage is 3.0 x 10 ¹⁵ /cm ² , the voltage is 30 kV and the beam current is 1 pA.	24
Figure 2.6 Magnetron Sputtering System used to grow all samples.	30
Figure 2.7 Schematic diagram of RHEED used in the research.	31
Figure 2.8 AFM working status.....	33
Figure 2.9 AFM used to characterize all samples.....	34
Figure 2.10 The JEOL JEM-2100F TEM located in the nano fabrication and characterization facility (NFCF), University of Pittsburgh.....	35
Figure 2.11 Fabrication Process of TEM samples.....	38
Figure 2.12 Plan view TEM samples preparation procedure.....	39
Figure 3.1 (a) overview AFM image of trench patterns before annealing. (b) Higher magnification of image of a single trench illustrating lack of topography in bottom of trenches before annealing. Image is of trench in lower left corner of Fig 3.1(a).....	42

- Figure 3.2 AFM image of trenches with different dosage after annealing: (a) $35 \times 10^{15}/\text{cm}^2$, (b) $39 \times 10^{15}/\text{cm}^2$ and (c) $42 \times 10^{15}/\text{cm}^2$ nm, (d) Ga nanodot diameter and height vs. dosage. 43
- Figure 3.3 AFM image of trenches with different width after annealing: (a) 50 nm, (b) 100 nm, (c) 200 nm, (d) 300 nm, (e) Ga nanodot diameter and height vs. trench width. 45
- Figure 3.4 SRIM Monte Carlo simulation result of ions trajectories in Si with an accelerating voltage of 30 kV. Total number of ions is 1400. (a) Transverse view. (b) Ion trajectories. 48
- Figure 3.5 HAADF and HR-TEM images of Ga nanodots on amorphous silicon membrane: (a) HAADF of template, (b) HAADF at higher magnification, (c) HR-TEM of Ga nanodots and (d) HR-TEM of Ga nanodots at higher magnification. 49
- Figure 3.6 (a) AFM $2 \times 2 \mu\text{m}$ image with edges roughly aligned along the $\langle 110 \rangle$ directions for Ga FIB pattern. Accelerating voltage was 30kV and the beam current was 5pA. The total ion dose was 2.9×10^{16} ions/ cm^2 for the $1 \times 1 \mu\text{m}$ patterned square area. (b) $1 \times 1 \mu\text{m}$ milled area after annealing for 1 hour at 600°C . (c) AFM image of the same patterned area after HCl etching. (d) HAADF image of the Ga nanocrystals formed in the patterned area with insert showing selected area diffraction pattern of the same area. (e) HR-TEM image of Ga nanocrystals showing the Ga lattice fringes inset (d)..... 54
- Figure 3.7 (a) AFM $1 \times 1 \mu\text{m}$ image with edges roughly aligned along the $\langle 110 \rangle$ directions for Ga FIB pattern. Accelerating voltage was 30kV and the beam current was 5pA. Total dose was 2.9×10^{16} ions/ cm^2 for the $100 \times 100 \text{ nm}$ patterned square area. (b) $100 \times 100 \text{ nm}$ milled area after annealing for 1 hour at 600°C . (c) $75 \times 75 \text{ nm}$ milled area after annealing for 1 hour at 600°C . (d) Diameters of Ga nanoislands as a function of total ion dose. 56
- Figure 3.8 Schematic of the positions of Ga nanodots. (a) Ga precipitation underneath the surface. (b) Ga nanodots on the Si surface capped with a thin layer of Si. (c) Ga nanodots on the Si surface..... 57
- Figure 3.9 AFM $2 \times 2 \mu\text{m}$ image with edges roughly aligned along the $\langle 110 \rangle$ directions for Ga FIB pattern. Accelerating voltage was 10kV and the beam current was 5pA. Fluence was $2.9 \times 10^{16}/\text{cm}^2$ for the $1 \times 1 \mu\text{m}$ patterned square area. (b) $1 \times 1 \mu\text{m}$ milled area after after annealing for 1 hour at 600°C 60
- Figure 3.10 Depth profile (obtained from AFM scan) of $1 \times 1 \mu\text{m}$ patterned square area before annealing with different accelerating voltage. Total ion dose was 2.9×10^{16} ions/ cm^2 for the $1 \times 1 \mu\text{m}$ patterned square area. 61
- Figure 3.11 SRIM Monte Carlo simulation result of ions trajectories in Si with an accelerating voltage of 30 kV and 10 kV. Total number of ions is 1700..... 62
- Figure 3.12 AFM images of (a) 1 pA beam current, $30 \times 10^{15}/\text{cm}^2$ dosage point mills before and (b) after anneal. The z-scale for both images is 8.5 nm. (c) 10 pA beam current, $60 \times$

10 ¹⁵ /cm ² dosage point mills before and (d) after anneal. The z-scale for both images is 10.2 nm.	64
Figure 4.1 (a) AFM 15 x 15 μm image with edges roughly aligned along the <110> directions for Ga FIB pattern. Accelerating voltage was 30kv and the beam current was 5pA. The total ion dose was 2.9 x 10 ¹⁶ ions/cm ² for the 10 x 10 μm patterned square area. (b) 10 x 10 μm milled area after annealing for 1 hour at 600 °C. (c) AFM image of the same patterned area after exposure to nitrogen plasma with N ₂ /Ar ratio as 1:1 for 5 minutes at 500°C. (d) 1 x 1 μm zoomed in scan in the same area after nitridation process. (e) HR-TEM image of GaN nanocrystals showing the GaN lattice fringes. (f) Selected area diffraction pattern of the same area.	70
Figure 4.2 (a) AFM 15 x 15 μm image for the 10 x 10 μm FIB patterned square area after annealing for 1 hour at 600 °C with edges roughly aligned along the <110> directions. Accelerating voltage was 30kv and the beam current was 5pA. The total ion dose was 2.9 x 10 ¹⁶ ions/cm ² . (b) AFM image of the same patterned area after exposure to nitrogen plasma with N ₂ /Ar ratio as 2:1 for 5 minutes at 500°C. (c) HR-TEM image of GaN nanocrystals showing the GaN lattice fringes. (d) Selected area diffraction pattern of the same area.....	73
Figure 4.3 (a) AFM 15 x 15 μm image for the 10 x 10 μm FIB patterned square area after annealing for 1 hour at 600 °C with edges roughly aligned along the <110> directions. Accelerating voltage was 30kv and the beam current was 5pA. The total ion dose was 2.9 x 10 ¹⁶ ions/cm ² . (b) AFM image of the same patterned area after exposure to nitrogen plasma with N ₂ /Ar ratio as 1:2 for 5 minutes at 500°C. (c) HR-TEM image of GaN nanocrystals showing the GaN lattice fringes. (d) Selected area diffraction pattern of the same area.....	74
Figure 5.1 65 nm Si buffer layer grown at 500 °C.....	80
Figure 5.2 (a)AFM images of 1 x 10 ¹⁵ /cm ² dosage point arrays mills after SiGe alloy growth. (b) Profile data of the quantum dot. The sample's edge is roughly aligned along the <110> direction.	82
Figure 5.3 (a) AFM images of 6 x 10 ¹⁵ /cm ² dosage point arrays mills after SiGe alloy growth. (b) Profile data of the quantum dot. The sample's edge is roughly aligned along the <110> direction.	83
Figure 5.4 (a) AFM images of 20 x 10 ¹⁵ /cm ² dosage point arrays mills after SiGe alloy growth. (b) Profile data of the quantum dot. The sample's edge is roughly aligned along the <110> direction.	84
Figure 5.5 AFM images of 6 x 10 ¹⁵ /cm ² dosage point arrays mills after SiGe alloy growth. (a) SiGe alloy grown at 550 °C with total growth rate of 1 Å/s. (b) SiGe alloy grown at 450 °C with total growth rate of 0.5 Å/s. The sample's edge is roughly aligned along the <110> direction.....	85

Figure 5.6 RHEED results for 10nm Si _{0.7} Ge _{0.3} growth on 6.5 nm Si buffer layer at 500 °C and 0.5 Å/s.	87
Figure 5.7 RHEED results for 10nm Si _{0.7} Ge _{0.3} growth on 1.8 nm Si buffer layer at 550 °C and 1 Å/s.	87
Figure 5.8 AFM 1x1 μm image with edges roughly aligned along the <110> directions for films deposited on substrates patterned at single points using a 1 pA beam current. The 10nm Si _{0.7} Ge _{0.3} were grown on a 6.5nm Si buffer layer at 500°C and 1Å/s. Pattern dosages were (a) 0.5 x 10 ¹⁵ /cm ² . (b) 1 x 10 ¹⁵ /cm ² . (c) 3 x 10 ¹⁵ /cm ² . (d) 6 x 10 ¹⁵ /cm ²	89
Figure 5.9 AFM of Ge quantum dots in un-patterned region.	91
Figure 5.10 Growth of Ge quantum dots in patterned region.	92

PREFACE

I would first like to thank my dissertation advisor Dr. Jennifer L. Gray and Dr. John A. Barnard for giving me the opportunity to work with them over the last four years. It has been a real pleasure and privilege working with Dr. Gray and Dr. Barnard during the course of my doctoral program. I sincerely appreciate all the advice, encouragement, support and the freedom to pursue and explore research from different vantage points. They also provided me with the opportunity to attend various conferences, present our work, which also allowed me to interact with other experts and researchers in my field. These interactions later proved to be quite invaluable in problem solving as I carried out my research. The day to day interactions and the constructive feedback, be it the design of experiments, publishing or presenting work during the progression of my program were enjoyable and in the end proved to be very successful. It was a wonderful experience as they were also my mentor in my capacity as a research assistant the last five years. The knowledge gained through collaborations with other highly respected research groups has been an insightful experience.

I would also like to acknowledge my committee members: Dr. John Barnard, Dr. Jung-Kun Lee, Dr. Guangyong Li and Dr. Qing-Ming Wang, who have helped in the form of collaborations and/or lending their profound technical expertise on the subject. I am also grateful to a number of people who have assisted me in the completion of the project, including Dr. Susheng Tan, Albert Stewart, Michael L. McDonald, Mattew Frances and Cole Van Ormer.

Finally, I would like to thank my family and friends, as they have been supportive in my interest and pursuit of an advanced degree. My parents and my wife have always been extremely supportive of my continuing education. I consider myself quite fortunate to have found wonderful friends both within and outside the University of Pittsburgh who have helped in various ways, professional and otherwise. These include my co-workers Mengjin Yang, Bo Ding, Xiahan Sang. A special note of thanks to Gowtam Atthipalli, Heather Meloy-Gorr, Korrinn Strunk for the delightful interactions and keeping my sanity intact as I successfully finish my doctoral work.

This work was funded by the National Science Foundation (NSF-DMR) under grant number 0906679.

1.0 INTRODUCTION

1.1 MOTIVATION

The ability to produce semiconductor nanostructures such as quantum dots (QDs) at specific locations on a substrate is important for nanoelectronic applications. For quantum dot device applications' development, zero-dimension structures are meaningful because of their discrete energy spectrum; and what is more, because they show genuine few-carrier effects. In order to create such new devices, a patterning method must be used that can arrange quantum dots at the appropriate length scales.⁸⁻¹³ A focused ion beam (FIB) is one method of laterally arranging nanosized islands of dissimilar materials on silicon by creating template patterns directly on the Si substrate with nanoscale resolution. To promote self-assembly of nanostructures, techniques such as surface topography features or chemical/compositional variations are used in the near surface region of these templates. Two changes are taking place simultaneously during the milling process: surface topography is created as material being removed while implanted Ga is added. The implanted Ga can form clusters or nanocrystals when heating.^{11,14} Both processes are of potential interest for lateral positioning of nanostructures.

One possible concern for device applications is the effect of the implanted Ga that is a result of the milling process. Implantation can result in damage to the lattice, unwanted doping of the substrate, and/or nucleation of Ga nanocrystals from the implanted material. On the other

hand, it may also be desirable in some scenarios to take advantage of the implanted material and nucleate nanostructures directly from it. For example, if large enough amounts of Ga are implanted near the surface, Ga surface islands could result upon annealing with the potential to be converted to Ga-based compounds, such as GaN, on Si through chemical reactions. GaN can be used as a direct band gap material; at the same time, it is also a useful component for electrically pumped ultraviolet–blue LEDs(light-emitting diodes), photo detectors, lasers, and possibly used for single photon sources.^{15–18} However, growth of GaN directly on silicon, the most technologically important substrate, is a challenge due to the thermal expansion coefficient mismatch between the GaN and Si substrate.^{19–21}

We have used two approaches in our studies. The first approach would be to understand the conditions that may induce Ga nucleation on the surface of FIB patterned Si substrates upon annealing. In the second case, under low dose FIB patterning conditions, it is presumed that Ga surface nucleation will not happen. Hence, the as-formed patterns could be used as topography templates. The templates could be potentially used to influence or guide the growth of strain-induced nanoislands that form when strained SiGe is deposited on Si substrates. We have explored ex-situ FIB patterning and magnetron sputtering to deposit SiGe on FIB patterned Si substrates in our initial experiments. Sputtering is commonly used in industry for depositing thin films. This method can bring about relatively high quality epitaxial deposition²² and compare to other techniques, it could get higher growth rates than e-beam deposition method at lower temperatures than could be achieved with CVD techniques.²³ The goal of these experiments is to first set up conditions under which epitaxy can be achieved at relatively low growth temperatures using magnetron sputtering under typical high vacuum pressures, and second understands how

surface island formation can be influenced by the FIB patterning conditions and SiGe deposition conditions in this system.

1.2 BACKGROUND

1.2.1 Methods of producing quantum dots

The recent focus of semiconductor quantum dots fabrication is spontaneous 3D (three dimensional) islanding approaches. the quantum dots formation can be achieved in multiple ways.²⁴

The first method need to be mentioned is MBE (Molecular beam epitaxy). It is the low deposition rate (usually lower than 5 Å per second) makes this method so distinguish. These deposition rates allow the films to grow epitaxially but require relatively higher vacuum than other deposition methods to access the same impurity grade.²⁵ The ultra-high vacuum and the low presence of carrier gases could lead to the highest accessible purity of the films. However, the most obvious drawback of MBE is that it's expensive and will need dedicated effort and significant amount of time to maintain such ultra-high vacuum. Moreover, neither the kinetic energy of the atoms nor the growth rate of desired thin film materials can be adjusted.

There are also reports indicated that metal organic vapor phase epitaxy (MOVPE) conditions was used for growing quantum dot arrays in the InGaAs/GaAs system.²⁶ The nanoscale In droplets can form on a GaAs (100) substrate during the decomposition of

trimethylindium (TMI) at temperatures as low as 160–360 °C.²⁶ This lower temperature can make it easier to use plastic or organic substrates for QDs growth. Besides, this is a more economic and energy-saving method if use in industry.

Some recent researches showed that the discrete quantum dots can be formed using 2D (two-dimensional) electron present in quantum wells or semiconductor materials' heterostructures.¹⁰ After coating the sample surface with a thin resist layer, the desired pattern can be created in the layer by electron beam lithography. This pattern will be conveyed by etching.¹⁰ The benefit of this technique is that it is easier to control the positions of self-assembled quantum dots.¹⁰

1.2.2 Ga and GaN quantum dots

For many optical device applications' developers, gallium nitride (GaN) is a kind of ideal direct band gap semiconductor materials. GaN, with a band gap of 3.4 eV at 300 °K⁴⁸, is widely used in UV blue LED (light-emitting diodes), photo detectors, lasers.³⁻⁶ The synthesis of two dimensional structures (thin films) and one-dimensional structures (nanowires and nanorods) has consumed a lot of time and fund. However, Because of their discrete energy spectrum and the few-carrier effects they display, zero-dimension structures are more meaningful to quantum dot device applications. A significant amount of studies about synthesis quantum dots has been launched; but how to directly grow gallium nitride quantum dots on silicon still needs a lot of work.

There are many factors that limit significant advances in device technology, including the ability to arrange materials at shrinking dimensions and the ability to successfully integrate new

materials of better properties with silicon. Methods for self-assembly of quantum dots are greatly desired for new devices which require smaller sizes, lower energy consumption, higher performance, and new functionality. In order to create such new devices, a patterning method must be used that can arrange quantum dots at the appropriate length scales. A focused ion beam (FIB) is one method of laterally arranging nanosized islands of dissimilar materials on silicon by creating template patterns directly on the Si substrate with nanoscale resolution. In order to encourage nanostructures' self-assembly, chemical/compositional deviations or surface features was used in the near surface region of templates.⁸² During FIB milling, surface topography is created as material is removed, however, implanted Ga is added which can form clusters or nanocrystals upon heating^{1,2}. Both processes are of potential attention for lateral positioning of nanostructures.

As a pre-patterned source of Ga, these templates can be further transformed to other useful Ga based semiconductor compounds.⁸³ For example, by implantation of Ga at 120 kV followed by implantation of N, we have created synthesis of GaN quantum dots.⁸⁴ We could also synthesize Amorphous GaN by implanting Ga into amorphous SiN.⁸⁵ Recently, some researchers has reported that the low energy implantation is now available to implant Ga near the surface of SiN then get GaN.⁸⁶

This technique mentioned above therefore offers the potential to combine the most prominent LED materials with Si, the cornerstone of the semiconductor industry. The emergence of Nitride-based semiconductors brought in new ideas to semiconductor optical device applications. In particular, Because its potential to be used in next generation light-emitting devices, self-assembled GaN quantum dots became attractive.⁸⁷ By using metal-organic chemical vapor deposition (MOCVD) on $\text{Al}_x\text{Ga}_{1-x}\text{N}$ surfaces⁸⁸ and by molecular beam epitaxy (MBE) on

a AlN surface, The formation of GaN quantum dots became achievable.⁸⁹ However, growth of GaN directly on silicon, the most technologically important substrate, is a challenge due to the thermal expansion coefficient mismatch between the GaN and Si substrate.¹⁹⁻²¹ By using the FIB to directly create nanoislands, we allow relaxation at the surface, when forming the nanodots on highly mismatched substrates.⁹⁰

1.2.3 Nucleation of Ga clusters

Ion implantation technology is mainly used to dope semiconductors in modern electronics industry. It has also been used in ion-beam synthesis (IBS) to generate growth source for nanostructures.^{27, 28} This includes self-assembled quantum dots formed in a bulk matrix and under-surface precipitates that form after annealing ion-implanted materials. For example, it has been demonstrated that high doses of Ga implanted into SiO₂ followed by annealing can result in the formation of Ga nanodots at random locations.²⁹ A Ga⁺ ion source is usually used in Focused ion beam systems (FIB) for engineering reasons. The movement of the ion beam can be controlled in these systems to form the desired pattern. Thus, FIB systems are most frequently used for maskless lithography and micromachining. One of the most important applications is to prepare samples for transmission electron microscopy (TEM), where the FIB is used as the material removal tool. It is suggested in an article from Kammler et al.¹, implanted Ga atoms can be created when FIB micro patterning of Si(001) surfaces by using Ga⁺ ions. And then the Ga atoms will diffuse to the surface during annealing process, and eventually form a modified surface region which can act as a surfactant. However, in this case it is unclear whether the Ga atoms actually diffuse to the top of the surface, or if they may instead form sub-surface clusters, or precipitate underneath the surface.

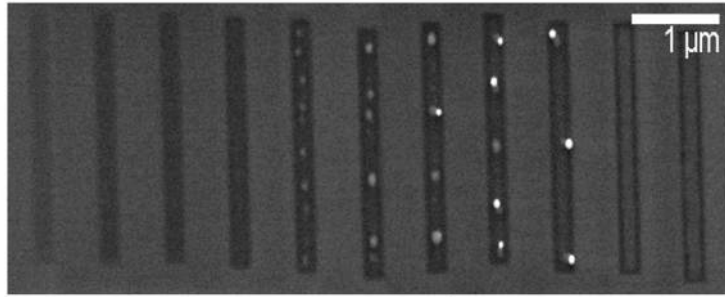


Figure 1.1 Ga nanodots on SiO₂ surface fabricated by FIB with different dosages.²⁹

To effectively apply the FIB to the synthesis of surface nanostructures at specific spots, we need to stick to several pieces of guide. First, the implanted material must be implanted at levels above the solubility limit of the host material. It is advantageous to choose the implant and host pair with low solubility. Second, the chemical reactivity between the host material and implanted ions can't be ignored. We are pursuing chemically stable implants in the host material, although certain chemical reactivity, such as the implanted material reducing the host, will be helpful. Finally, it will be helpful if the surface region of the substrate becomes amorphous, so it will be easier for the implanted material to move to the surface. There are some other factors that can affect the characteristics of surface precipitates. The size of pattern area, annealing condition, relative surface energies of segregated material and host surface will all contribute to the diffusion behavior.²⁹ It has been reported by Buckmaster²⁹ that Ga nanodots can be formed on SiO₂ surface with the help of FIB, as shown in figure 1.1. In this approach, they use trench patterns with different dosages to observe the formation of Ga nanodots after vacuum annealing. The morphology of the Ga nanodots is closely related to Ga dose, showing a critical dose needed

for nucleation that results in Ga nanodot formation just below the surface, while at higher doses Ga nanodots form on the surface as metallic Ga droplets.²⁹

1.2.4 Deposition of SiGe on Si substrates

Usually, lattice mismatched heteroepitaxy, large strains and the significant amount of resulting elastic strain energy are interrelated. The reason is that morphological evolution of the growing film or the introduction of misfit dislocations could release the lattice mismatch. Under proper growth condition, the conventional strain relaxation mode, which is forming misfit dislocation, will not be observed. Instead, new phenomena of three dimensional surface roughening will take place and become the new strain relaxation process. The unwanted excessive elastic energy will be released much more due to the 3D relaxation mode compared to the 2D mode. The surface roughness expresses the form of isolated islands with high lattice mismatch.³⁰ The shapes in the transition process depend on temperature; and the islands will change back to dome-shape form pyramid-shape when cooling down.³¹ The larger the mismatch strain is, the smaller size of the quantum dots.^{32,33} All of above suggests that the larger lattice mismatch strain (due to higher Ge content) is, the smaller quantum dots size will be. Increasing Ge concentration will increase the kinetics of the island formation, as a result, wetting layer will be thinner and evolution of the surface morphology will be faster.

For a lattice mismatched system, such as SiGe/Si, the topography created by the FIB can lead to the formation of strain-relieving islands at preferential sites. This applies not only to SiGe/Si, but also in theory to any lattice mismatched film grown on a dissimilar substrate. There have been recent examples of this for InAs/GaAs and Cu₂O/SrTiO₃ material systems.^{34,35} For the

case of SiGe/Si, it has been demonstrated using conventional molecular beam epitaxy (MBE), i.e. electron-beam evaporation of Si and Ge under UHV conditions (less than 1×10^{-10} Torr), that deposition of epitaxial strained SiGe on top of a FIB patterned Si substrate can lead to preferential island formation at pit edges (which can be found in figure 1.2) under appropriate growth conditions where the kinetics are limited by lower growth temperature and higher growth rates.¹³ In this case, the FIB patterning was done ex-situ to the MBE growth chamber, and it is believed that the topography of the substrate is guiding the formation of the quantum dots. The size of the pit should be dependent on the strain in the film, but may also be modified by growth conditions and film thickness. In the preceding experiments^{7,32,36,37}, the Ge concentration was set at 30%, we got a 20 nm wetting layer thickness underneath a pit approximately 70 nm wide. Much higher Ge concentrations supposed to be applied in the future experiments to reduce the pits size and wetting layer thickness. The Ge concentration needs to be raised above 70% to achieve sizes below 20nm. We need to control the Ge diffusion at high growth temperature to obtain the high Ge concentration while keeping the same morphology. Along with the high concentration, a higher Ge growth rate is also required, but the MBE system can't meet the requirement.

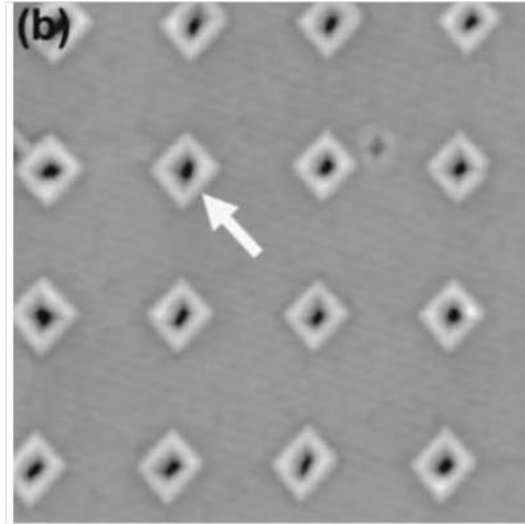


Figure 1.2 AFM $2\ \mu\text{m} \times 2\ \mu\text{m}$ images of 20 nm $\text{Si}_{0.7}\text{Ge}_{0.3}$ film grown at $550\ ^\circ\text{C}$ and $0.9\ \text{\AA}/\text{s}$ on a 7 nm Si buffer layer for patterned region within the FIB array.¹³

It has also been proven that the nucleation of discrete Ge islands on FIB patterned sites can be reached by using ultra high vacuum chemical vapor deposition (UHV-CVD).³⁸ As the situation discussed here, the FIB patterning was an in-situ process. The Ga will behave as surfactant and play an important role in the geometry size and islands' properties no matter it is beneath the surface or on top of the surface.¹ However, the problem is, the growth rate is also reduced as the temperature is reduced during CVD growth. Therefore, unlike the situation in MBE, neither growth temperature nor growth rate can be adjusted individually. This makes it more difficult to achieve conditions of limited kinetics for higher Ge concentrations.

Another possible technique is sputtering. There are many benefits using sputtering, including the reduced cost and versatility. In industry the use of high vacuum sputtering is wide spread, which makes the sputtering method more attractive for potential industrial applications. In addition, epitaxial growth can be achieved, potentially at lower substrate temperatures and

there are additional means of adjusting the kinetic energy of the sputtered atoms. Sputtering growth provides more options for modifying the nucleation and growth of surface structures, which are not available with MBE. The composition of the layer and therefore strain can be varied by independently changing the power to each of the sputtering sources. The crystalline quality and electronic properties of UHV sputtered films have also been shown to be comparable to those grown by MBE.³⁹⁻⁴² Apart from a roughening at very low misfit, both the defect structure and surface morphology of films sputter-grown at high average adatom excess energy are very similar to those observed in films synthesized by conventional growth techniques such as MBE and CVD.⁴² Island morphologies similar to those observed using MBE have also been demonstrated using UHV sputtering.⁴³⁻⁴⁵ A much higher growth rates can be achieved for Ge deposition, which will be important for studies of kinetic effects.

1.3 APPLICATION OF GAN

1.3.1 High-efficiency light-emitting diodes (LEDs)

The active layer of semiconducting material is used in an LED device with a sandwiched structure. The active layer is located between n-type and p-type semiconductor cladding layers. Electrons from the n-type material will jump into the conduction band of the active layer when a voltage is applied to the junction. At the same time, holes from the p-type layer will move into the valence band.⁴⁶ When the recombination between the electrons and holes happen, light emission will occur in the active layer.⁴⁶

Some specific types of GaN nanodots and GaN nanostructure can be used in manufacturing the LED devices. These nanodots and nanostructures formation process are carefully control in order to get specific geometry. By fine tuning the parameter GaN's size and nanostructures's dimensions, this kind of LED devices can excite light with different wavelengths, which means different colors. In addition, the GaN nanodots structures with shrinking dimension will make the future laser diodes' size much smaller than current ones. The shrinking size, as a result, will lead to an obvious energy-saving effect. Running for the same period of time, the new devices will consume much less energy than current ones.

1.3.2 Short wavelength laser diodes (LDs)

In laser diodes' circumstances, it is necessary to use additional light-guiding layers to sandwich the active layer and then to restrict the light within the light-guiding layers if the active layer is too thin to restrict the light within the active layer. Because of the refractive index difference between light-guiding and the cladding layers, the light generated at the active layer is restricted within the light-guiding layers.⁴⁷ This sandwich style structure is called a separate-confinement heterostructure (SCH) because the light and guided along parallel by different layers(active layers and light guiding layers). Mirrors are used at the ends of the light-guiding layer to reflect the light back and forth. The reflected light can trigger other electrons to recombine with holes; then cause the release of further light and magnify the light when there is population inversion.⁴⁸ At a certain current (the threshold current), strong stimulated emission can be detected at the edges of the light-guiding layers, and the device is called an LD. Achieving continuous wave GaN–InGaN laser diodes is very important for technology development.⁴⁹

If the size of individual GaN nanodots and the geometry of the GaN nanostructure can be chosen precisely, the laser with specific wavelength can be excited. Thus desired laser can be produced by this kind of devices. Beyond the ability of accelerating different laser, with the shrink dimension of the GaN nanodots structures, the whole size of the laser diodes can be much smaller than what we currently have.

1.3.3 UV Photo-detectors

The AlGa_xN system with 3.4–6.2 eV band gaps is the best candidate material for the application of ultraviolet (UV) detectors. Usually, materials with smaller band gap are more sensitive to infrared and visible radiation. This character makes the AlGa_xN used in nitride devices such as laser detectors, ozone monitors, flame sensing, and pollution monitoring.⁴⁶ The responsivity cut-off wavelength can be adjusted within the range of 365 to 170 nm by adjusting the amount of Aluminum.⁴⁶ As a sequence of the direct gap of the Ga-rich alloys, the quantum efficiencies of the AlGa_xN system are high. With that being said, this system is very suitable to form heterojunctions and it can operate at relative high temperature. As a result, Al_xGa_{1-2x}N tends to be ideal material to fabricate UV detector.⁴⁶

In our case, if the size of individual GaN nanodots and the geometry of the GaN nanostructure can be controlled precisely, the specific wavelength can be collected preferentially. By adjusting the parameter of the GaN nanodots and the structure, the device can be made to be sensitive to desired UV with given wavelength.

1.4 SIGE QUANTUM DOTS

Silicon photonics have promising potential for the next generation of high-performance optoelectronic devices.⁵⁰ Because modulators make waveguides optically connect to detectors on silicon photonic chips, they become indispensable parts of these devices. To make these devices commercial accessible, The main problem is fabricating higher speed silicon photonic devices with more reasonable cost.⁵¹ The key to fabrication of these kinds of devices is heteroepitaxial growth of semiconductor structures. Also, quantum computers can utilize SiGe quantum dots structures as the basic processing unit.⁶¹ Due to the quantum effect, the electrons will be confined in a four-side-wall shape structure. The unit can represent “1” by charging the electrons in “/” direction and represent “0” by charging the electrons in “\” direction.

However, if the epitaxial layer has a different lattice constant than the substrate, there will be a lattice mismatch, which can cause large strains to develop in the epitaxial layer. To lower this negative effect, we can try to form islands on the surface of the film.⁵¹ With the help of relieving the strain, quantum dots could self-assemble into two-dimensional arrays with specific order on the film surface.⁶²

Restricting SiGe island formation to occur at just the template sites formed during FIB milling sites will be the goal of this set of experiments. To form the desired quantum dot structures, we need to have the ability to control the position and size of the quantum dot to meet the application requirement. By changing the dosage at the milled sites, the thickness of the buffer layer and the growth rate of the alloy thin films, we will explore how this impacts island formation under epitaxial growth conditions. During this process, the strain due to lattice mismatch between the SiGe thin film and Si substrate is the dominant factor that will determine

the final morphology of the nanostructures. The kinetics in this self-assembly process can be manipulated by varying the growth rate or the growth temperature.

The wide range of dosages ($0.2 \times 10^{15}/\text{cm}^2$ to $20 \times 10^{15}/\text{cm}^2$) may need to be chosen to provide a large window for the formation of SiGe quantum dots. Based on the wider selection of dosages, we can expect higher possibility to observe the preferential formation of SiGe quantum dots on the FIB patterned sites.

Higher Ge concentration will require careful consideration of the kinetics during growth. Higher Ge concentration results in smaller self-assembled structures, which would be better for quantum confinement purposes. The growth temperature will need to be kept relatively low to suppress islanding and interdiffusion which could lead to overall lower effective concentrations and larger characteristic sizes. To suppress islanding for pure Ge, it is expected that the kinetics must be slowed down even further compared to the growth of the 30% Ge structures³² since relaxation processes such as islanding happen much more quickly for higher strain levels, because higher Ge concentration will cause larger lattice mismatch. These constraints make growth rate the primary variable. To achieve conditions which island formation required, the Ge composition must be increased from 30% to 50%; at the same time, the growth rate must be increased three fold as well³². Although much higher growth rates are not possible with our Si target, we have an unlimited range of growth rate with the Ge source. The strained alloy growth will be stopped before island formation begins in order to study the initial pit formation process in more detail. The whole process is expected to be strongly dependent on composition, film thickness, and growth temperature and growth rate. The growth window for producing quantum dot structures is rather narrow, rendering it difficult to tailor the length scale of the structures. In addition, for high misfit systems, the energy barrier for island nucleation is relatively small, so

that islands already provide an efficient means of strain relaxation before a sufficient wetting layer for pit formation is reached. Very thin wetting layers that typically result for high Ge concentrations would limit the size of its making but clusters favored in order to relax strain.

1.5 GERMANIUM QUANTUM DOTS

Another potentially useful application is to use the pit arrays as templates to guide the formation of pure Ge nanodots. The combination of Ge self-assembled quantum dots and complementary metal oxide semiconductor (CMOS) technology is now achievable. This combination can be used for light emission in the range of telecommunication wavelengths.⁶³ These benefits make Ge quantum dots better material for templates. Self-assembled Ge quantum dots can be created by growing the epitaxial Ge layer on Si. And this kind of nanostructure has the potential to be used in quantum devices and solar cells.⁶³

Ge quantum dots with high density 3D packed array structures buried in Si substrate show supreme reduction of the thermal transport phenomena.⁶³⁻⁶⁶ Gillet showed by varying the Ge concentration, 3D Ge quantum dots supercrystals in Si can lower the thermal conductivity more than 0.04 W/m/K at room temperature.⁶³⁻⁶⁶

Some other techniques can provide us with similar results other than the FIB patterning method. In an alternative method, electron-beam-induced carbon deposits are used as masks during the growing process. Selectively deposition of InAs quantum dots inside InP holes⁸ can be achieved by applying this technique. In this process, the InP holes were formed when the masks were partially overgrown by InP and then the mask was removed. This method can be

mimicked to the Si/Ge system. Masks induced by E-beam can be fabricated on Si (001) surfaces.⁸ The pits were formed after the overgrowth of carbon deposition. Then the consistent arrays of Ge dots can be nucleated within and around the surface pits. Randomly distributed, but with similar structures can be found over the surface under MBE growth conditions.⁸ It is predictable that the formation of Ge dot arrays are controllable by applying the e-beam guided carbon nanomasks technology.

Ge has a larger lattice mismatch than SiGe alloy; so we will need to use a lower growth temperature or higher growth rate ($>3 \text{ \AA/s}$) and thinner Ge film thickness (8 \AA or 16 \AA) in order to suppress the Ge nanodots formation outside the patterned pit.

2.0 EXPERIMENTAL TECHNIQUES

Un-doped Si (001) wafers purchased from Virginia Semiconductor[®] were used as substrates for all of the experiments in our studies. The two different experimental procedures are shown in figure 2.1. The silicon wafers were cleaned ultrasonically in acetone for approximately 10 minutes followed by iso-propyl alcohol (IPA) for another 10 minutes before loading them into the dual beam FIB (Seiko Instruments SMI3050SE FIB-SEM). Controllable growth of nanostructures includes two approaches:

1. Ga nanodot formation and Nitridation
2. SiGe quantum dot formation

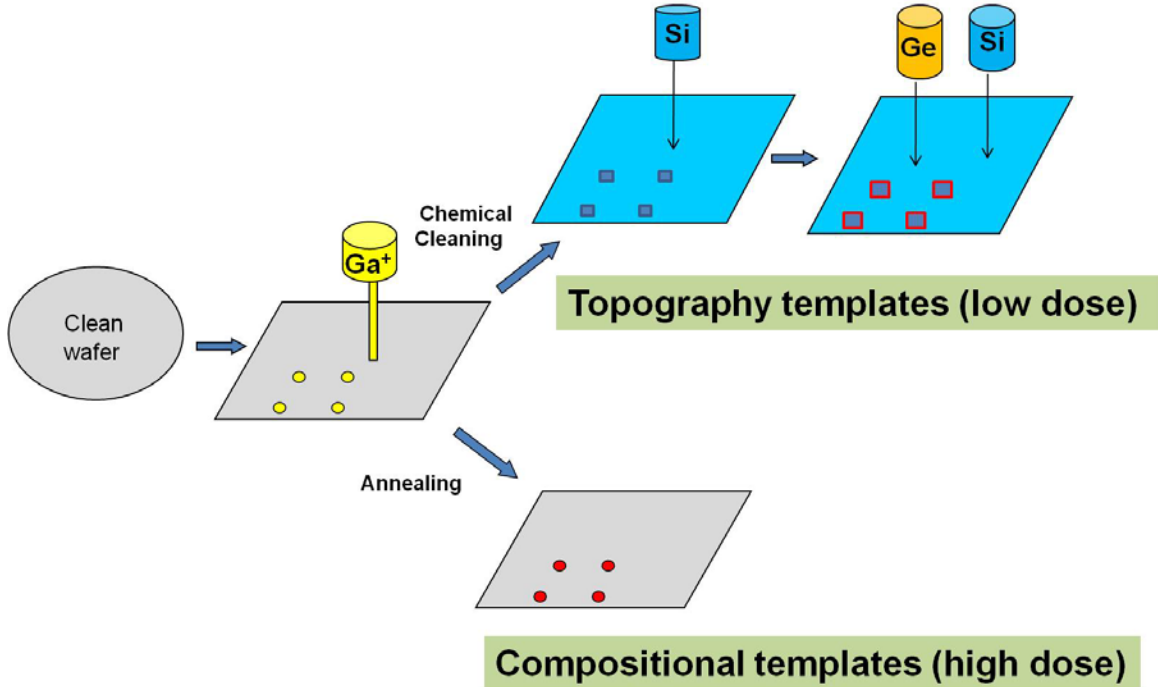


Figure 2.1. General experimental procedure in the FIB assisted nanostructure formation.

2.1 FOCUSED ION BEAM (FIB)

In a Focused Ion Beams system, a strong electric field is used to extract the ions from a liquid-metal ion source (LMIS), then to form the ion beam. The positively charged ions are emitted by electric field from a liquid gallium cone. The cone is formed at the tip of a high melting point metal (tungsten) needle. The chosen accelerating voltage is used to accelerate the emitted ions, then the ions would toward the sample surface.⁶⁷ As soon as the ions touch the sample surface, there is a one-way energy transfer occurs from the accelerated ions to the atoms on the sample's surface. There are some important effects when the Ga ion beam impinges the substrates. First,

the ion beam will sputter ionized and neutral atoms from the substrate, and this will lead to the removal or substrate mill effect which can be observed after the FIB patterning process by AFM or SEM. Secondly it will cause the emit phonons, which will bring the temperature of the substrate at a small level. Thirdly, the incident Ga ion beam will lead to the transposition of the host material, and result damage to the substrate. Finally, this process will release electrons, and these emitted electrons can be used for imaging. That's why usually FIB system also has the SEM column and the whole system is called dual-beam system.⁶⁸ Three primary parameters in the FIB patterning process are accelerating voltage, focused ion beam current and focal adjustment. Given higher accelerating voltage, which means the ions projected from the column with higher energy, ions can penetrate deeper in the substrate and it also provides better adjustment for the focus. With higher beam current, the beam diameter will be larger and it will become harder to adjust the focus. So in this research, we tend to choose smaller beam current to achieve fine control of beam size and position. Carefully adjusting the focus and eliminating the stigma can help to reach the round and symmetrical shape of beam which also increase the resolution of the patterning process.⁶⁸



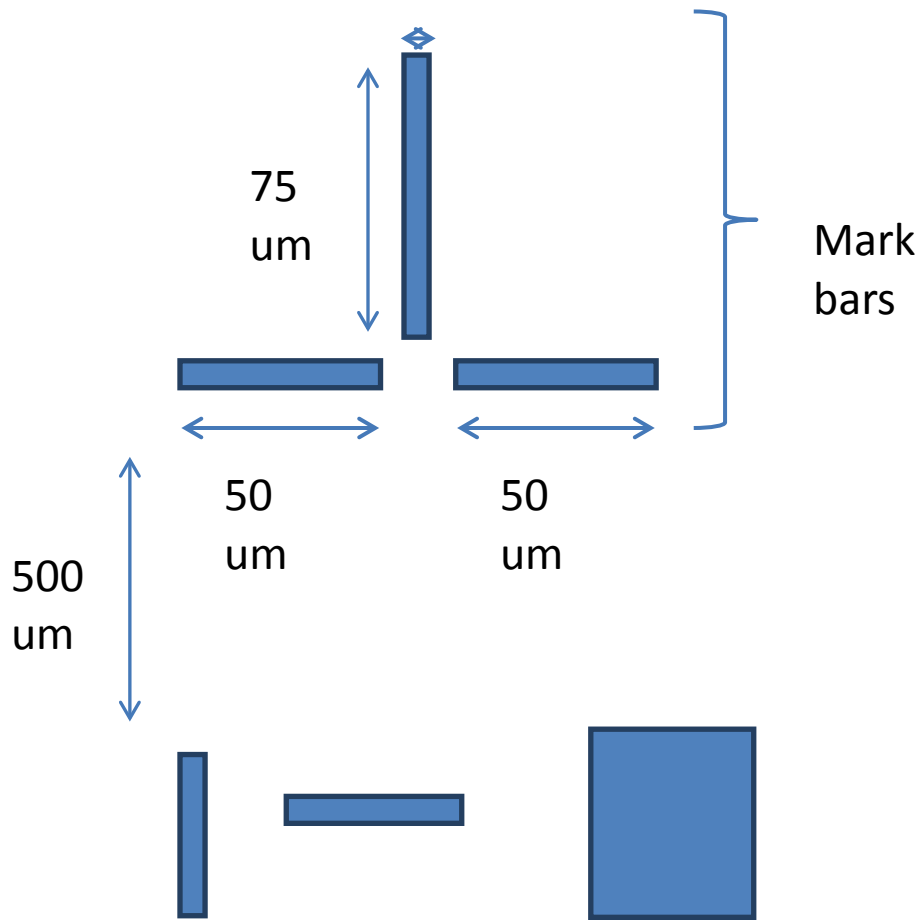
Figure 2.2 Focused Ion Beam System. ⁶⁸

2.2 FIB PATTERNING PROCESS

Some of the substrates used in these experiments were patterned before growth using a Focused Ion Beam (FIB). The specific instrument used was a Seiko Instruments SMI3050SE FIB-SEM with Oxford Instruments Inca XEDS. The ions are focused and accelerated down onto the sample with energy of 30 (or 10) keV and different beam currents ranging from 1 pA to 10 pA for the work described here. The appropriate alignments, focus, and astigmatism procedures are done before patterning is started. Final focusing and astigmatism are done at 150 kX magnification and are critical for creating the smallest, roundest holes possible during subsequent patterning.

Before creating the sputtered patterns, a marker bar is firstly fabricated by milling out large trenches that are easily seen under an optical microscope. These are used to aid in finding the patterned regions later in AFM analysis. After creating the marker bar in the center of the

sample, the sample is moved to the position for each of the patterns. The beam is blanked in between patterns and no more imaging is done on the sample at this point in order to prevent any damage to the rest of the substrate. The FIB patterns are shown in figure 2.3.



Ga patterns with different sizes and dosages

Figure 2.3 FIB pattern diagrammatic sketch (no to scale).

For Ga and GaN samples, squares or trenches with different physical dimension and dosages were created.

For $\text{Si}_x\text{Ge}_{1-x}$ samples, arrays of holes were created as fabricated diameters of 30 nm, depth ranging from 3 to 30 nm, and spacing of 200 to 400 nm. An AFM scan for one array can be seen in figure 2.5. In order to create these arrays, the Ga beam is rastered across the sample according to a predetermined bitmap file, which is the case produce an array of holes. The file used here is created by Dr. Gray.



Figure 2.4 FIB pattern used for SiGe quantum dots growth.

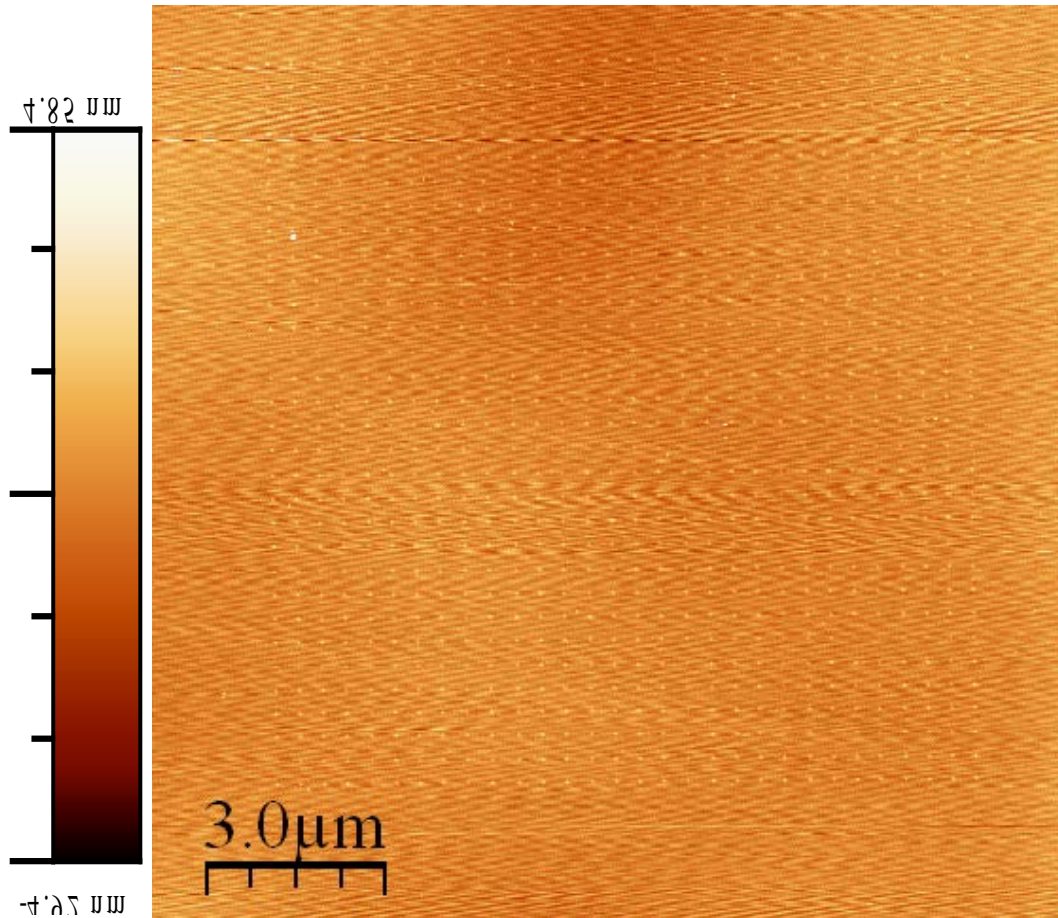


Figure 2.5 AFM image of FIB dot array pattern Si substrate. Dosage is $3.0 \times 10^{15}/\text{cm}^2$, the voltage is 30 kV and the beam current is 1 pA.

2.3 SUBSTRATE CLEANING PROCEDURES

Before being loaded into the magnetron sputtering system ultra-high vacuum (UHV) chamber, all the $\text{Si}_x\text{Ge}_{1-x}$ samples need to be cleaned. The samples need to be soaked in acetone and isopropyl alcohol (IPA) to remove backside tape first, then applied solvent clean. Finally, a

modified Shiraki cleaning procedure needs to be performed to complete the cleaning process.

The followings are the solutions used in the Shiraki procedure:

1. IMEC = 4 H₂SO₄ : 1 H₂O₂, room temperature
2. RCA-2 = 4 H₂SO₄ : 1 HCl : 1 H₂O₂ (heated to 85°C in water bath)
3. Oxidation = 1 H₂O : 3-4 HCl : 2 H₂O₂ (heated to 85°C in water bath)
4. BOE = Buffer Oxide Etch = 7 Ammonium Fluoride : 1 HF

All chemicals should be cleanroom grade. There are some requirements for the cleaning process: for the RCA and Oxidation solutions, the peroxide should be added just before the sample is ready for that step. A single beaker should only be used for one solution in one cleaning step. All acid beakers (include beakers used in solvent clean) should be pre-rinsed in DI water for 5 minutes before each use. The protection glasses and acid-proof gown need to be worn all the time for protection. Gloves need to be worn at all times and silver shield gloves are used for handling acid. The tweezers and sample dippers can only be touched with new and clean gloves. The entire procedure is performed under a hood operated at full flow. The following content is the step by step cleaning procedure, which includes the chemicals used at each step, time and temperature for each step.

Solvent Clean:

1. IPA -1 for 1.5 minutes in ultrasonic bath at room temperature
2. Acetone-1 for 1.5 minutes in ultrasonic bath at room temperature
3. Trichloroethylene for 10 minutes in 85°C water bath
4. Acetone-2 for 1.5 minutes in ultrasonic bath at room temperature
5. IPA-2 for 1.5 minutes in ultrasonic bath at room temperature

6. DI rinse in DI-1 for 5 minutes

IMEC

1. Mix enough solution to just cover sample in IMEC beaker
2. Immediately add sample
3. Etch for 5-7n minutes
4. DI rinse in DI-1 for 2 minutes
5. BOE dip in HF-1 for 15 seconds
6. DI rinse in DI-1 for 5 minutes

RCA-2

1. Add peroxide to hot HCL solution
2. Add sample
3. Etch for 2-3 minutes
4. Dip rinse in DI-2
5. 15 seconds dip in BOE (HF-2)
6. Dip rinse in DI-2
7. Repeat steps 3-6 two more times with final BOE dip in HF-3 beaker
8. DI rinse in DI-2 for 5 minutes

Oxidation

1. Add sample to oxidation beaker so that it is lying facing up on the bottom of the beaker
2. Add half of the peroxide and wait for 5 minutes before adding the other half
3. After 10 minutes, reaction should be complete (no significant bubbling)
4. Rinse in DI-2 for 10 minutes or longer

After cleaning process, an N₂ gun is used to blow the sample until completely dry. The samples also need to be examined under a light to see if there are any particles or contamination before being loaded into the load lock of the sputtering system.

2.4 PHYSICAL VAPOR DEPOSITION (MAGNETRON SPUTTERING)

Sputtering, known as a physical vapor deposition process, is usually used for depositing thin films of metals, alloys, semiconductors and dielectric materials in a vacuum environment. An evacuated chamber with a pair of metallic electrodes comprises the basic sputtering system. A cathode, which should be connected to the negative terminal of a DC power supply, is usually used as the target (source). There is also a substrate to be used as the anode. The substrate can be process in multiple ways: grounded, biased negative/positive, heated or a combination of all these. The process also needs vacuum pumps to evacuate the chamber; as well as, a noble gas (argon, neon) is used as working gas to originate self-sustaining plasma under the condition of an

electrical discharge. The gas pressure need to be controlled in the range from a few to a few hundred millitorr in order to “strike” the plasma^{69,70}.

When positively charged inert gas atoms from the plasma sputter physically remove atoms from the target through momentum transfer, the sputtering happens. Therefore, in this stage sputtering can be considered as physical vapor deposition. The removed atoms then enter the plasma discharge region and finally deposit onto the substrate. Other particles (secondary electrons, negative ions) and radiation (x-rays) are also taken away from the target during sputtering. The emitted secondary electrons can promote the ionization of neutral argon atoms (in the plasma) during the sputtering process. Out of the purpose to increase the possibility of ionization, ring magnets are placed right underneath the targets to confine the electrons. Because of the configuration, the process tends to be magnetron sputtering. The Lorentzian force generated by the magnetic field then can trap the electrons within the magnetic field so that the electrons won't lose to the sidewalls of the chamber. So magnetron sputtering helps to keep electrons in the plasma longer by trapping them. Then the ionization rate will be increased. Compared to conventional sputtering, the higher ionization rate could get plasma with lower strike pressure. The lower chamber pressure will increase the mean free path for the atoms while they move toward the substrate. In conclusion, magnetron sputtering brings about two kind of benefit: increased deposition rate and increased mean free path of sputtered atoms.

The sputtering system set up used for deposition of thin films in all our studies is shown as a schematic in figure 2.1. It consists of a separate load-lock sample introduction chamber, a cryo-pumped main chamber, one RF and one DC power supplies, four UHV magnetron sources,

and all true UHV valves and seals. The system is primarily pumped by the cryo-pump, and is capable of achieving pressures in the low 10^{-10} torr regime with the recent addition of a getter pump. The chamber can hold substrate with diameters up to 4". There is also a gas introduction ring on the substrate supply nitrogen for nitridation process. The gas sources should be purified to the parts-per-billion level before introducing into the chamber. In addition to that, the heating lamps can bring the substrate holder as high as 850°C. The sputtering system also has the ability to uniform the thin film growth by rotating the substrate holder with the help of the motor. Bias voltage can also be applied to the substrate while heating it up. There is a reflection high energy electron diffraction (RHEED) system has been installed on the sputtering system. The primary usage of RHEED is monitoring the epitaxial quality and roughness of the surface in-situ during growth.

The sputter rates for Si and Ge were calibrated using the KLA Tencor 'Alpha-Step IQ' Surface Profiler[®] at the University of Pittsburgh's Nanoscale Fabrication and Characterization (NFCF) Facility. The substrate-target distance was maintained at 6 and 5 inches for the samples. The Si and Ge targets used were 2 inches in diameter, 0.125 inch thick, 99.999% pure and were purchased from Kurt J. Lesker Company[®]. The argon gas used was 99.999% pure, purchased from Valley National Gas[®]. All the sputtering processes were carried out at room temperature. The Si/SiO₂ wafers were purchased from Virginia Semiconductor. The 2 inch wafers had 300 nm thermally grown SiO₂ layer on the surface.

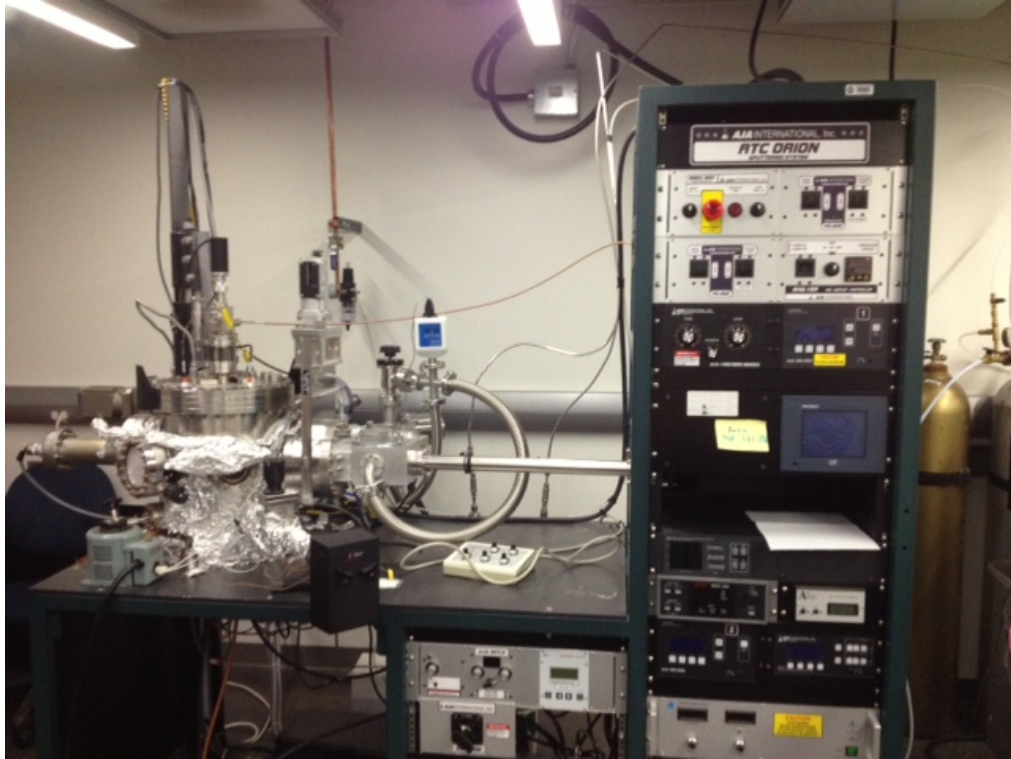


Figure 2.6 Magnetron Sputtering System used to grow all samples.

2.5 REFLECTION HIGH-ENERGY ELECTRON DIFFRACTION (RHEED)

The $\text{Si}_x\text{Ge}_{1-x}$ films in this experiment were grown using a magnetron sputtering system. The growth surface is monitored in-situ using reflection high-energy electron diffraction (RHEED). This technique provides information on the surface structure and crystalline quality of the film during growth. The electron beam is operated at a voltage of 30 kV and current of 1.45 A. The beam covers an area approximately 2 mm in diameter on the sample surface and hits the surface at an angle of only a few degrees. Most of the incident electrons will only interact with the surface atoms due to the glancing angle. As we know, the two-dimensional surface in real space will yield rods lattice in reciprocal space and these rods are normal to the substrate surface. The

RHEED pattern is the result of the intersection between Ewald sphere and the reciprocal rods lattice. With all that being said, the RHEED patterns generated by the flat surface will have the shape of discrete streaks with different intensity. If the surface is disordered, the RHEED pattern will only consist long streaks. On the other hand, the RHEED pattern will be spotty pattern if the surface is rough.⁷¹ That is because the electron is interacting three-dimensional structures rather than ideal flat surface.⁷² The schematic of RHEED can be found in figure 2.7.

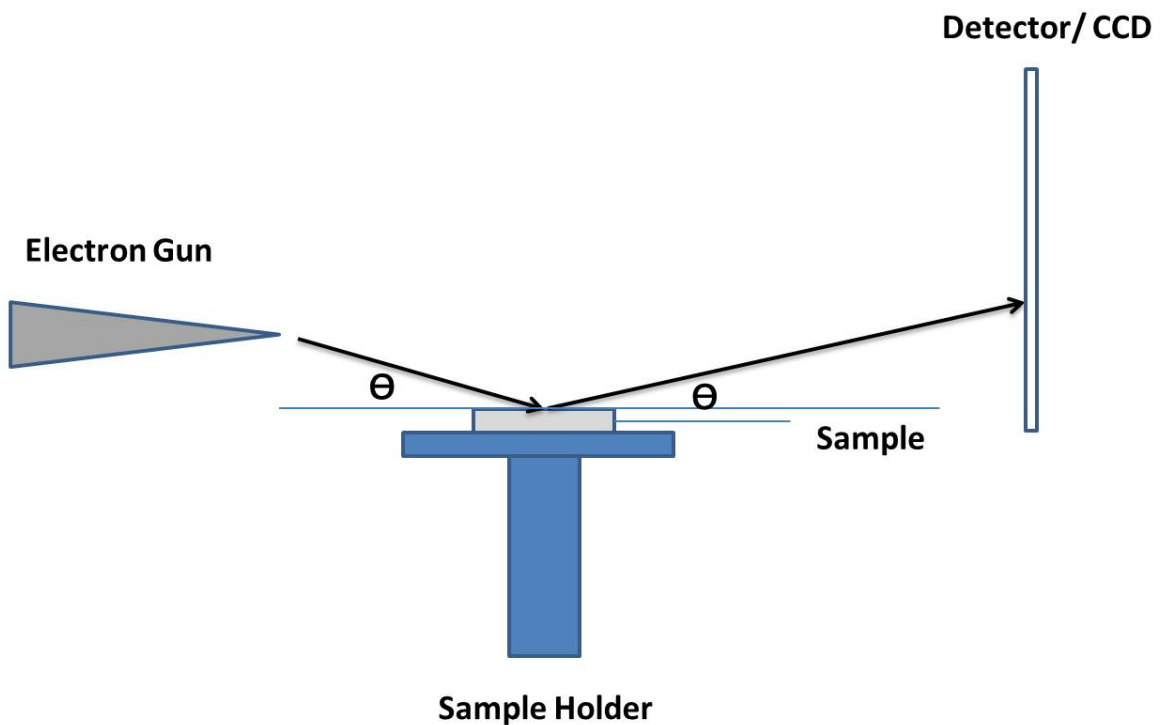


Figure 2.7 Schematic diagram of RHEED used in the research. .

2.6 ATOMIC FORCE MICROSCOPY

In AFM, a sharp probe scans across the surface. During the scan the monitor will record the tip-sample interaction. In this research effort, all AFM analysis was carried out in tapping mode. Figure 2.8 represents a cantilever at the sample surface. The cantilever will move up and down when there is vertical excitation by a piezo stack. As the cantilever moves vertically, the position of reflected laser beam, so called “return signal,” will change direction and be recorded by a quad photodiode. It is this process generates the electrical signal. The tip deflection will change as soon as the tip encounters the surface. As a result, laser position will change on the quad photodiode. All these alterations will finally change the electronic signal that the instrument received. The whole procedure will disclose some characteristics of the material such as elasticity, magnetism and presence of electrical forces, as well as the vertical height of the sample surface.

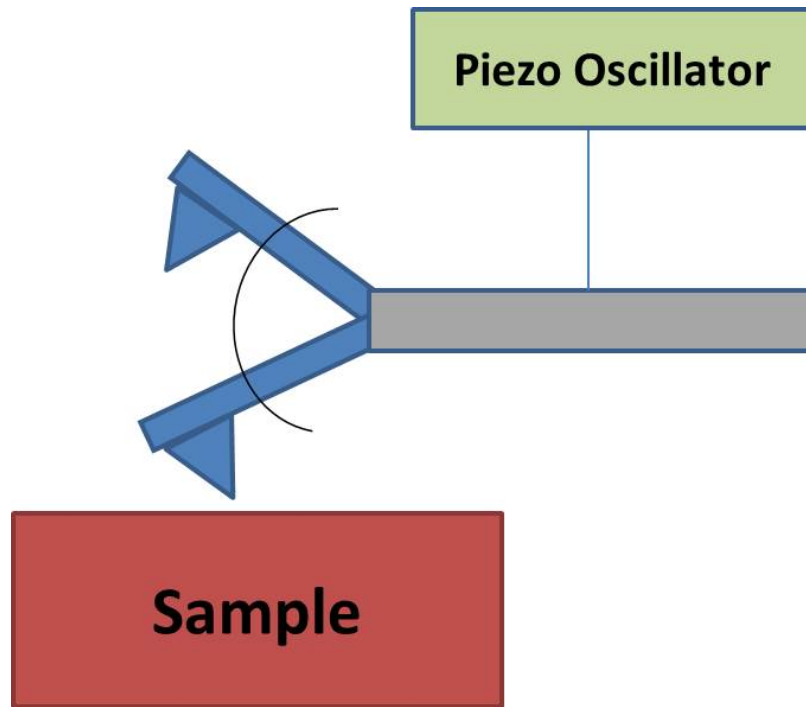


Figure 2.8 AFM working status.

The scan size is 512×512 pixels and the scan speed ranged from 1 Hz for $50 \times 50 \mu\text{m}^2$ scan to 2 Hz for $1 \times 1 \mu\text{m}^2$ or smaller scan size. The offline version of the software package Nanoscope IIITM was used for processing the images. Dimension 3100 Digital instruments AFM is the equipment to be used, which belongs to MSE department of the University of Pittsburgh (as shown in figure 2.9).

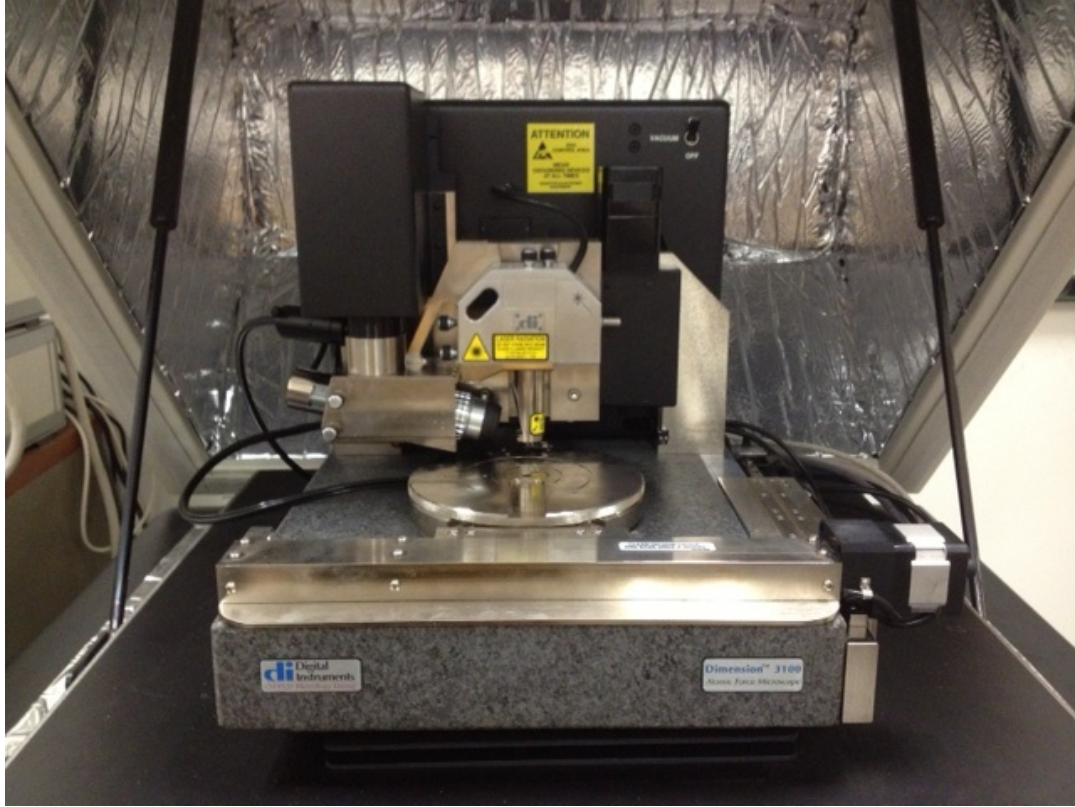


Figure 2.9 AFM used to characterize all samples.

2.7 TRANSMISSION ELECTRON MICROSCOPY

Transmission electron microscopy (TEM) analysis was done using a JEOL JEM-2100F (Schottky field-emission electron gun (FEG) at 120kV up to 200kV). The TEM (figure 2.10) is part of the nano fabrication and characterization facility (NFCF) at the University of Pittsburgh. In TEM, a high-energy electron beam is scattered, as it is “transmitted” through the sample. The exiting beam has two major components: a transmitted beam and diffracted beams due to scattering from interacting with the sample. A bright field image is formed when only the

transmitted beam is used. A dark field image is formed when one of the diffracted beams is selected by using a selected area diffraction aperture. TEM images used for all our research studies were obtained from the bright field-imaging mode, dark field mode and selected area diffraction mode.



Figure 2.10 The JEOL JEM-2100F TEM located in the nano fabrication and characterization facility (NFCF), University of Pittsburgh.

The JEOL JEM 2100 F is also equipped with high angle annular dark field (HAADF) detector. The HAADF collector only collects the incoherent electrons, which are not Bragg diffraction electrons. These electrons carry the elemental information.

2.8 TEM SAMPLE PREPARATION

2.8.1 TEM Plan View Samples Created by Mechanical Thinning and Chemical Etching

The TEM sample for the HR-TEM experiment is specially made at the MEMS lab at the University of Pittsburgh. Figure 2.11 shows the schematic drawing of the Si sample. The Si piece holder is 320 nm thick and 2 by 4 mm in size to fit in the TEM sample holder. The fabrication procedure for the Si piece holder is also shown in figure 2.11. SOI (silicon on insulator) wafers (320 nm thickness of device layer, (100) orientation) on 1000nm oxide layer with about 700um handling layer were commercially purchased.

First, the wafer is cut into rectangular pieces that fit the TEM sample holder (in our case, 2x4 mm). Then the pieces are thinned to about 100 um by mechanical (hand) polishing. Then each 2x4mm chip is placed on a glass slide, covered by melting wax layer with a hole in the center that exposes about 1mm circle on the back and covers the rest, and the circle is wet-etched with silicon etchants. In this etching process, we apply two etchants contain the same chemicals but with different concentration. The etchants contains hydrofluoric acid (HF), acetic acid (CH_3COOH) and nitric acid (HNO_3). The fast etchant is used in the initial step of the etching. Its

ratio is HF: CH₃COOH: HNO₃ = 3:3:5. When we find relatively large area of exposed silicon glares red under optical microscope, we stop the fast etching and change to the slow etchant. The ratio of the slow etchant is HF: CH₃COOH: HNO₃ = 3: 6: 5. The etching will be stopped when multiple small holes are found in the etched area. The Si specimen is placed under a low magnification optical microscope, the source of light comes from the back, and monitored while it's being etched – the trained eyes are supposed to be able to identify when to stop the etching the optically transparent areas begin to show. This usually takes from 10 to 30 min. The etch stops when the etchant reaches the oxide layer. These specimens are then thoroughly cleaned in sulfuric acid (soaked in it overnight). Clean chips are stored in DI water until it's time to load them in the TEM. Each chip is etched in 1:5 HF: H₂O immediately before loading to remove the oxide layer and expose the SOI membrane. Our oxide was 1 um thick, and the last step took about 45min to remove all traces of oxide. The electron transparent areas are about 10-100um in lateral size (this depends on when the silicon etch has been stopped – less than 10um is not that useful, more than 100um is too fragile).

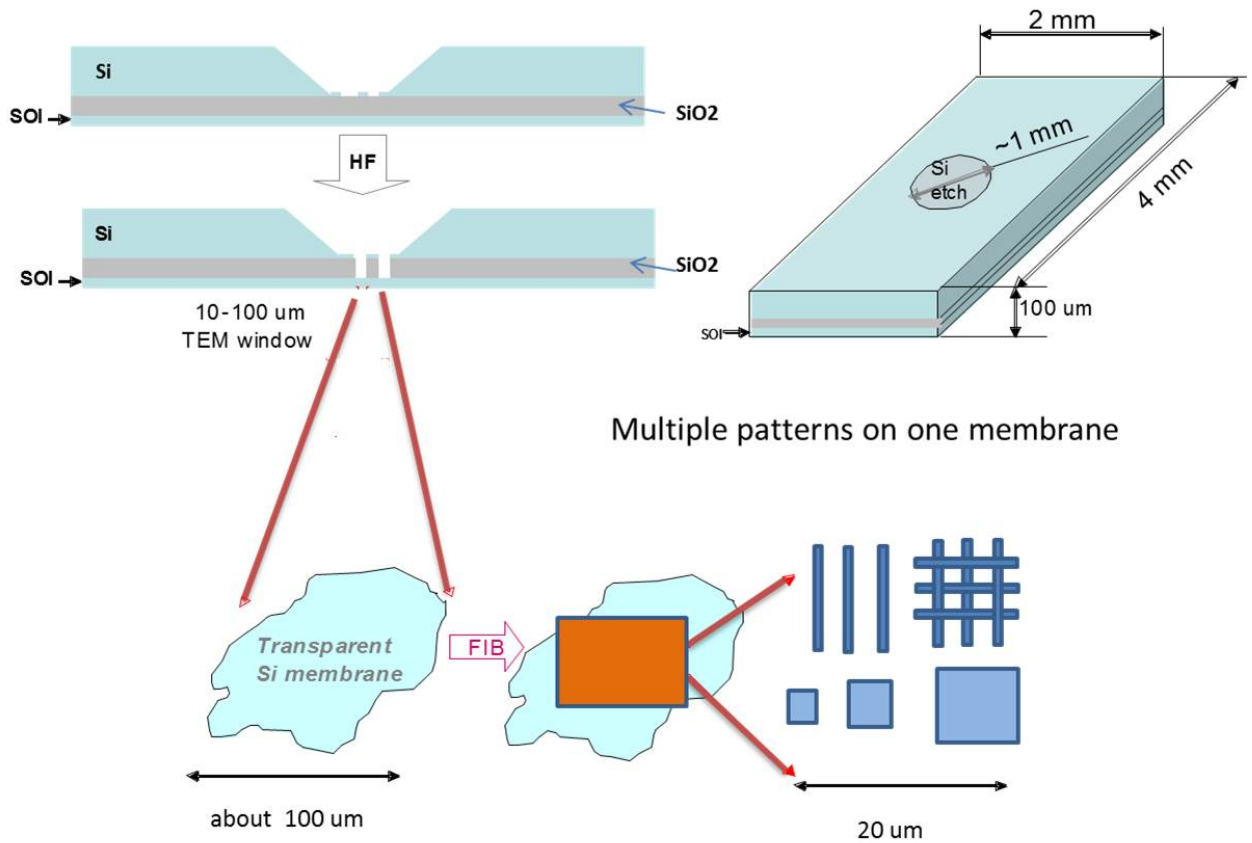


Figure 2.11 Fabrication Process of TEM samples.

2.8.2 Nonporous Amorphous Silicon Membrane

UltraSM TEM Window substrates (from SiMPore Inc.) were also utilized as the substrate for gallium templates. The key difference between this method and the one we discussed in the previous section is that these substrates are amorphous Si. These TEM substrates consist of 9 square windows. Each window has identical dimensions, 100 μm by 100 μm. The nonporous amorphous silicon membrane in each of the square windows has a thickness of 15nm, which is suitable for transmission electron microscopy (TEM) analysis.

2.8.3 TEM Plan View Samples Created by FIB

A new method of making plan view TEM sample in the FIB will also be tried to characterize the Ga nanocrystals. The first step of making a plan view TEM sample is the same with the one in ordinary FIB cross-section sample preparation procedures. After the sample has been mounted on the TEM grid (as shown in figure 2.12), we will use Ga ion beam to thin the sample from the back side to reach the thickness which is electron transparent in TEM.⁷³

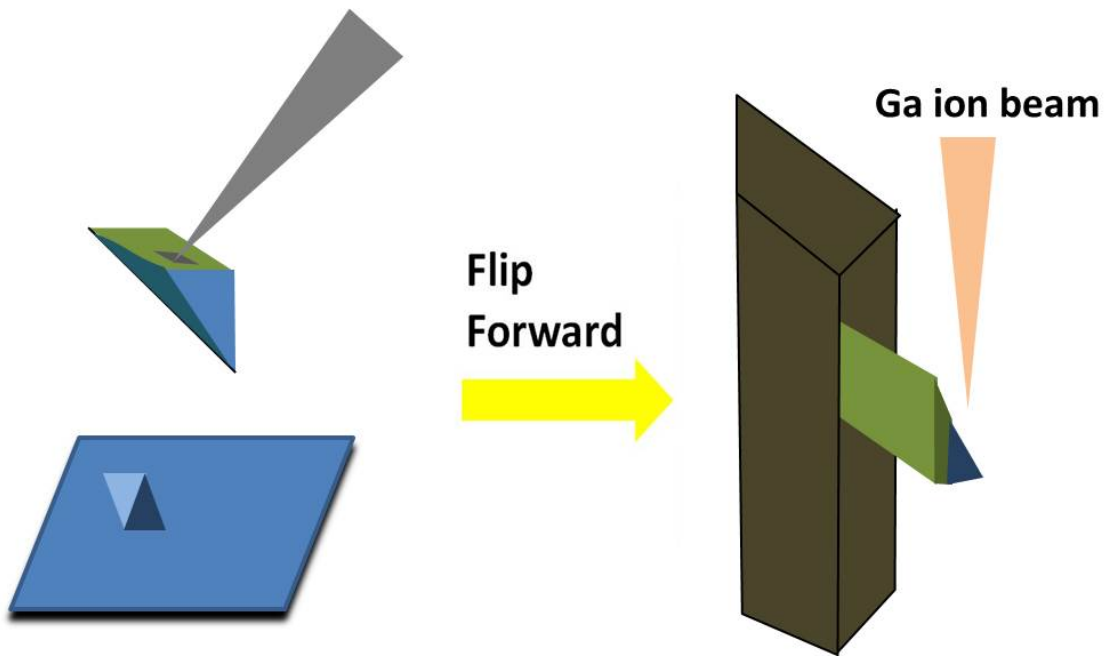


Figure 2.12 Plan view TEM samples preparation procedure.

3.0 GALLIUM NANOISLAND FORMATION

The primary objective of this study is to form gallium nanodot templates. The templates on silicon substrate using a focused ion beam direct patterning method will be used as a source of gallium for the eventual conversion to GaN. Such a method can be applied to controllably form gallium nanodots of specific sizes at a particular position on the substrate to create new device structures. Since an un-doped silicon substrate itself contains no trace of gallium, the technique discussed here employs different dosages to fabricate the gallium template on standard Si substrates and on thin amorphous Si membranes for analysis using transmission electron microscopy.

3.1 OVERALL EXPERIMENTAL DETAILS

Si (001) substrates were used for most of the Ga templates in the study. The silicon wafers were cleaned ultrasonically in acetone for about 10 minutes followed by iso-propyl alcohol (IPA) for another 10 minutes before loading them into the dual beam FIB (Seiko Instruments SMI3050SE FIB-SEM). The gallium templates were patterned in the dual beam FIB using a beam current of 10 pA and an accelerating voltage of 30 kV. These patterns consisted of a series of rectangular trenches which were milled using dosages that varied from $29 \times 10^{15}/\text{cm}^2$ to $42 \times 10^{15}/\text{cm}^2$ (number of ions/ cm^2). The width of the trench patterns was also varied, including trench widths

of 50nm, 100nm, 200nm and 300nm. All the trench patterns created had a uniform length of 5 μm . We choose wider dosage window for patterning to explore the effect of dosage applied in FIB process on the formation of Ga nanodots. Multiple geometry dimensions have also been used in this experiment to evaluate the relationship between the size of Ga nanodots and the dimension of the pattern area.

To confirm the formation of gallium nanodots, UltraSM TEM Window substrates (from SiMPore Inc.) were also utilized as the substrate for gallium templates. The key difference is that these substrates are amorphous Si. These TEM substrates consist of 9 square windows. Each window has identical dimensions, 100 μm by 100 μm . The nonporous amorphous silicon membrane in each of the square windows has a thickness of 15nm, which is suitable for transmission electron microscopy (TEM) analysis.

After removal from the FIB system, the samples were ultrasonically cleaned in acetone and IPA before being loading into an ultrahigh vacuum (UHV) chamber with a base pressure of 1×10^{-9} Torr and annealed at 600 $^{\circ}\text{C}$ for 1 h. This annealing time and temperature was chosen based on previous reports found in the literature of Ga droplet formation in SiO_2 . After removal from the vacuum chamber, the samples were analyzed using an atomic force microscope (AFM) (Digital Instruments DimensionTM 3100) in tapping mode to obtain the topography information of the templates both before and after annealing. High resolution-transmission electron microscopy (HR-TEM) analysis of the gallium nanodots formed was conducted using a JEOL JEM-2100F.

An overall AFM topography image of the trench patterns created in the FIB is shown in Figure 3.1. The trench width varies from 0.05 μm to 0.3 μm , and the dosage has a range between

$29 \times 10^{15}/\text{cm}^2$ and $42 \times 10^{15}/\text{cm}^2$. It is observed that in the template before heating, there is no topography features inside the trenches which appear to be flat in AFM profile measurements. However, it can be seen in AFM images after annealing that features form in the trenches. This can be explained by the diffusion kinetics. Before vacuum annealing, the gallium atoms locally implanted in the silicon substrate do not have sufficient energy to diffuse in the substrate to form gallium dots. During vacuum annealing, the large number of gallium atoms implanted in the silicon substrate have enough thermal energy to allow the formation of nanodots to occur.

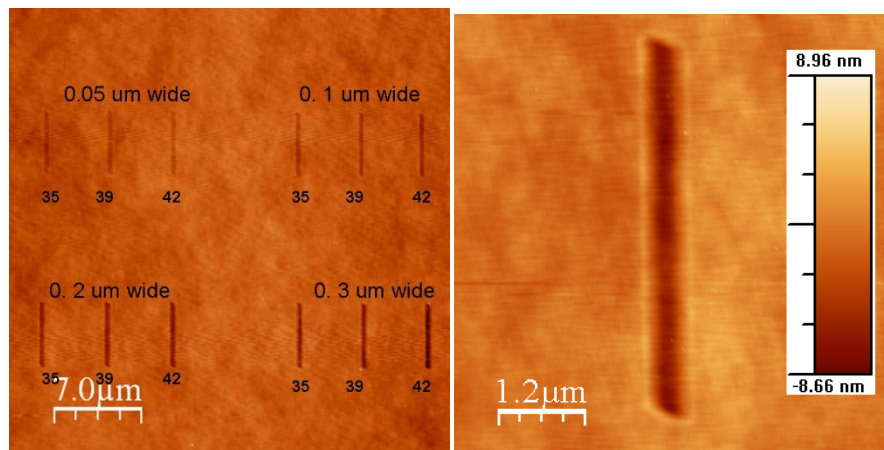


Figure 3.1 (a) overview AFM image of trench patterns before annealing. (b) Higher magnification of image of a single trench illustrating lack of topography in bottom of trenches before annealing. Image is of trench in lower left corner of Fig 3.1(a).

3.2 GALLIUM TEMPLATES USING DIFFERENT DOASGE

Three different dosages of $35 \times 10^{15}/\text{cm}^2$, $39 \times 10^{15}/\text{cm}^2$ and $42 \times 10^{15}/\text{cm}^2$ were used to compare gallium nanodot formation as is shown below in figure 3.2. All the trenches compared here are

with the same trench width of 200nm. It is observed that gallium nanodots were pervasively present in different trenches with different dosages as seen in figure 3.2. Based on the images obtained from AFM and the measurements made on the nanodot structures, it is found that there is a relationship between the dosage and the average diameter and height of the gallium nanodots, which is showed in fig 3.2 (d). The nanodots in the higher dosage trench have on average greater diameter and height.

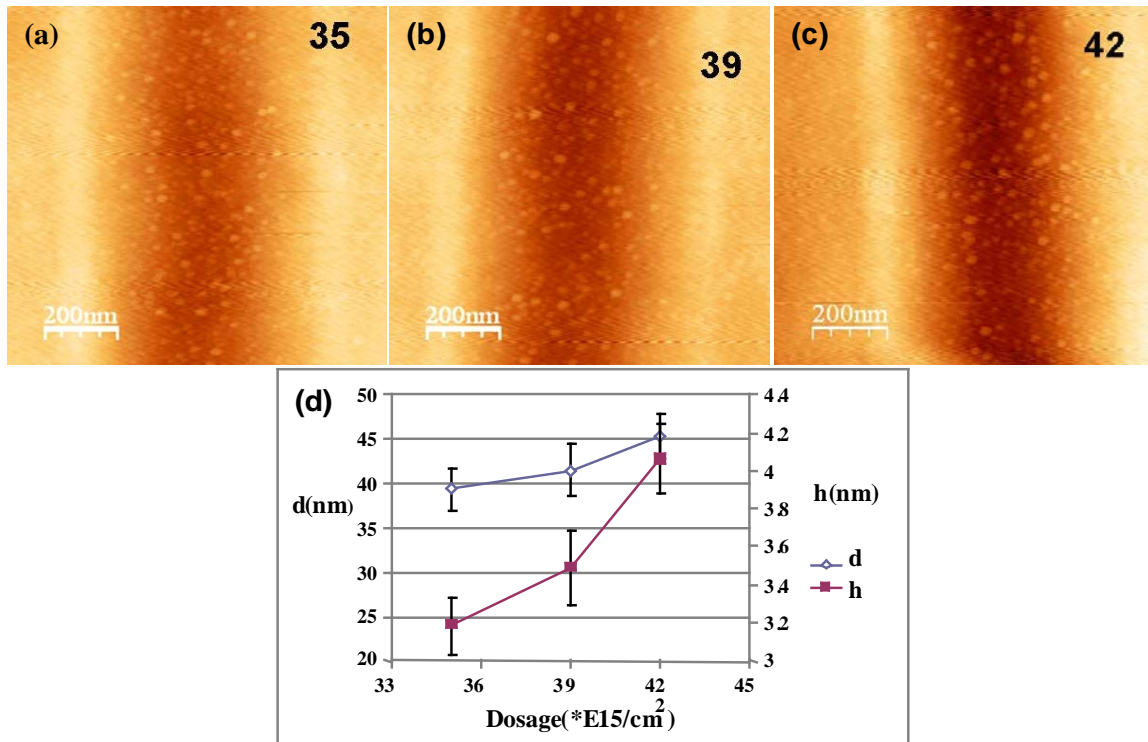


Figure 3.2 AFM image of trenches with different dosage after annealing: (a) $35 \times 10^{15}/\text{cm}^2$, (b) $39 \times 10^{15}/\text{cm}^2$ and (c) $42 \times 10^{15}/\text{cm}^2$ nm, (d) Ga nanodot diameter and height vs. dosage.

3.3 GALLIUM TEMPLATES USING DIFFERENT TRENCH WIDTH

The effect of trench width on Ga nanodot formation was also analyzed. This also confirmed from another aspect that with more gallium implanted, the nanodots tend to grow larger. With larger width, even when the dosages are the same, the total amount of gallium atoms will be greater, which means the total source of gallium atoms that can diffuse and form nanodots is larger (shown in figure 3.3). Given that there is enough energy at 600 °C in vacuum during the annealing process, the gallium atoms implanted in the substrate can form the nanodots during the one hour anneal, with an average size that depends on the total amount of Ga available in the irradiated area.

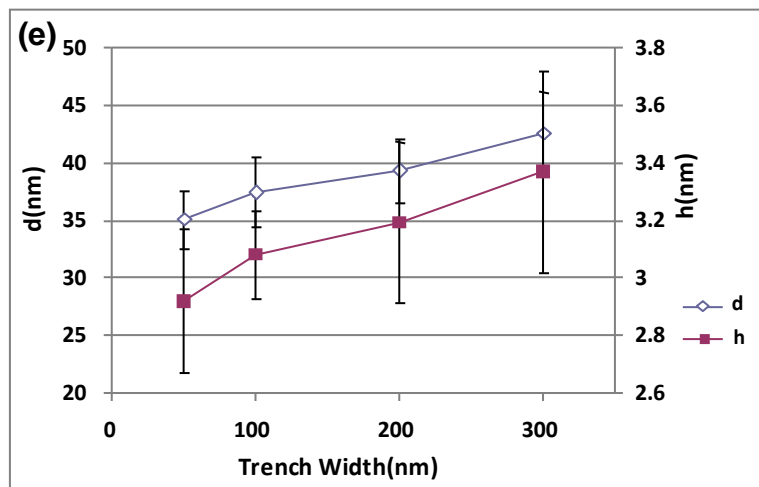
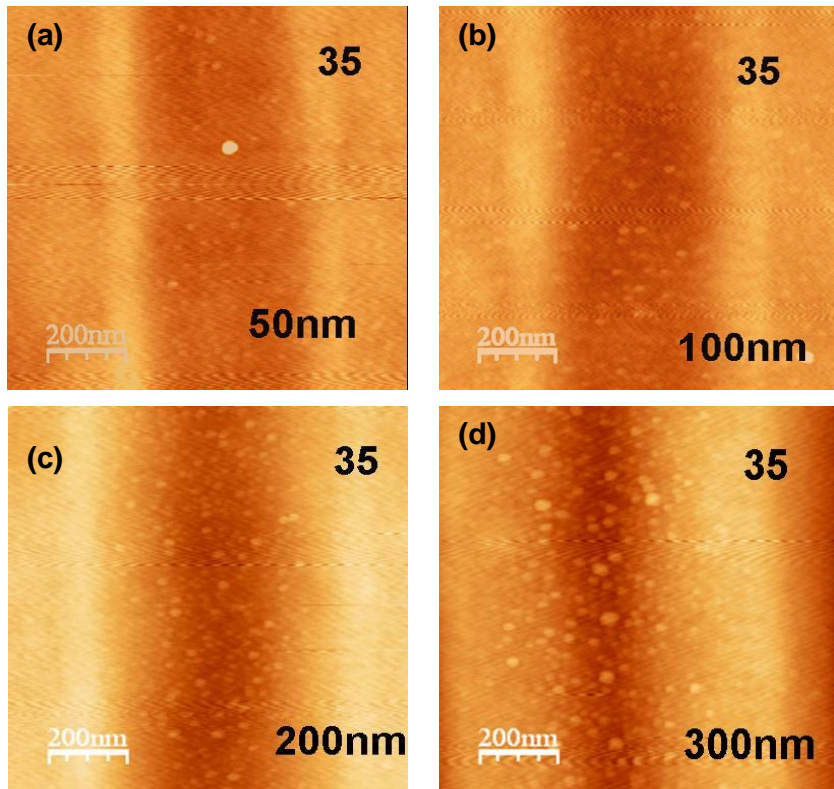


Figure 3.3 AFM image of trenches with different width after annealing: (a) 50 nm, (b) 100 nm, (c) 200 nm, (d) 300 nm, (e) Ga nanodot diameter and height vs. trench width.

3.4 GALLIUM TEMPLATES PATTERNED ON AMORPHOUS SI TEM WINDOWS

Gallium nanodots formed on the non-porous amorphous silicon TEM membrane are shown in figure 3.5. The dosage used here is $35 \times 10^{15}/\text{cm}^2$. To confirm that these nanodots are most likely Ga nanocrystals rather than small regions of crystallized Si, HAADF-STEM was used since it is the most suitable method for Z-contrast imaging and therefore ideal for characterizing these nanocrystals. By using a STEM detector with a large inner radius (a HAADF detector) electrons are collected which are not Bragg scattered. HAADF images show little or no diffraction effects, and their intensity is approximately proportional to Z^2 .⁷⁴ A high density of bright dots was detected in the silicon membrane for the patterned area. It can be determined from the HAADF images that the smallest size of gallium nanodots is approximately 5 nm. HR-TEM images also confirm this measurement. The background contrast in figure 3.5 (c) and (d) is due to the amorphous silicon membrane. It can be seen from the HRTEM image that the gallium nanodots are crystalline because of the presence of the atomic lattice fringes. A conclusion can be made that in the vacuum annealing process the crystallization of the gallium nanodots occurs.

The smallest visible gallium nanodot size seen in the TEM images is approximately 5nm. Given the density 5.91 g/cm^3 and molecular weight of 69.72 g/mol for gallium, we can obtain the result after calculation [from equation (1) to (4)] that the smallest nanodots contain 1670 Ga atoms (making an assumption that the gallium nanodots have a half sphere shape). The dosage used in the FIB was $35 \times 10^{15}/\text{cm}^2$, which equals $350/\text{nm}^2$, so the number of atoms needed to form the nanodots could come from a 5nm^2 area. The nanodot sizes measurement from AFM images is different from what we observed from TEM images. This difference could come from three different sources: first, there could be possible differences in diffusion of Ga nanodots on

the substrate and surface energies for a crystalline silicon substrate versus an amorphous silicon membrane. Another likely scenario could be that some of the gallium ions are able to penetrate through the very thin (15 nm) silicon membrane which means some of the Ga is not contained within the membrane, resulting in lower concentrations of Ga than what is expected. The third possibility may be within the TEM we are also seeing sub-surface cluster formation as discussed by Kammler et al.¹, which may be smaller than the surface nanodots.

$$V = \frac{1}{2} * \frac{4}{3} \pi \left(\frac{d}{2}\right)^3 = \frac{1}{2} * \frac{4}{3} \pi (2.5 * 10^{-9})^3 = 32.725 * 10^{-21} \text{ cm}^3 \dots\dots\dots (1)$$

$$m_{Ga} = \rho * V = 5.91 \text{ g/cm}^3 * 32.725 * 10^{-21} \text{ cm}^3 = 193.405 * 10^{-21} \text{ g} \dots\dots\dots (2)$$

$$n_{Ga} = \frac{m_{Ga}}{M_{Ga}} = \frac{193.405 * 10^{-21}}{69.72 \text{ g/mol}} = 2.774 * 10^{-21} \text{ mol} \dots\dots\dots (3)$$

$$\# \text{ of atoms} = 2.774 * 10^{-21} * 6.02 * 10^{23} = 1670 \dots\dots\dots (4)$$

Results based on equations 1-4 have been checked by using the SRIM (Stopping and Range of Ions in Matter) Monte Carlo simulation.⁷⁵ This simulation uses the standard elemental data in the SRIM library, and 1400 ions per calculation which is based on the diameter of the focused ion beam multiplied by the dosage. The parameter set used in the SRIM simulations were as follows: Angle of incidence was 0° (normal incidence), the beam species Ga⁺, beam energy was 30 keV, the material was Si and the thickness of sample was 150 Å. We found that a significant number of ions penetrate through the entire thickness of the membrane in figure 3.4.

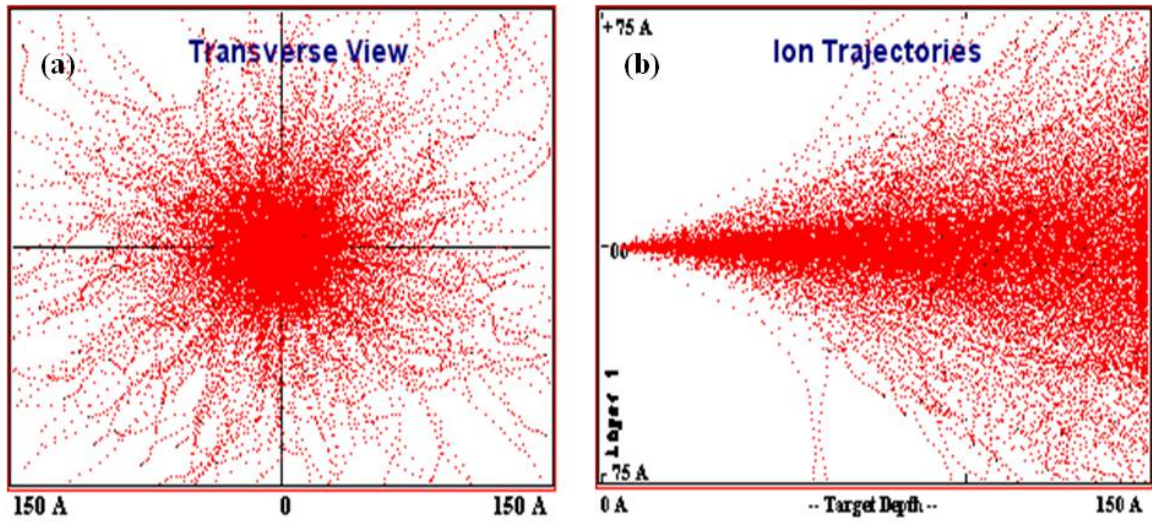


Figure 3.4 SRIM Monte Carlo simulation result of ions trajectories in Si with an accelerating voltage of 30 kV. Total number of ions is 1400. (a) Transverse view. (b) Ion trajectories.

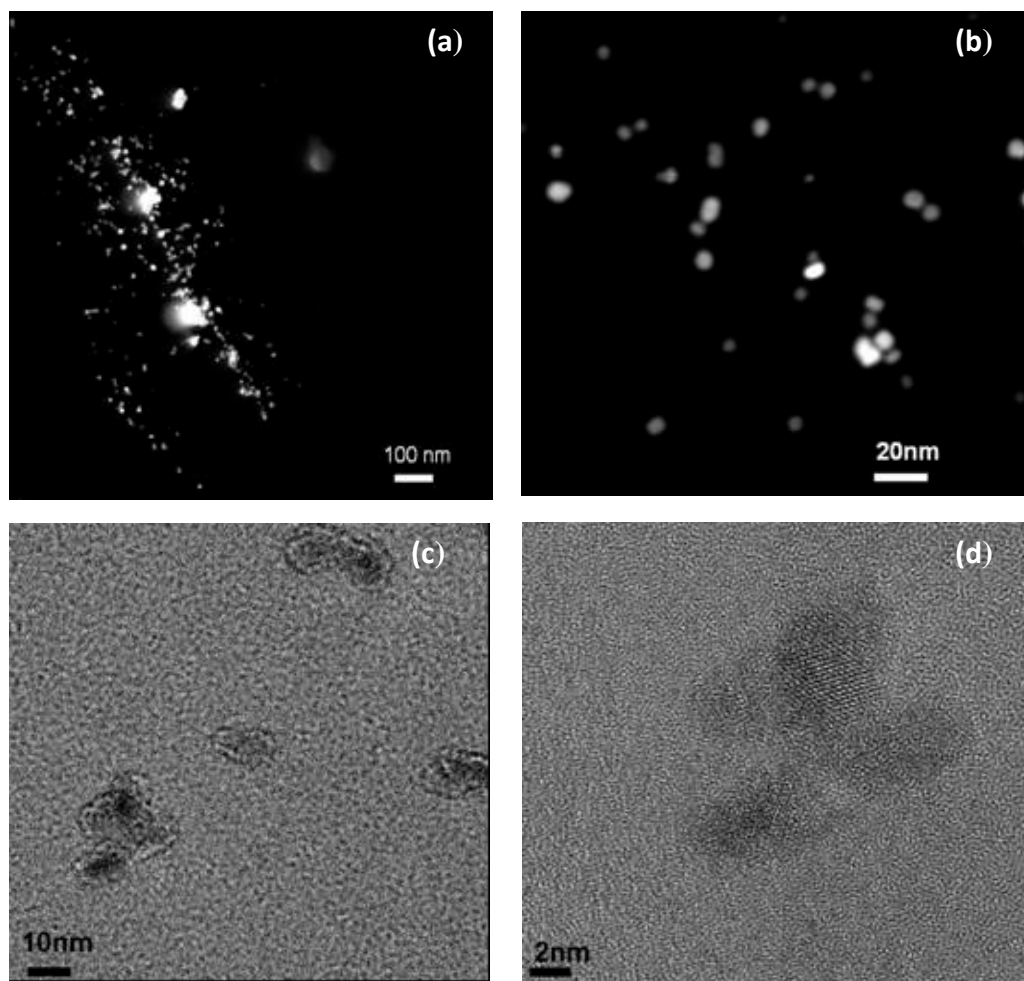


Figure 3.5 HAADF and HR-TEM images of Ga nanodots on amorphous silicon membrane: (a) HAADF of template, (b) HAADF at higher magnification, (c) HR-TEM of Ga nanodots and (d) HR-TEM of Ga nanodots at higher magnification.

3.5 GALLIUM TEMPLATES WITH SQUARE SHAPE

Si (001) substrates were used for all of the experiments in the study. The silicon wafers were cleaned ultrasonically in acetone for approximately 10 minutes followed by iso-propyl alcohol (IPA) for another 10 minutes before loading them into the dual beam FIB (Seiko Instruments SMI3050SE FIB-SEM). The substrate was patterned in the dual beam FIB using an accelerating voltage of either 30 kV or 10 kV and a beam current of 5 pA. The total number of Ga ions/cm² impinging on the surface during FIB patterning, commonly referred to as dose or fluence, was varied to investigate the effect on the Ga islands' size. This value depends on the ion beam current used and milling time. The patterned samples were ultrasonically cleaned in acetone and IPA before being loading into a vacuum chamber with a base pressure of 9×10^{-10} Torr and annealed at 600 °C for 1 hour. This annealing time and temperature was chosen based on previous reports found in the literature of Ga droplet formation on SiO₂ and our previous experiments on thin amorphous Si membranes⁷⁶.

In order to determine if the nanoislands formed on the surface were metallic, an HCl (37%, clean room grade) etch was used to preferentially remove any Ga from the surface of the Si. The samples were soaked in HCl at room temperature and ultrasonically agitated for 5 minutes then rinsed under DI water for 5 minutes. An atomic force microscope (AFM) (Digital Instruments Dimension TM 3100 operated in tapping mode) was used to characterize the surface topography of all the samples before annealing, after annealing and post wet etching.

The plan view TEM samples were made from SOI (silicon on insulator) wafers consisting of a 320 nm thick (100) Si layer on top of a 1000 nm oxide layer with an approximate 700 μ m handle base thickness. The samples were first thinned to about 100 μ m by mechanical

polishing. Then final thinning was done by etching a small exposed area from the back-side of the samples. The etchant is a mixture of hydrofluoric acid (HF), acetic acid (CH₃COOH) and nitric acid (HNO₃). The samples were then thoroughly soaked in sulfuric acid overnight to remove any contamination. Each plan view sample was etched in 1:5 HF: H₂O immediately before loading in the FIB to remove the oxide layer and expose the silicon membrane. For the 1 μm thick oxide layer, it took about 45 minutes to remove all traces of oxide. The electron transparent areas are about 10-100 μm in lateral size.

The effect of heating substrate for various FIB patterns and conditions is first examined to determine under what conditions Ga surface islands will form. Clear evidence of island formation is seen for larger total ion exposures used in conjunction with relatively large square milled areas. An AFM topography image of the square milled patterns before and after annealing created with a total ion patterning dose of 2.9×10^{16} ions/cm², a 5 pA beam current and 30 kV accelerating voltage in the FIB is shown in figure 3.6. Based on AFM analysis, the FIB beam shape is round and the diameter of a single point mill site is approximately 16 nm after careful alignment and focusing for this combination of beam current, accelerating voltage, and milling time. Since this diameter is less than the distance between dwell points of the beam (approximately 45 nm) within the raster scan, there is little overlap of the dwell points. These individual beam dwell sites are slightly raised with respect to the rest of the surface due to swelling caused by amorphization of the substrate at each FIB dwell point⁷⁷. Therefore, these beam dwell positions can be seen in the AFM image of figure 3.6 (a) as regular faint periodic features within the square box mill and also cause the edges of the box to appear scalloped instead of perfectly straight. A small amount of re-deposition is also likely happening around the edge of the patterned area, which can lead to nucleation of islands at the pattern edge after

annealing since it will contain some Ga as well. Other than features above, no other significant topography features were observed inside the milled square (figure 3.6(a)). However, from the AFM image it can be seen that overall, material is being removed from the patterned area under these patterning conditions since the milled area is about 4 nm lower in depth than the surrounding substrate surface.

After annealing, it can be seen in the AFM images that islands formed in the square area (figure 3.6 (b)). These islands can form as a result of large number of gallium atoms implanted in the silicon substrate having enough thermal energy to segregate to the surface and nucleate nanocrystals during the vacuum annealing. In this case the maximum total amount of Ga implanted should be approximately equal to the implanted number of ions/cm² times the patterned area size, although some Ga may be lost from the surface during milling due to sputtering. Based on Monte Carlo simulations for an accelerating voltage of 30 kV, it is estimated that most of the Ga atoms are expected to be between 15 nm to 40 nm under the surface.⁷⁸ From Fahey et al.⁷⁹ and Makris et al.⁸⁰ we can assume an activation energy of diffusion of implanted Ga in Si of 3.75 eV with a prefactor of 60. Given this value, the annealing temperature and time used in these experiments, we can calculate an approximate diffusion length of 15 nm for the Ga ions. In addition, the material close to the surface in the patterned area will have been heavily damaged leading to amorphization and some will have been removed due to the sputtering of Si by the Ga beam. Ga is known to segregate to the surface of Si^{81–83} when used as a surfactant, and for the case of implanted Ga we also expect to have defect-enhanced diffusion toward the surface⁸⁴. Therefore it is likely that a large amount of Ga is able to diffuse to the surface upon annealing. From Elliman et al.⁸⁵ it has also been observed that a small fraction of implanted Ga will redistribute towards the surface and a Ga concentration peak

at or near the Si surface will occur for samples that have been annealed when the damaged Si recrystallizes. This is also commonly observed when the concentration of impurities exceeds equilibrium solubility limit.⁸⁵ In this case the impurity atoms increased the total energy of the whole system due to lattice strain which is the driving force for the recrystallization process. As a result of this process, the implanted Ga atoms will be driven towards the surface of the substrate by the advancing growth front of the recrystallized region. The second question is if there will be enough Ga at the surface to exceed the solubility limit. The solid solubility limit of Ga in Si is about $4.5 \times 10^{19}/\text{cm}^3$ and it has been shown that this limit will be exceeded at the surface for an ion implantation dose as small as $6.17 \times 10^{15} \text{ ions}/\text{cm}^2$ at 100 kV.⁸⁶ Therefore, under our patterning conditions which we have a much higher number of ions/cm^2 impinging on the sample and narrower implantation depth range expected at our lower accelerating voltage, the solubility limit should also be exceeded at the surface of our samples.

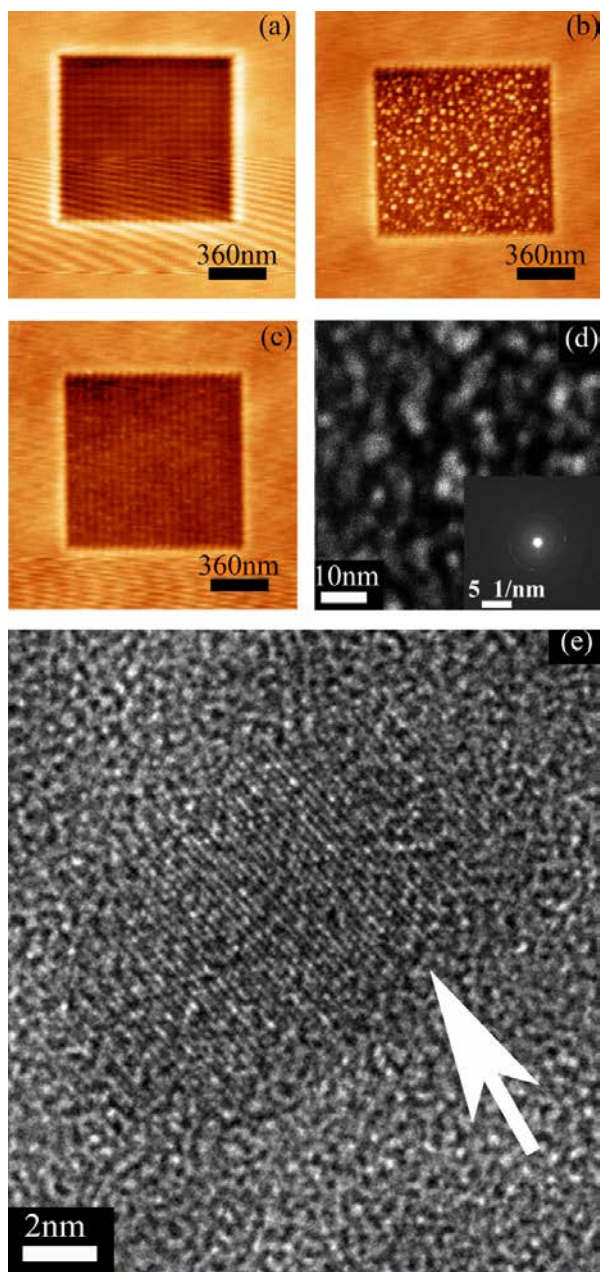


Figure 3.6 (a) AFM 2 x 2 μm image with edges roughly aligned along the $\langle 110 \rangle$ directions for Ga FIB pattern. Accelerating voltage was 30kv and the beam current was 5pA. The total ion dose was 2.9×10^{16} ions/ cm^2 for the 1 x 1 μm patterned square area. (b) 1 x 1 μm milled area after annealing for 1 hour at 600 $^\circ\text{C}$. (c) AFM image of the same patterned area after HCl etching. (d) HAADF image of the Ga nanocrystals formed in the patterned area with insert showing selected area diffraction pattern of the same area. (e) HR-TEM image of Ga nanocrystals showing the Ga lattice fringes inset (d).

As the pattern size is reduced, for the same total number of ions/cm², the number of islands within the pattern area decreases. For a FIB milled region that is 100 nm x 100 nm, a single island is formed inside the pattern area for accelerating voltage as 30 kV. In figure 3.7 (a), similar to figure 3.6 (a), no features are observed in the patterned square before annealing. After annealing, a single Ga island forms in the relatively small pattern area with a diameter of approximately 30 nm. It also appears that small islands may be starting to nucleate just outside the recessed milled area, at the top surface edges of the patterned area. This is likely because of re-deposited material that contains implanted Ga as well. With smaller patterned areas, no Ga islands are observed to form after vacuum annealing. We therefore assume that the total amount of Ga (maximum of 1.63125×10^6 atoms) implanted within this volume is not enough to cause surface nucleation of islands (figure 3.7(c)). The relationship between the average diameter of Ga nanoislands and patterning dose (ions/cm²) fits into a third degree polynomial function (figure 3.7 (d)). Any value that is smaller than 1.0×10^{16} ions/cm² will not lead to surface Ga nanoisland formation after vacuum annealing. To estimate the retained Ga within the nanoislands, we assume a hemispherical shaped Ga islands to calculate the volume of the Ga nanoislands. Here we use the pattern area of 100 x 100 nm and patterning dose of 2.9×10^{16} ions/cm² to calculate the total amount of Ga that impinged upon the patterned area. The result is 2.9×10^6 atoms. The average diameter of the islands is 42.8 nm and there is one Ga nanoisland in this patterned area. The molar mass of Ga is 69.723 g/mol and the density of Ga around room temperature is 5.91 g/cm³. Therefore the total amount of Ga in this nanoisland is 1.06×10^6 atoms. From this calculation, we can estimate that about 37% of the total amount of Ga segregated towards the surface and about 63% of implanted Ga was still within the Si substrate although some may also have been removed due to surface sputtering effects. Since Ga does not

de-sorb for temperatures below 700 °C, there should be no additional loss of Ga due to desorption from the surface during annealing.⁸⁷

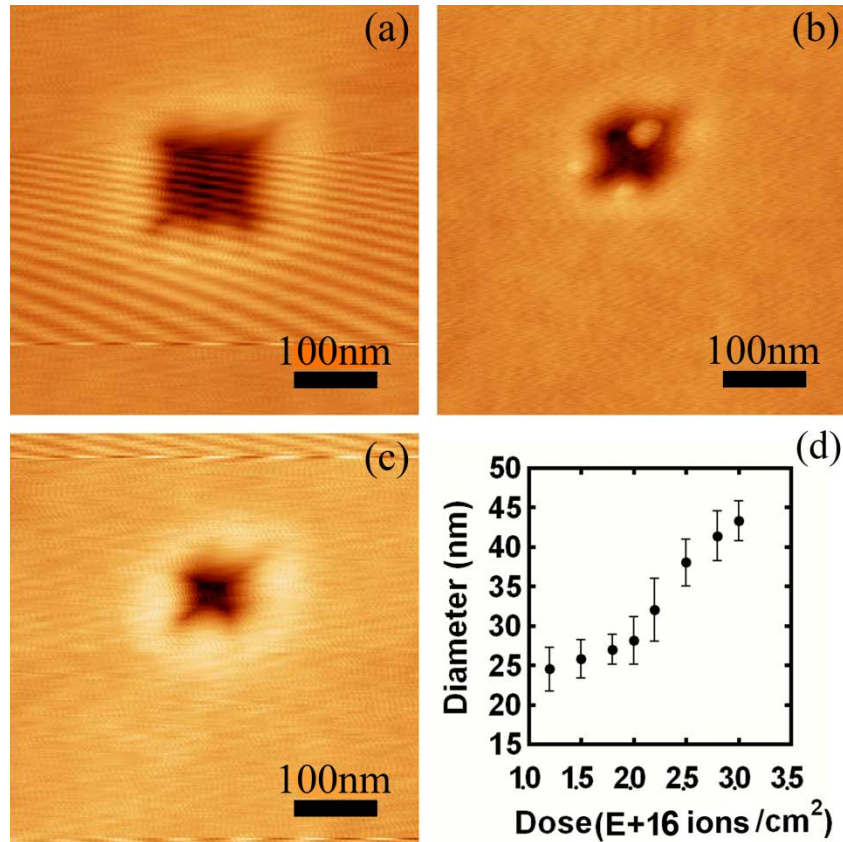


Figure 3.7 (a) AFM 1 x 1 μm image with edges roughly aligned along the $\langle 110 \rangle$ directions for Ga FIB pattern. Accelerating voltage was 30kv and the beam current was 5pA. Total dose was 2.9×10^{16} ions/cm² for the 100 x 100 nm patterned square area. (b) 100 x 100 nm milled area after annealing for 1 hour at 600 °C. (c) 75 x 75 nm milled area after annealing for 1 hour at 600 °C. (d) Diameters of Ga nanoislands as a function of total ion dose.

The experimental results we have obtained so far do not give us any information about the location of the Ga nanodots. Kammler et al.¹¹ have shown the formation of the Ga nanodots underneath the Si surface (figure 3.8 (a)). There are two other possibilities for the formation of nanodots over the patterned area: Ga nanodots are on top of the Si surface capped with a thin layer of Si (figure 3.8 (b)) and Ga nanodots are on the Si surface (figure 3.8 (c)).

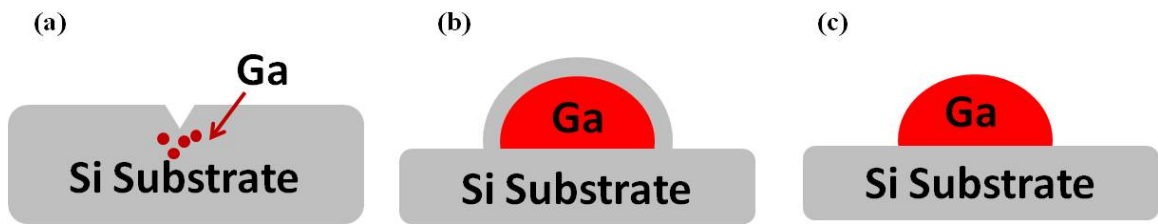


Figure 3.8 Schematic of the positions of Ga nanodots. (a) Ga precipitation underneath the surface. (b) Ga nanodots on the Si surface capped with a thin layer of Si. (c) Ga nanodots on the Si surface.

To confirm that the nanosized islands formed in the patterned area are a result of nucleation of Ga nanocrystals, etching was done using an HCl solution⁸⁸ which etches only Ga but not the Si substrate at room temperature. An AFM topography image of the annealed sample after etching for the same patterned square can be seen in figure 3.6 (c). In figure 3.6 (c), no significant surface islands were seen in the square pattern which now looks more like the pre-annealed image in figure 3.6 (b).

TEM analysis was also done to confirm the formation of Ga nanocrystals in FIB patterned areas. Similar patterns were milled on a single crystal silicon substrate that had previously been mechanically thinned and etched to a thickness that was thin enough to be electron beam transparent in TEM. Both HAADF-STEM and diffraction pattern analysis were

used to prove that the islands seen in the AFM images were Ga nanocrystals and these nanocrystals were formed in the patterned area. The HAADF technique allows Z-contrast imaging and is therefore ideal for imaging elemental information in Ga regions on the Si substrate. In the HAADF mode, electrons are collected by a detector with a large inner radius, which are not Bragg scattered. The intensity of HAADF images is approximately proportional to Z^2 ⁸⁹, and the use of STEM-HAADF images can determine high-Z atoms at low concentration.⁹⁰ A high density of bright dots was detected in the image for the patterned area (figure 3.6 (d)), indicating that these regions are made up of elements heavier than Si, which therefore can only be Ga. The smallest size of gallium crystals seen in the image is approximately 5 to 10 nm. The selected area diffraction (SAD) pattern from the FIB patterned area can be used as another proof of Ga nanocrystalline formation which is also shown in figure 3.6 (d). The crystal structure of single crystal Ga is orthorhombic.⁹¹ The spacing of the rings in the diffraction pattern are indexed as the (021), (131) and (134) planes for the Ga crystal structure and the lattice fringes associated with the nanocrystals can be seen in the high resolution TEM image of figure 3.6 (e). The lattice spacing in figure 3.6 (e) was calculated to be approximately 2.0 Å, which corresponds to the (021) plane. We therefore can conclude that these nanocrystals are in fact Ga. However, the regions next to the Ga nanocrystals do not appear to be crystalline based on the lack of Si lattice fringes in those regions combined with the absence of a Si diffraction pattern. Therefore, the redistribution of Ga towards the surface may not be caused by recrystallization in this case. However, the additional thermal energy provided during annealing may still lead to diffusion and surface segregation.⁸¹⁻⁸³

3.6 EFFECT OF ACCELERATING DOSAGE IN FIB PATTERNING

Next we will examine the effect of accelerating voltage. In the FIB patterning process, the accelerating voltage determines the speed (and the total energy) of the ions passing through the column.⁵⁻⁸

By applying a different accelerating voltage, the speed of the ions will change and as a result the energy of the ions when they arrive at the surface of the sample will be different. With a lower accelerating voltage we expect the implanted Ga to be found nearer to the surface since the energy of the ions will be less and therefore the island sizes and distribution could change. However, the resolution of the 10 kV ion beam will be worse than the 30 kV beam due to the lower accelerating voltage. Therefore we can expect the beam size to be wider, but the total amount of Ga implanted in the whole patterned area should be similar. To investigate the effects of the accelerating voltage, we used a 10 kV accelerating voltage and 5 pA beam current and then compared the results to those shown in figure 3.6. We duplicated the same pattern as before using 2.9×10^{16} ions/cm² and a 1 x 1 μm pattern size. Before annealing, similar features at the bottom of the patterned area were seen in the AFM (figure 3.8 (a)). Like before, only small features at each of the beam dwell positions could be seen as the Ga beam was rastered across the milled area. After annealing, a similar density of Ga islands with a slightly smaller diameter of 39.8 nm and standard deviation of 2.1 nm (compared to 43.4 nm with a standard deviation of 2.5 nm for 30 kV) formed in the patterned square.

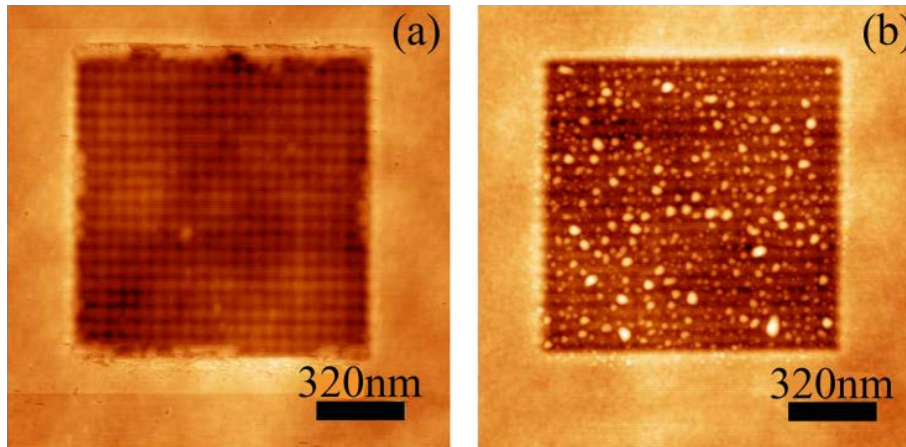


Figure 3.9 AFM 2 x 2 μm image with edges roughly aligned along the <110> directions for Ga FIB pattern. Accelerating voltage was 10kv and the beam current was 5pA. Fluence was $2.9 \times 10^{16}/\text{cm}^2$ for the 1 x 1 μm patterned square area. (b) 1 x 1 μm milled area after a after annealing for 1 hour at 600 °C.

The stopping and range of ions in matter (SRIM 2008 version software) Monte Carlo simulation⁷⁸ was used to simulate the Ga ions behavior under the two different accelerating voltages, using the standard elemental data in the SRIM library, and using 1700 ions per calculation which is based on the diameter of the focused ion beam multiplied by the number of ions/cm² for different accelerating voltages. The parameter set used in the SRIM simulations were as follows: Angle of incidence was 0° (normal incidence), the beam species Ga⁺, beam energy was either 10 or 30 keV, the material was Si and the thickness of sample was 700 Å. From figure 3.11, we observed that the penetration depth for Ga ions at 30 kV is about three times of that at 10 kV. In addition, most of the Ga ions in the 10 kV simulations were concentrated between 10 to 20 nm from the sample surface while in the 30 kV simulation, most of the Ga ions were found in the 15 to 45 nm range.

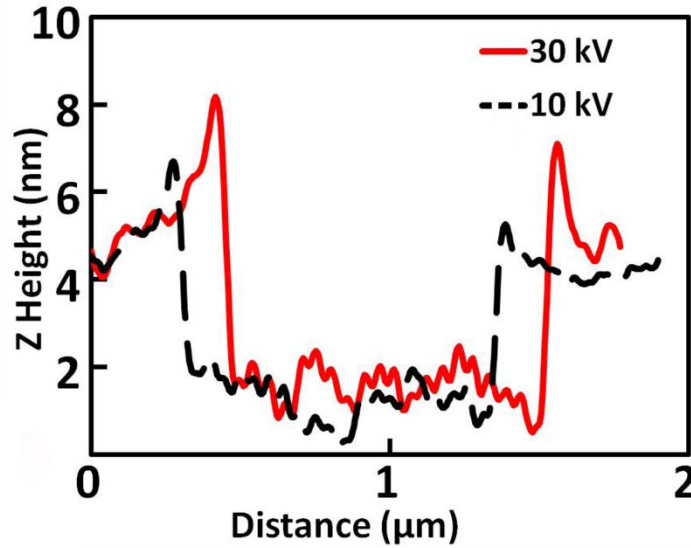


Figure 3.10 Depth profile (obtained from AFM scan) of 1 x 1 μm patterned square area before annealing with different accelerating voltage. Total ion dose was 2.9×10^{16} ions/cm² for the 1 x 1 μm patterned square area.

The SRIM simulation shows the sputtering yield is about 2.0 for 10 kV and about 2.5 for 30 kV accelerating voltage. This small difference in sputtering yield could perhaps explain the slight differences in depth profiles, which can be seen in the AFM scans for the 30 kV (3.8 nm depth) and 10 kV (3.5 nm depth) samples before annealing (figure 3.10). Therefore, only a slightly greater volume of material has been removed by the 30 kV ion beam compared to 10 kV ion beam. From the Monte Carlo simulation in figure 3.11, we observed that the number of Ga atoms trapped within the Si substrate during the patterning process in the 0 to 3.8 nm depth range (with respect to the substrate surface) is much smaller compared to the rest of the Ga implanted by ion beam. We also observed from figure 3.11 that the shape of the 30 kV curve is less Gaussian (more flat). The flatter shape of the curve may due to a relatively greater damage zone that would result from the higher energy (30 kV) of the ions. Hence we can hypothesize that the

similar Ga nanocrystalline islands for the 10 kV and 30 kV samples after the vacuum annealing procedure are caused by the total almost same amount of Ga atoms left in the substrate for the two milling conditions.

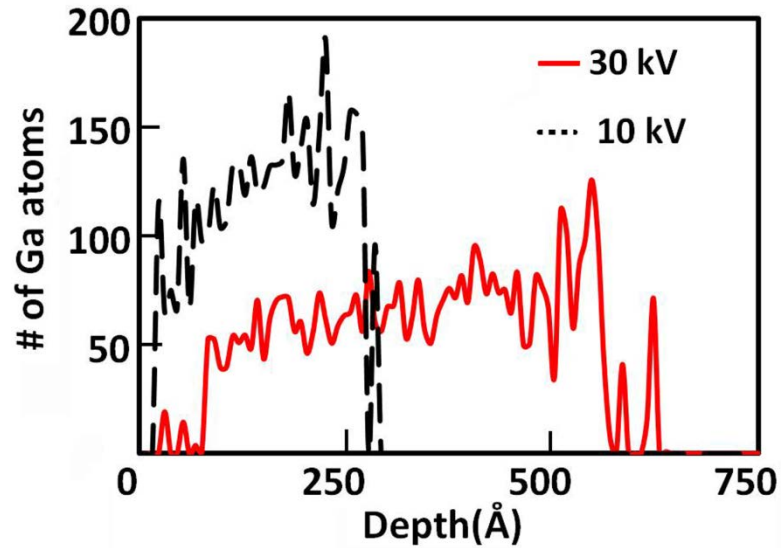


Figure 3.11 SRIM Monte Carlo simulation result of ions trajectories in Si with an accelerating voltage of 30 kV and 10 kV. Total number of ions is 1700.

3.7 DOT ARRAYS GALLIUM TEMPLATES ON SI SUBSTRATE

The Si substrate was also patterned with an array of single point FIB mills as opposed to rectangular area mills. These samples were also analyzed to see if any islands would form upon annealing and if there were any other changes to the surface topography in general after the heat treatment. Another objective of this experiment is to precisely control the formation of Ga nanodots, and attempt to create discrete Ga nanodots with the help of dot array patterns. Based on the discussion in previous sections, relatively higher dosages were applied in this experiment after carefully considering that the patterned area for each dot was very small. The dosages used ranged from 30×10^{15} to $120 \times 10^{15}/\text{cm}^2$ and included two different beam currents, 1pA and 10pA.

Representative AFM images of before and after annealing for two of the patterning conditions can be seen in figure 3.12. In all cases, there were no new islands or changes to the patterns observed in the AFM images after annealing. For low dosages and 1pA beam current (figure 3.12 (a)), only surface swelling was seen at the milled point due to amorphization of the crystalline silicon. This result is new compared to the pre-annealing data from the trench patterns. For this low beam current, the dosage needs to be approximately twice the value ($60 \times 10^{15}/\text{cm}^2$) before a crater starts to be seen in the substrate surface. For larger beam currents, such as was shown in figure 3.12 (c), crater formation at the milled site happened more quickly and a slightly raised amorphous ring formed around the crater. In either case, no changes were seen in the surface topography after heating the point mill samples for any of the conditions. The reason could be too few Ga atoms have been implanted into the substrate even though the dosage was high. However, this does not preclude the formation of subsurface Ga clusters.¹¹

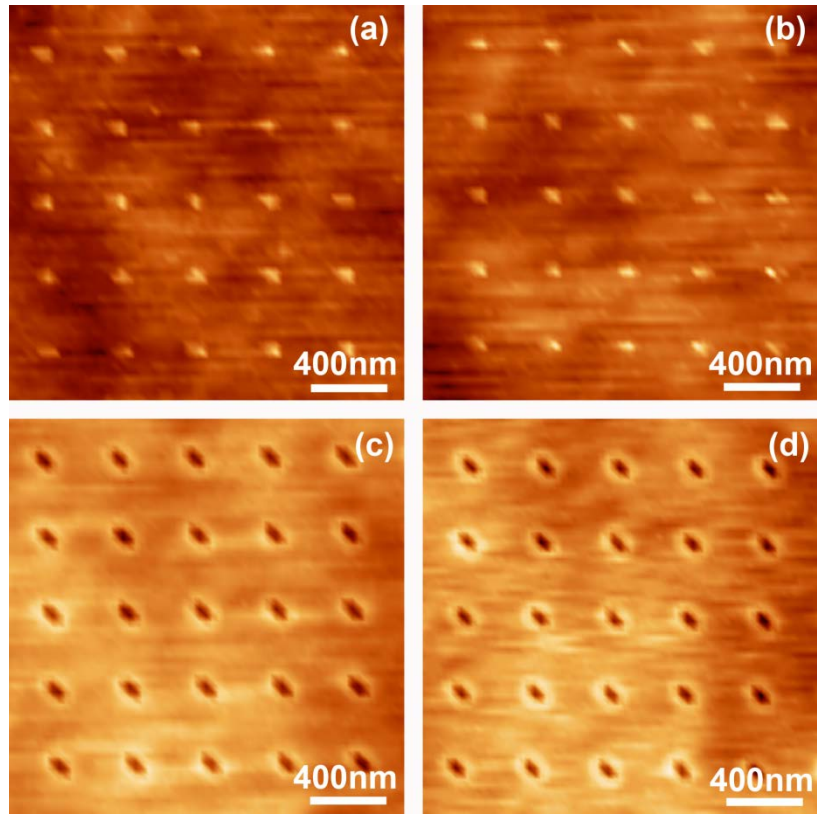


Figure 3.12 AFM images of (a) 1 pA beam current, $30 \times 10^{15}/\text{cm}^2$ dosage point mills before and (b) after anneal. The z-scale for both images is 8.5 nm. (c) 10 pA beam current, $60 \times 10^{15}/\text{cm}^2$ dosage point mills before and (d) after anneal. The z-scale for both images is 10.2 nm.

3.8 CONCLUSIONS FOR THE GALLIUM NANODOTS FORMATION

Formation of crystallized gallium nanodots on silicon substrates has been achieved with the aid of a focused ion beam system using the gallium ion beam as the source of gallium. Different ranges of dosages and templates were used to investigate the size of the Ga nanodots within the trenches. In contrast, Ga nanodots were not detected when the same procedure was repeated using a bit map dot array technique. The reason could be the insufficient area available within

the individual dots in the array, which means the total amount of Ga is not enough at each patterned site. Our conclusions at this point are that the Ga nanodots can be observed after one hour vacuum annealing at 600 °C. The concept of a linear relationship between the diameter of Ga nanodots and the dosages or trench width of the patterned area is also demonstrated in our study.

The contrast in HAADF images observed from the trenches indicates that crystallized Ga nanodots have been formed. The lattice fringes in the HRTEM images also provided evidence for crystallized Ga nanodot formation. We also observed a difference in the size of the Ga nanodots when comparing AFM and TEM data. This change in size could possibly arise from differences in the surface diffusion mechanism of the Ga atoms on the Si substrates that are either crystalline or amorphous. Our experimental observations also agreed with the Monte Carlo simulations that were performed using the appropriate parameters.

We have demonstrated that nucleation of gallium nanoislands directly on commercial silicon (001) substrates can be achieved with the aid of a FIB system using the Ga ion beam as the source of gallium. For proper FIB milling conditions, Ga nanoislands can be observed to form after one hour vacuum annealing at 600 °C. A single discrete Ga surface island can be achieved by carefully reducing the pattern size. Preferential chemical wet etching and TEM analysis have provided substantial proof of the nanocrystalline Ga formation at the surface of the silicon. We have also shown that the substantial decrease in accelerating voltage of the Ga ions has little effect on the island nucleation process. These results confirmed the feasibility of using the FIB as means of directly forming nanocrystalline islands at specific surface locations on a commercial silicon substrate.

4.0 NITRIDATION PROCESS OF GALLIUM NANOISLANDS

We have previously demonstrated conditions under which gallium quantum dot templates will form on the surface of an undoped silicon substrate using a focused ion beam direct patterning method.⁹² The number and size of the Ga surface islands that form upon annealing the implanted Si substrates can be tailored by adjusting the ion dose and pattern sizes. In these experiments, we will investigate nitridation of the Ga surface islands using nitrogen plasma.

Si (001) substrates were used for all of the experiments in the study. The silicon wafers were cleaned ultrasonically in acetone for approximately 10 minutes followed by isopropyl alcohol (IPA) for another 10 minutes before loading them into the dual beam FIB (Seiko Instruments SMI3050SE FIB-SEM). The substrates were patterned in the dual beam FIB using an accelerating voltage of 30 kV and a beam current of 5 pA. The dosage was kept at 2.9×10^{16} for all these experiments. The patterned samples were then loaded into a vacuum chamber with a base pressure of 9×10^{-10} Torr and annealed at 600 °C for 1 h. This annealing time and temperature was chosen based on previous reports found in the literature of Ga droplet formation on SiO₂ and our previous experiments on Si.^{76,92} In addition, Ga desorbs above 700 °C⁹³, which causes Ga loss, so the annealing temperature must be kept lower than this temperature.

4.1 NITRIDATION PARAMETERS

The patterned samples were characterized using atomic force microscopy (AFM) and then cleaned again ultrasonically in acetone and IPA for another 10 minutes before being loaded into the vacuum chamber for the following nitridation process. Nitridation of the Ga islands was achieved by creating a nitrogen plasma by RF biasing the substrate at 5 W. Different N₂/Ar gas ratios were tried including 1:2, 1:1 and 2:1. The total mixed gas pressure during the nitridation process was 3×10^{-2} Torr. The substrate temperature was kept at 500 °C and a total plasma nitridation time was 5 minutes. During the N₂ plasma nitridation process, the sample was also heated to provide the Ga atoms and N ions enough energy to overcome the thermodynamic energy barrier of forming GaN. However, we keep the temperature lower than that in the previous annealing step to prevent any additional evolution of the nanoisland surface morphology.⁹⁴ Growth temperatures that are too low (like room temperature) would potentially result in amorphous structures due to the lack of energy needed to overcome the barrier to form the crystalline structure.⁹⁵

An atomic force microscope (AFM) (Digital Instruments Dimension TM 3100 operated in tapping mode) was used to characterize the surface topography of all the samples before annealing, after annealing and post nitridation.

The samples were first coated with carbon coater for 15 seconds. The plan view TEM samples were made using a dual-beam focused ion beam/scanning electron microscope. The first step of making a plan view TEM sample is similar to that in the the standard FIB cross-section sample preparation procedures in which the sample is removed from the substrate using the lift-out technique. We then rotated the sample for 90 degrees before mounting it onto the TEM grid.

After the sample had been mounted on the TEM grid (after the rotation, the back side of the sample was exposed to the ion beam), we used Ga ion beam to thin the sample from the back side to reach the thickness which is electron transparent in TEM.⁷³ At the end, carefully cleaning the front side of the sample can remove the protective coatings without milling away the GaN islands.

4.2 RESULTS WITH DIFFERENT NITROGEN/ARGON RATIO

Clear evidence for island formation after annealing the FIB patterned samples can be seen by comparing the AFM topography image of the square milled patterns before and after annealing. The pattern was created with a total ion patterning dose of 2.9×10^{16} ions/cm², a 5 pA beam current, and 30 kV accelerating voltage in the FIB. In figure 4.1(a), there were not any significant features in the square patterned area before annealing. Also, from the AFM image it can be seen that overall, material was being removed from the patterned area under these milling conditions since the milled area is at a lower overall depth from the color contrast in the image. After annealing, it can be seen in the AFM images that islands formed in the square area (figure 4.1(b)). The mechanisms of the formation of surface Ga nanoislands and the characterization of the Ga islands have been investigated in previous studies⁹².

4.2.1 N₂/Ar gas ratios as 1:1

After carrying out the nitridation process with N₂/Ar gas ratios as 1:1 at 5 W substrate bias, no significant topography change can be observed in the patterned area (figure 4.1(c)). The size of

the surface nanoislands formed under these specific patterning conditions ranges from 20 nm to 70 nm.

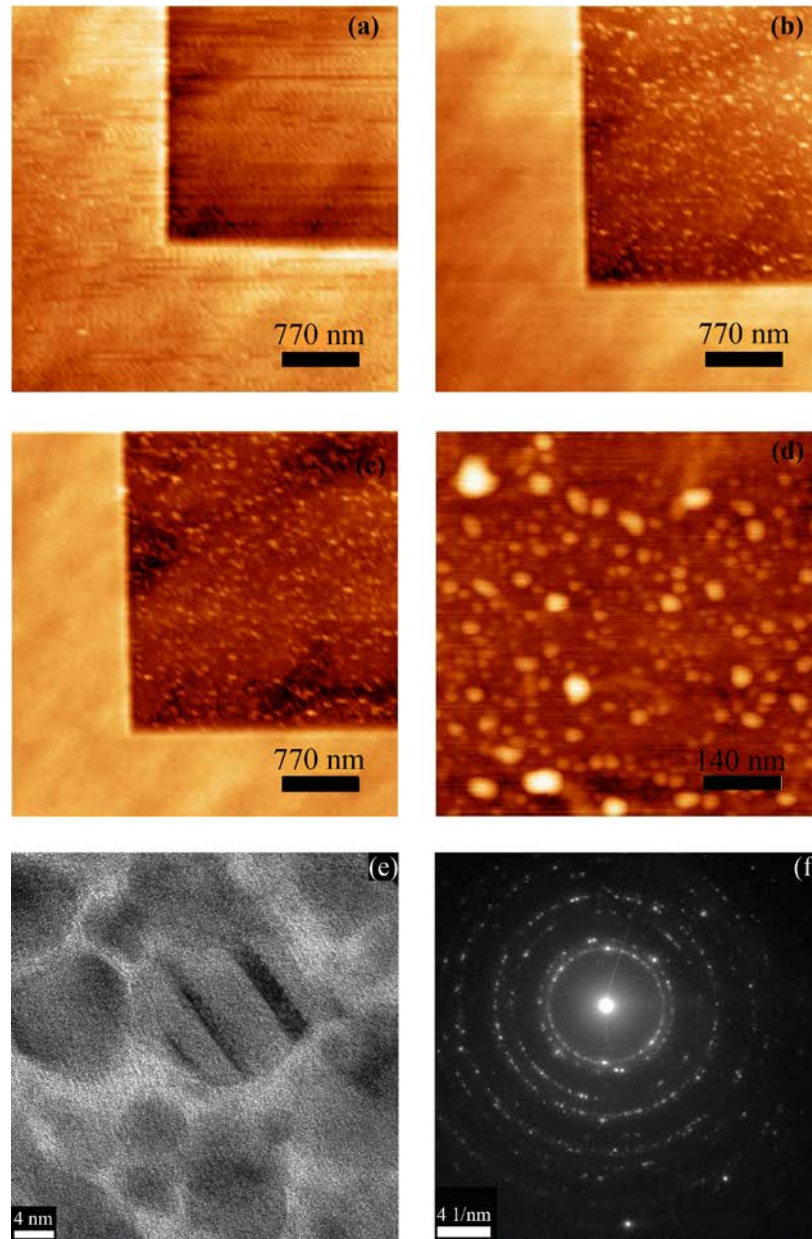


Figure 4.1 (a) AFM 15 x 15 μm image with edges roughly aligned along the <110> directions for Ga FIB pattern. Accelerating voltage was 30kv and the beam current was 5pA. The total ion dose was 2.9×10^{16} ions/cm² for the 10 x 10 μm patterned square area. (b) 10 x 10 μm milled area after annealing for 1 hour at 600 °C. (c) AFM image of the same patterned area after exposure to nitrogen plasma with N₂/Ar ratio as 1:1 for 5 minutes at 500°C. (d) 1 x 1 μm zoomed in scan in the same area after nitridation process. (e) HR-TEM image of GaN nanocrystals showing the GaN lattice fringes. (f) Selected area diffraction pattern of the same area.

TEM analysis was also done to confirm the formation of GaN nanocrystals in FIB patterned areas after nitridation process. The selected area diffraction pattern was indexed to prove that the islands seen in the AFM images were GaN nanocrystals that were formed in the patterned area. The lattice fringes associated with the nanocrystals can be seen in the high resolution TEM image of figure 4.1(e). Multiple crystals were selected to be included in the selected area diffraction (SAD) analysis. The crystal structure of GaN nanoislands determined from the SAD pattern is the rock-salt cubic structure, which has previously been found to form under high pressure conditions.⁹⁶ It has been reported that the phase transformation from the wurtzite to the rocksalt cubic phase begins at 37 GPa.⁹⁶ The Ga-Ga distances of the GaN sample in wurtzite and rocksalt phases during the phase transformation are 3.03 ± 0.02 Å and 2.84 ± 0.02 Å at 40 GPa.⁹⁶ Such a decrease in the Ga-Ga distance during the wurtzite-to-rocksalt phase transformation is initiated by the pressure-induced charge transfer (connected with changing the ionicity and electronegativity inside the GaN)⁹⁶. In our experiment, there was no external pressure applied during the process and the Ga nanoislands possess the orthorhombic structure before the nitridation process.⁹² Every Ga atom has one very close neighbour at 2.44 Å and six other atoms only a little further away at 2.71-2.79 Å.⁹² The whole system only needs to overcome a smaller lattice distortion energy barrier to form the rock-salt cubic phase GaN compared to a relatively larger lattice deformation to fit the wurtzite phase GaN.

Growth of GaN thin films⁹⁷ and nanorods⁹⁸ using a gallium target and N₂ plasma have been reported. The wurtzite GaN nanorods⁹⁸ can be obtained through radio frequency magnetron sputtering system with pure metal Ga target and N₂/Ar as reactive gas on Si (111) substrates. In this case discussed above, both the Ga and N atoms have the ability to move freely on the substrate's surface. In our experiments, since the Ga nanoislands already presented on the Si

substrate, in other words, the Ga nanoislands were confined on the surface, and therefore Ga atoms don't have the ability to diffuse freely on the surface. This can also explain why we didn't observe a topography change before and after the nitridation process.

The impact of the reactive mixed gas N_2/Ar ratio was also investigated to see if the ratio has any influence over the shape or crystal structure of the islands. For example, for the slightly different case reactive sputtering of Ga and ammonia, it has been reported that the Ga/N ratio may dominate the surface morphology of the film⁹⁸ and allow the optical properties to be altered without changing the GaN crystal structure.⁹⁹ This is explained that how the Ga/N ratio changes can influence the growth front and thus lead to different morphology.¹⁰⁰ Under Ga rich conditions, the lateral growth rate is high due to the high mobility of Ga atoms and thus resulting in the formation of a continuous film. On the other hand, nanorods form under nitrogen rich conditions.

4.2.2 N_2/Ar gas ratios as 2:1 and 1:2

In our experiments, for N_2 rich condition ($N_2/Ar = 2:1$) and Ar rich condition ($N_2/Ar = 1:2$), there were no topography changes seen in the AFM images between before and after nitridation for both gases (figure 4.2 (a, b) and figure 4.3 (a, b)). In our study, the situation is different from that of reactive sputtering, we have a fixed amount of Ga atoms reacting with a varying supply of nitrogen. However, the change in ratio of fixed Ga to nitrogen arriving at the surface of the Ga nanoislands is insignificant. Thus, as we expected, the small difference in N atomic concentration did not play a dominant role in the morphology of the GaN nanoislands.

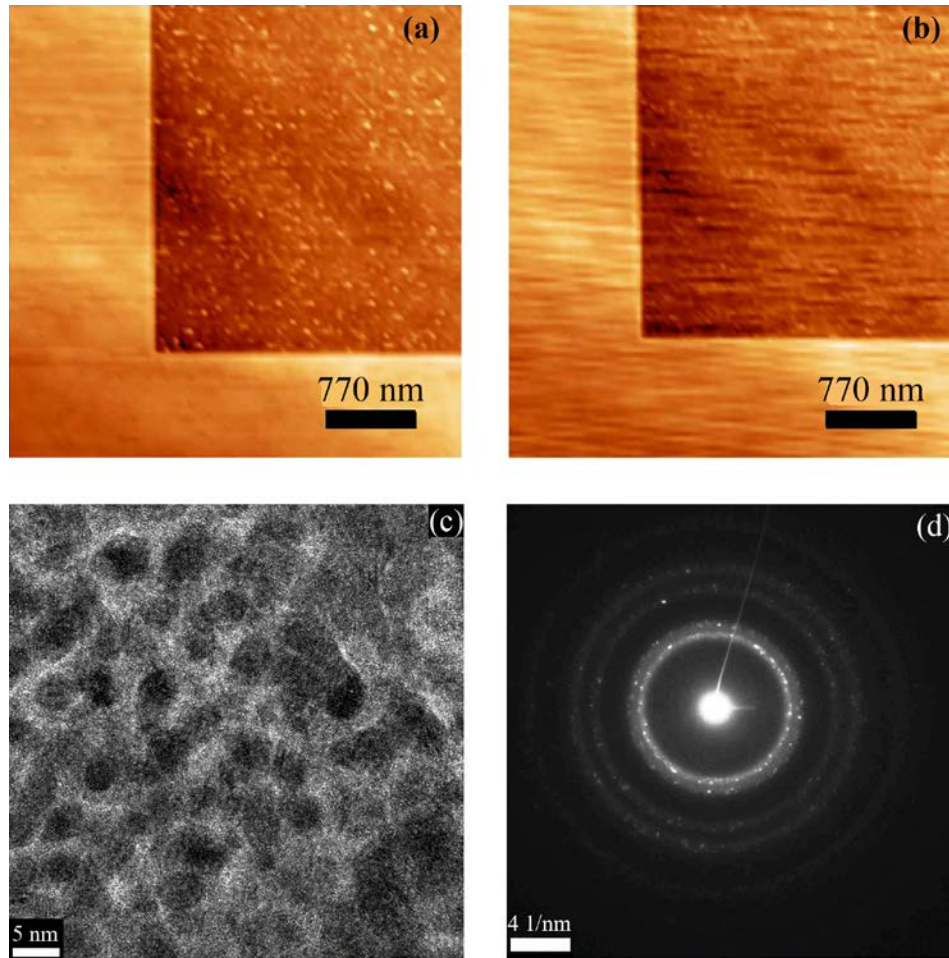


Figure 4.2 (a) AFM 15 x 15 μm image for the 10 x 10 μm FIB patterned square area after annealing for 1 hour at 600 $^{\circ}\text{C}$ with edges roughly aligned along the $\langle 110 \rangle$ directions. Accelerating voltage was 30kv and the beam current was 5pA. The total ion dose was 2.9×10^{16} ions/ cm^2 . (b) AFM image of the same patterned area after exposure to nitrogen plasma with N_2/Ar ratio as 2:1 for 5 minutes at 500 $^{\circ}\text{C}$. (c) HR-TEM image of GaN nanocrystals showing the GaN lattice fringes. (d) Selected area diffraction pattern of the same area.

Also, in our experiments, as opposed to the reactive co-sputtering case, the diffusion of Ga atoms was limited by their incorporation into the previously formed Ga nanoislands, whereas, the N atoms can be considered to have unlimited mobility. This can also explain why we did not

see the islands evolve into a continuous film as reported by Liu et. al for the case of reactive co-sputtering.⁹⁸

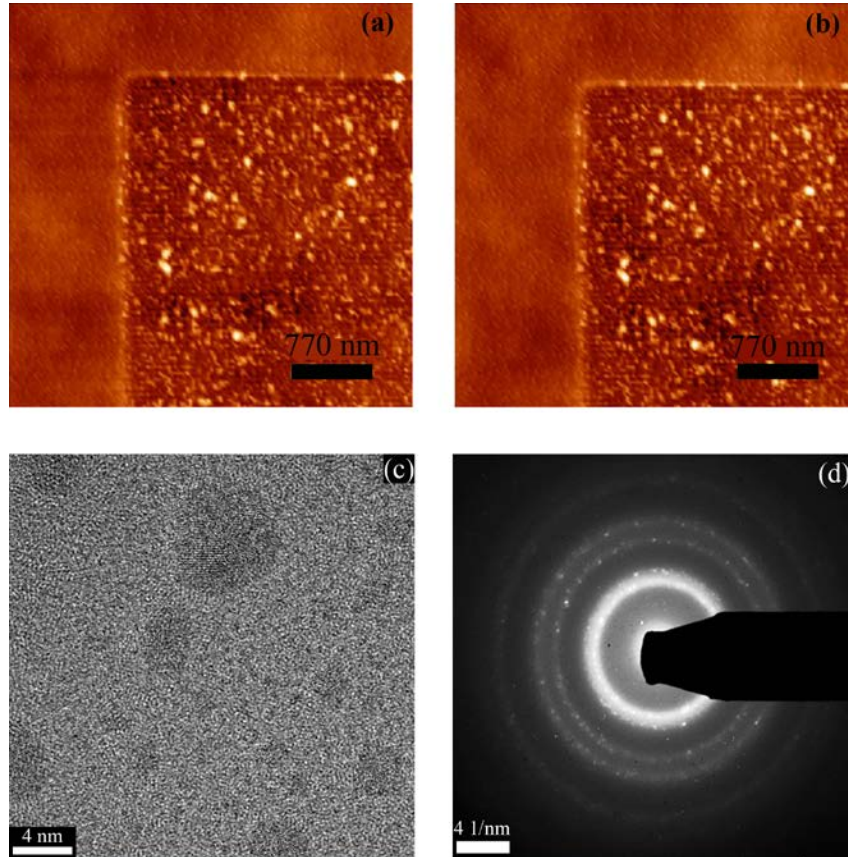


Figure 4.3 (a) AFM 15 x 15 μm image for the 10 x 10 μm FIB patterned square area after annealing for 1 hour at 600 $^{\circ}\text{C}$ with edges roughly aligned along the $\langle 110 \rangle$ directions. Accelerating voltage was 30kv and the beam current was 5pA. The total ion dose was 2.9×10^{16} ions/ cm^2 . (b) AFM image of the same patterned area after exposure to nitrogen plasma with N_2/Ar ratio as 1:2 for 5 minutes at 500 $^{\circ}\text{C}$. (c) HR-TEM image of GaN nanocrystals showing the GaN lattice fringes. (d) Selected area diffraction pattern of the same area.

The lattice fringes associated with the nanocrystals were observed in the high resolution TEM images from both N rich and Ar rich conditions (figure 4.2 (c) and figure 4.3 (c)). The SAD pattern from the FIB patterned area also proved the crystalline structure didn't change by

tuning the N₂/Ar ratio. Both conditions showed the formation of rock-salt cubic phase GaN (figure 4.2 (d) and figure 4.3 (d)).

4.3 CONCLUSION FOR GALLIUM NITRIDE FORMATION

We have demonstrated that nucleation of gallium nanoislands directly on commercial silicon (001) substrates can be achieved with the aid of a FIB system using the Ga ion beam as the source of gallium. Ga nanoislands can be observed to form after one hour vacuum annealing at 600 °C. We are able to convert the Ga to a rock-salt cubic GaN structure, which has previously be found to form under high pressure conditions This can be proved by TEM diffraction pattern analysis of plan view samples. These results confirmed the feasibility of using the FIB as a means of directly forming nanocrystalline islands of Ga-based compounds at specific surface locations on a commercial silicon substrate.

5.0 SIGE QUANTUM DOTS FORMATION

Zero-dimension quantum dot structures are critical for new device structures that can utilize their discrete energy spectrum and few-carrier effects. There has been a lot of research carried out in synthesizing quantum dots in general¹⁰¹; however, precise lateral control the position of quantum dots directly on silicon, the most technologically important substrate, is still a challenge.

Si (001) substrates were used for all of the experiments in the study. The silicon wafers were cleaned ultrasonically in acetone for approximately 10 minutes followed by iso-propyl alcohol (IPA) for another 10 minutes before loading them into the dual beam FIB. The substrates were patterned in the dual beam FIB using an accelerating voltage of either 30 kV or 10 kV and a beam current of 5 pA. The total number of Ga ions/cm² impinging on the surface during FIB patterning, commonly referred to as dose or fluence, was varied to investigate the effect on the Ga islands' size. The total number of Ga ions/cm² depends on the ion beam current used and milling time.

5.1 HIGHLIGHTS IN SILICON-GERMANIUM QUANTUM DOTS FORMATION

PROCEDES

A set of unannealed patterned samples was used for further SiGe deposition experiments. The dosage applied in this experiment ranged from $0.2 \times 10^{15}/\text{cm}^2$ to $20 \times 10^{15}/\text{cm}^2$ (number of ions/ cm^2). The substrates were first ultrasonically cleaned in acetone and IPA. Then a modified Shiraki cleaning procedure was applied. The wafers were first immersed in the acid solution ($\text{H}_2\text{SO}_4/\text{H}_2\text{O}_2$ at $\sim 85^\circ\text{C}$, mixing ratio 4:1) for 5 to 7 minutes, and then rinsed in ultrapure (18 M Ω cm of resistivity) de-ionized water (DI water) for 2 minutes. This was followed by a dip in a buffer oxide etch (BOE, $\text{NH}_4\text{F}/\text{HF}$ at room temperature, mixing ratio 6:1) for 15 seconds and another rinse in DI water for 5 minutes. The second stage of the cleaning was performed using the RCA method¹⁰² in which an oxide layer is repeatedly formed and stripped off. This was done by first boiling the wafers in a $\text{H}_2\text{O}/\text{HCl}/\text{H}_2\text{O}_2$ solution (mixing ratio 4:1:2) at $\sim 85^\circ\text{C}$, rinsing in DI water, and then dipping into BOE for 15 seconds to remove the oxide. This procedure was repeated twice and ended with the BOE step. Finally, the samples were rinsed in DI water for 10 minutes before being loaded into the sputtering system. This process should produce a hydrogen-terminated surface, free of oxides. The samples were then heated overnight at 200°C for out gassing.

$\text{Si}_{0.7}\text{Ge}_{0.3}$ films were then deposited using magnetron sputtering on the chemically cleaned Si (001) substrates. The base pressure of the chamber was 9×10^{-10} Torr, and the process pressure was 3×10^{-3} Torr. High purity Ar gas (99.999% pure, purchased from Valley National Gas company) was used then purified to part-per-billion levels with an in-line purifier. The Si

and Ge targets were 2" in diameter with purity of 99.999% (purchased from Kurt J. Lesker Company). A 65 Å Si buffer layer was first deposited at 450 to 550°C with a deposition rate of approximately 0.1 Å/s using RF power. Then Si_{0.7}Ge_{0.3} film was deposited at 450 to 550°C with the total growth rate of 0.5 and 1 Å/s, using DC and RF power for Ge and Si respectively. The temperature and growth rate were chosen to try to prevent islanding from occurring at non-patterned sites, which would otherwise occur due to strain relaxation at more near-equilibrium conditions.¹⁰³

To achieve the ultra-high vacuum and epitaxial growth, we need both low base pressure and no hydrocarbon peaks in the residual gas analyzer (RGA). While increasing the substrate temperature, we recorded the RGA data to monitor the gas content in the UHV chamber. From table 5.1, we can observe that until 500 degree, there are still not significant peaks for hydrocarbons compared with the background at 1×10^{-10} Torr (at mass number 40 and 43). After ramping up the temperature over 600 degrees, the peak for hydrocarbons became non-neglectable. That may due to the plastic wires in our chamber starting to release hydrocarbons at these higher temperatures.

Therefore, to maintain the UHV and the purity in the chamber, it is also important that we not go beyond 600 degrees for the thin film growth in order to good crystallinity.

Table 5.1 Hydrocarbons peak height from RGA data at different temperatures.

Temperature Mass Number	25°C (Torr)	500°C (Torr)	600°C (Torr)	700°C (Torr)
40	1×10^{-10}	2×10^{-10}	1×10^{-9}	2.5×10^{-9}
43	1.5×10^{-10}	3×10^{-10}	9×10^{-10}	2×10^{-9}

5.2 SILICON BUFFER GROWTH

The deposition of a Si buffer layer is done to minimize any impact from Ga or contamination still present after cleaning. It also could provide a fresh surface for in-situ SiGe alloy growth. Thus it is very important to achieve a flat and epitaxial Si buffer layer before the deposition of the SiGe thin film. All the samples in this chapter need to go through the thoroughly chemical cleaning procedure discussed in section 2.3 to remove all the possible contaminations before loading into the main chamber.

A 65 Å Si buffer layer was first deposited at 500 °C with a deposition rate of approximately 0.1 Å/s using RF power. This carefully chosen low growth rate is another method to achieve the epitaxial buffer layer.

(Multiple growth condition trials for Si buffer layer can be found in Appendix A1.)

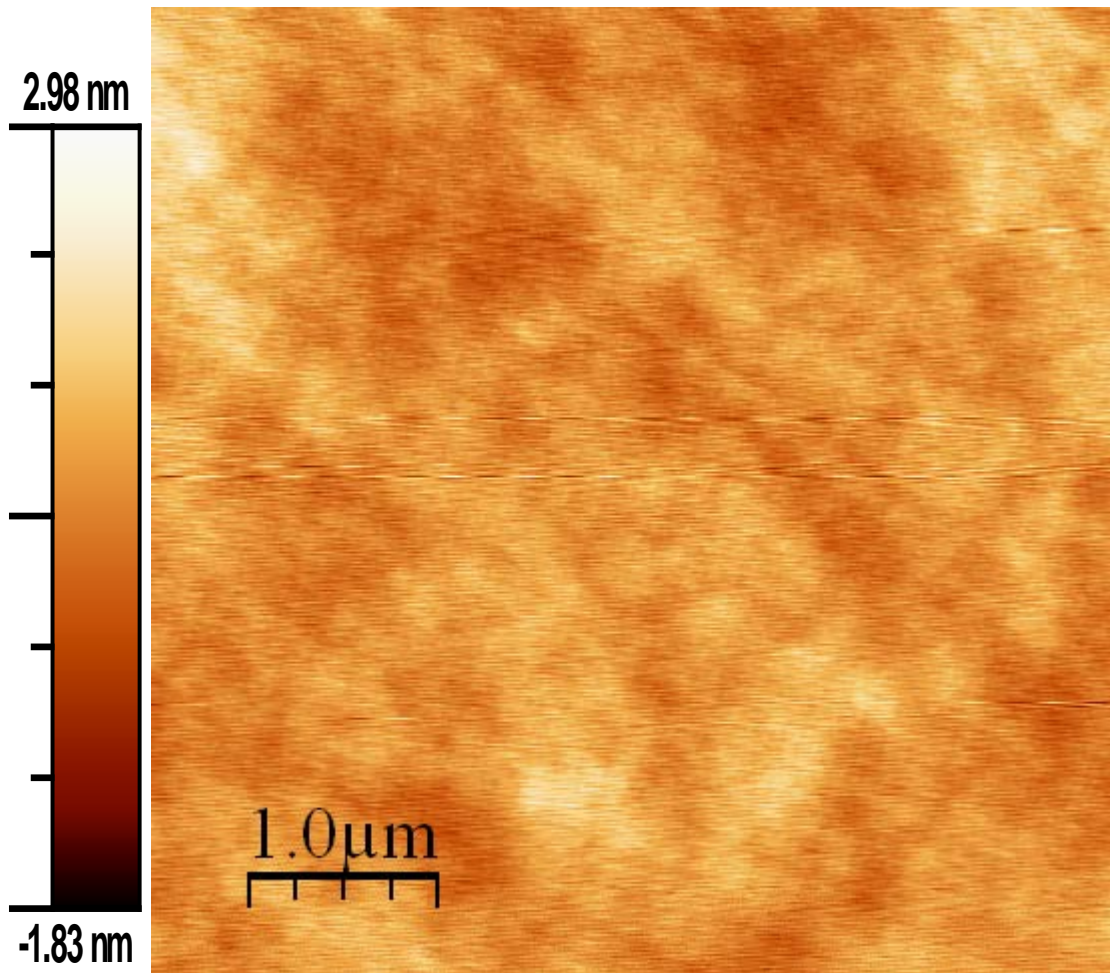


Figure 5.1 65 nm Si buffer layer grown at 500 °C.

5.3 SIGE QUANTUM DOTS GROWTH ON SI WAFERS

Since no change in surface features were visible in the figure 3.12 upon heating these single point milled arrays, this type of low dose patterning is has the potential application for subsequent deposition of a lattice mismatched material such as SiGe onto the patterned templates. In this experiment, the changes in topography at these milled sites may act as preferential nucleation sites for islands to form.

There is a three stage procedure that is performed to ensure that there is no island formation from implanted Ga post FIB patterning. First, the dosages were varied from $0.2 \times 10^{15}/\text{cm}^2$ to $20 \times 10^{15}/\text{cm}^2$. The dosages used in these experiments were even lower than those used to form Ga nanodots. Second, the substrate underwent a chemical cleaning process that consisted of multiple surface oxidization and oxide removal steps after FIB patterning. This ensures access to pristine Si surface. Third, deposition of a very thin (~7 nm) Si buffer layer minimizes any impact from possible leftover Ga atoms trapped within the patterned area. The buffer layer also eliminates remnant contaminants post the chemical cleaning process. The growth temperature for both the buffer layer and the SiGe depositions should never above 550 °C. This temperature range is well below the Ga nanodot formation temperature of 600 °C.

5.3.1 10 nm Si_{0.7}Ge_{0.3} growth on 6.5 nm Si buffer layer at 500 °C and 0.5 Å/s

From figure 5.2, it is observed that there is no pit formation at the low dosage of $1 \times 10^{15}/\text{cm}^2$. For the low dosages that were used, only discrete islands were formed at the damage site. These

islands are typically much larger than those were expected to form from substrate amorphization due to FIB patterning.

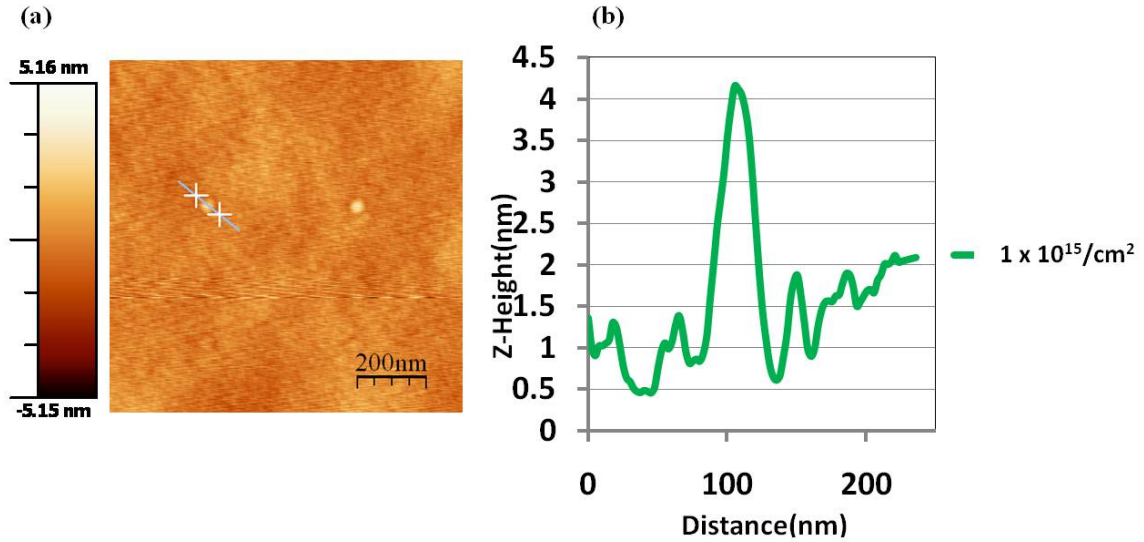


Figure 5.2 (a)AFM images of $1 \times 10^{15}/\text{cm}^2$ dosage point arrays mills after SiGe alloy growth. (b) Profile data of the quantum dot. The sample's edge is roughly aligned along the $\langle 110 \rangle$ direction.

When intermediate dosages ($6 \times 10^{15}/\text{cm}^2$) were tried, a series of continuous rings were observed around the damage sites as seen in figure 5.3. The height of the observed rings was 1.82 ± 0.6 nm with an outside wall angle of 6.52° . The angle of pit sidewall was measured to be 31.0° . TEM diffraction will be done in order to determine the crystalline state.

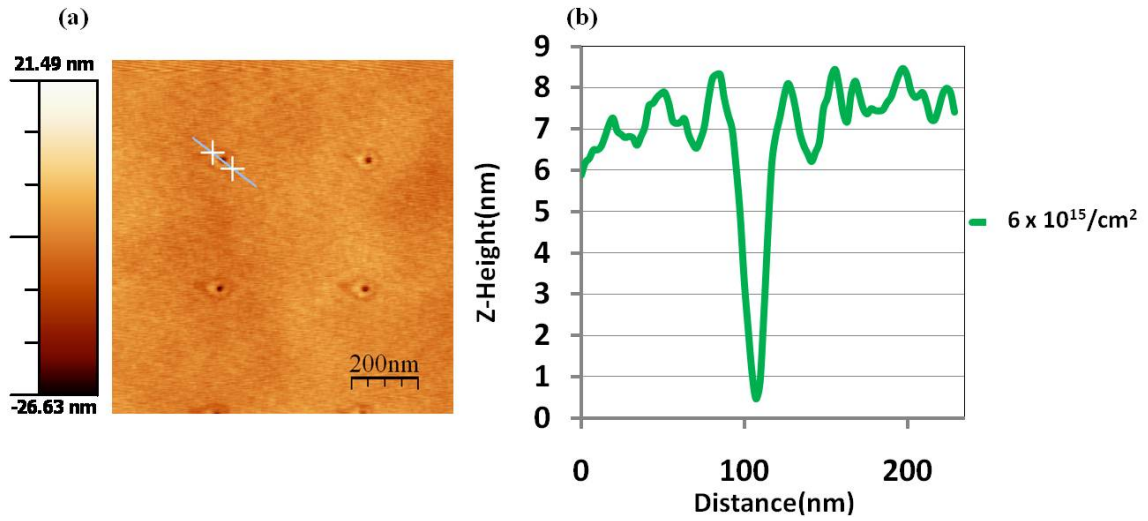


Figure 5.3 (a) AFM images of $6 \times 10^{15}/\text{cm}^2$ dosage point arrays mills after SiGe alloy growth. (b) Profile data of the quantum dot. The sample's edge is roughly aligned along the $\langle 110 \rangle$ direction.

With higher dosages ($20 \times 10^{15}/\text{cm}^2$), the island formation was confined to the interior floor of the pits. In figure 5.4, the pit depth which is likely to act as “trap”, confined the diffusion of Ge, so that they were forced to form islands at the bottom of the pits.

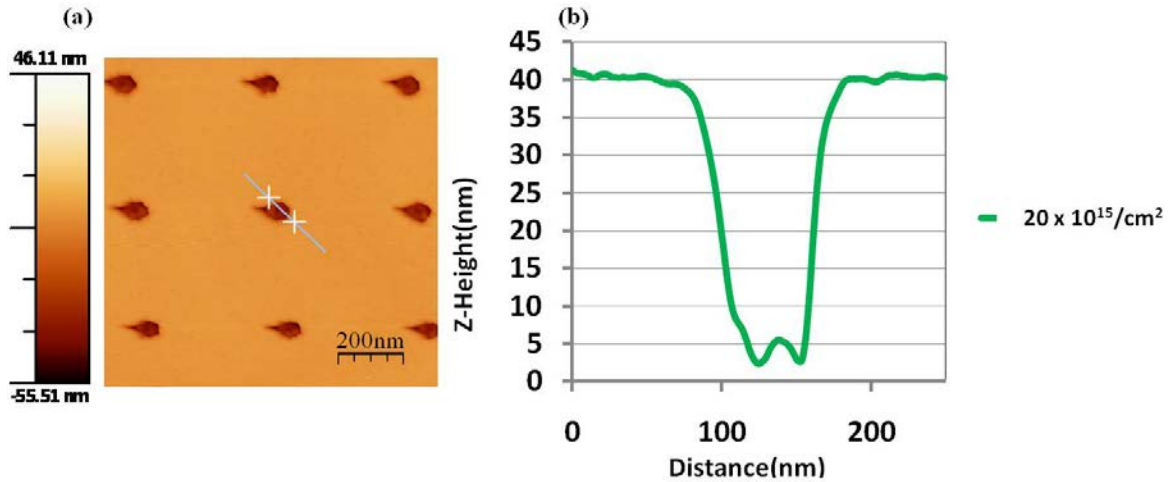


Figure 5.4 (a) AFM images of $20 \times 10^{15}/\text{cm}^2$ dosage point arrays mills after SiGe alloy growth. (b) Profile data of the quantum dot. The sample's edge is roughly aligned along the $\langle 110 \rangle$ direction.

5.3.1.1 10nm Si_{0.7}Ge_{0.3} growth on 6.5nm Si buffer layer at different conditions

In order to figure out the influence of growth temperature and growth rate on the formation of SiGe quantum dots, more experiments were carried out. For ease of comparison, we chose the same dosage ($6 \times 10^{15}/\text{cm}^2$) but under different growth conditions. From figure 5.5(a), at the higher growth temperature of 550 °C, we observed a relatively rougher surface compared to figure 5.3(a) and non-continuous rings. This higher surface roughness could be attributed to increased surface diffusion of the atoms on the substrate. In order to minimize the surface roughness effect, a higher growth rate of 1 Å/s was used for this temperature of 550 °C.

For a given thickness, a higher growth rate will decrease the growth time. The shorter growth time could help suppress the excessive diffusion of the SiGe atoms. A higher growth rate of 1 Å/s in combination with the higher growth temperature could not overcome the undesirable surface diffusion effect, as seen in figure 5.5 (a). At a lower growth temperature of 450 °C and

0.5 Å/s, no ring formation was seen (figure 5.5 (b)). The protuberance features in figure 5.5 (b) was from the amorphization during the patterning process. The phenomena observed here could perhaps be due to the lack of enough thermal energy to overcome the activation energy barrier of the surface diffusion process.

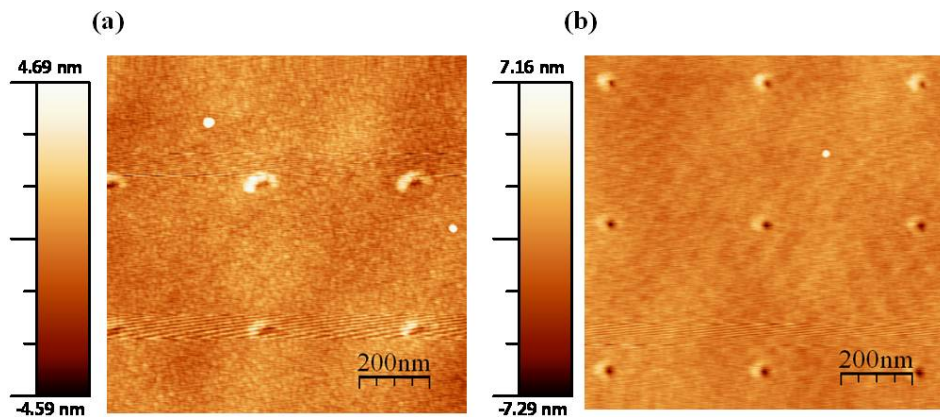


Figure 5.5 AFM images of $6 \times 10^{15}/\text{cm}^2$ dosage point arrays mills after SiGe alloy growth. (a) SiGe alloy grown at 550 °C with total growth rate of 1 Å/s. (b) SiGe alloy grown at 450 °C with total growth rate of 0.5 Å/s. The sample's edge is roughly aligned along the $\langle 110 \rangle$ direction.

5.3.2 RHEED results for 10nm $\text{Si}_{0.7}\text{Ge}_{0.3}$ growth on 6.5 nm Si buffer layer at 500 °C and 0.5 Å/s

Based on the AFM results and how they differ from previously reported MBE, we suspected that the deposited films may not be single-crystal. Recently, a RHEED system has been added to the sputtering system. The RHEED (Reflective high-energy electron diffraction) technology is utilized in-situ to determine the surface crystallinity, especially for epitaxial growth of thin

films.⁶¹ A RHEED system requires an electron source (gun), a photoluminescent detector screen and a sample with a clean surface. The electron gun generates a beam of electrons which strike the sample at a very small angle relative to the sample surface. Incident electrons diffract from atoms at the surface of the sample, and a small fraction of the diffracted electrons interfere constructively at specific angles and form regular patterns on the detector. The electrons interfere according to the position of atoms on the sample surface, so the diffraction pattern at the detector is a function of the sample surface. In the RHEED setup, only atoms at the sample surface contribute to the RHEED pattern.¹⁰⁴ Streaks appear in the place of perfect points when broadened rods (incident beams) intersect the Ewald sphere. Diffraction conditions are fulfilled over the entire intersection of the rods with the sphere, yielding elongated points or ‘streaks’ along the vertical axis of the RHEED pattern. In real cases, streaky RHEED patterns indicate a flat sample surface while the broadening of the streaks indicates small area of coherence on the surface.¹⁰⁵

The dotted pattern in figure 5.6 is the RHEED pattern for the $\text{Si}_{0.7}\text{Ge}_{0.3}$ layer grown at 500 °C and 0.5 Å/s, which means the film is not epitaxial. Polycrystalline films can be expected under this growth condition.



Figure 5.6 RHEED results for 10nm Si_{0.7}Ge_{0.3} growth on 6.5 nm Si buffer layer at 500 °C and 0.5

Å/s.

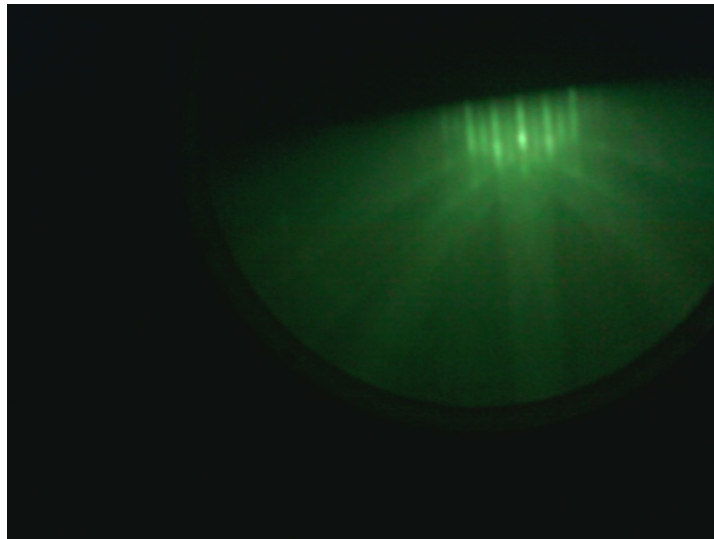


Figure 5.7 RHEED results for 10nm Si_{0.7}Ge_{0.3} growth on 1.8 nm Si buffer layer at 550 °C and 1 Å/s.

Epitaxial growth can be achieved with thinner buffer layer and higher growth temperature. The streaks patterns (shown in figure 5.7) shows good surface reconstruction which means good epitaxy.

5.4 GROWTH CONDITIONS LEAD TO PREFERRED QUANTUM DOTS GROWTH

AFM images of surfaces after 10nm Si_{0.7}Ge_{0.3} growth on a 6.5nm Si buffer layer at 500°C and 1Å/s with different FIB dosages are shown in figure 5.8. No pits were observed for low dosages (figure 5.8 (a) and (b)) and discrete islands only presented at the damage site. These islands are much larger than would be expected from substrate amorphization due to FIB patterning for such a low dosage. The sidewall angles were between 10-16°. As the dosage was increased, double islands started to form at each milled site (figure 5.8 (b)). This may be due to the larger size of the damage zone which supports double nucleation sites.¹⁰⁶ Higher FIB dosage is expected to not only yield deeper damage into the substrate, but also latterly increase the size of the damage zone. As the dosage increased further, the double islands were more distinguishable (figure 5.8 (c)). With the highest dosage tried (figure 5.8 (d)), discrete islands now formed around central pits. The average height of the islands was 5.5 (±1) nm and the outside angle of the islands was 29°. The central pit observed at this dosage is most likely not due to the original FIB topography for this dosage. Instead the pit may form during the chemical etch or by ejection of deposited material from the damage site.

Pit edges then acted as preferential nucleation sites¹⁰⁷ for the islands when the damage was large enough to cause pit formation (<100> direction with respect to pit center). The growth

conditions are also of particular importance, since for these conditions, islanding is limited and only occurs at the damage site. Growth conditions that allowed for increased kinetics would not suppress island growth on the non-patterned regions. Similarly, if the growth kinetics were too low we would expect island formation to be suppressed entirely.

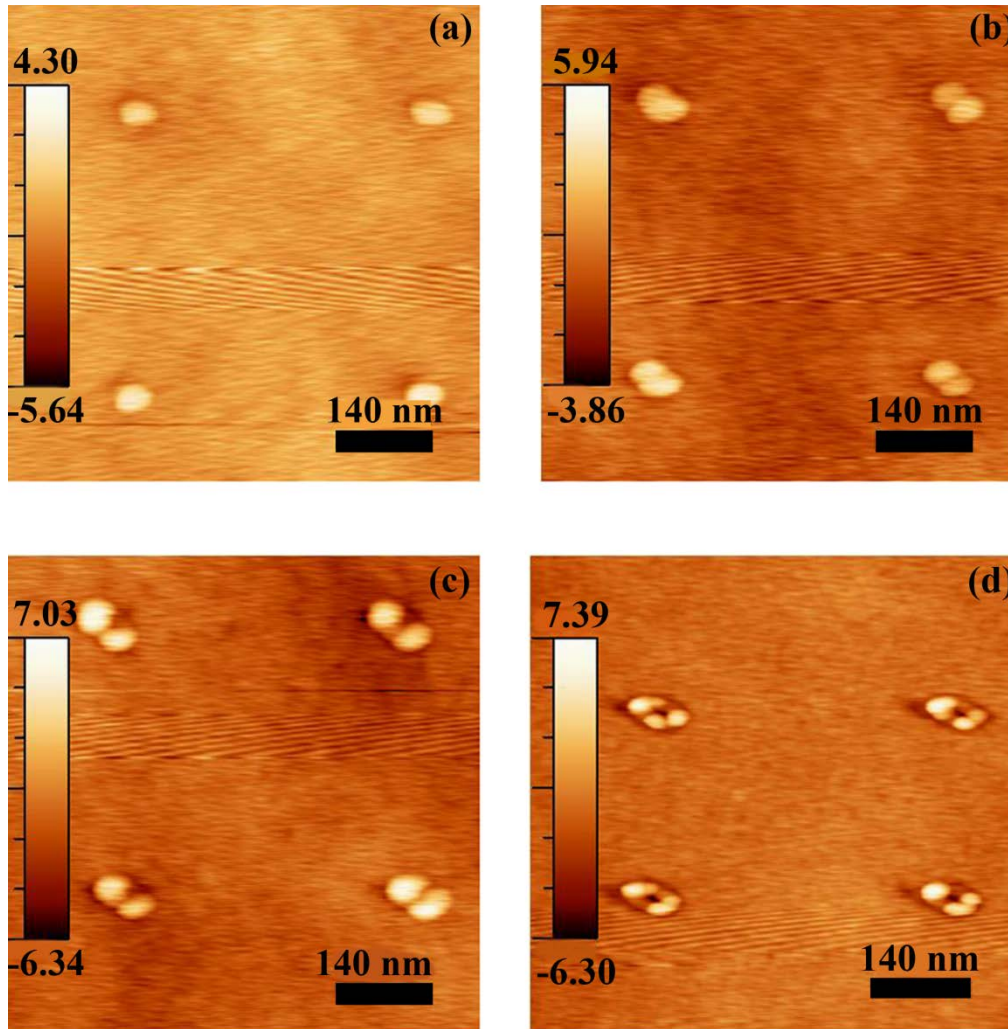


Figure 5.8 AFM 1x1 μm image with edges roughly aligned along the $\langle 110 \rangle$ directions for films deposited on substrates patterned at single points using a 1 pA beam current. The 10nm $\text{Si}_{0.7}\text{Ge}_{0.3}$ were grown on a 6.5nm Si buffer layer at 500°C and $1\text{\AA}/\text{s}$. Pattern dosages were (a) $0.5 \times 10^{15}/\text{cm}^2$. (b) $1 \times 10^{15}/\text{cm}^2$. (c) $3 \times 10^{15}/\text{cm}^2$. (d) $6 \times 10^{15}/\text{cm}^2$.

5.5 GEMANIUM QUANTOM DOTS ON SI SBUSTRATE

The growth of Ge quantum dots on Si substrate is another approach in this experiment. It is carried out using a similar process to the SiGe quantum dots growth. The difference is during the magnetron sputtering step, in which only the Ge target is used. To suppress the Ge quantum dots to grow only in or on the template region, we use a high growth rate for Ge (4 Å/s).

Figure 5.9 shows the Ge quantum dots grown at 500 °C with 65 Å Si buffer layer. The thickness of the Ge thin film is 8 Å and the growth rate is 4 Å/s. From figure 5.9, the size of the Ge quantum dots is about 20 nm to 35 nm and the height is around 5 nm.

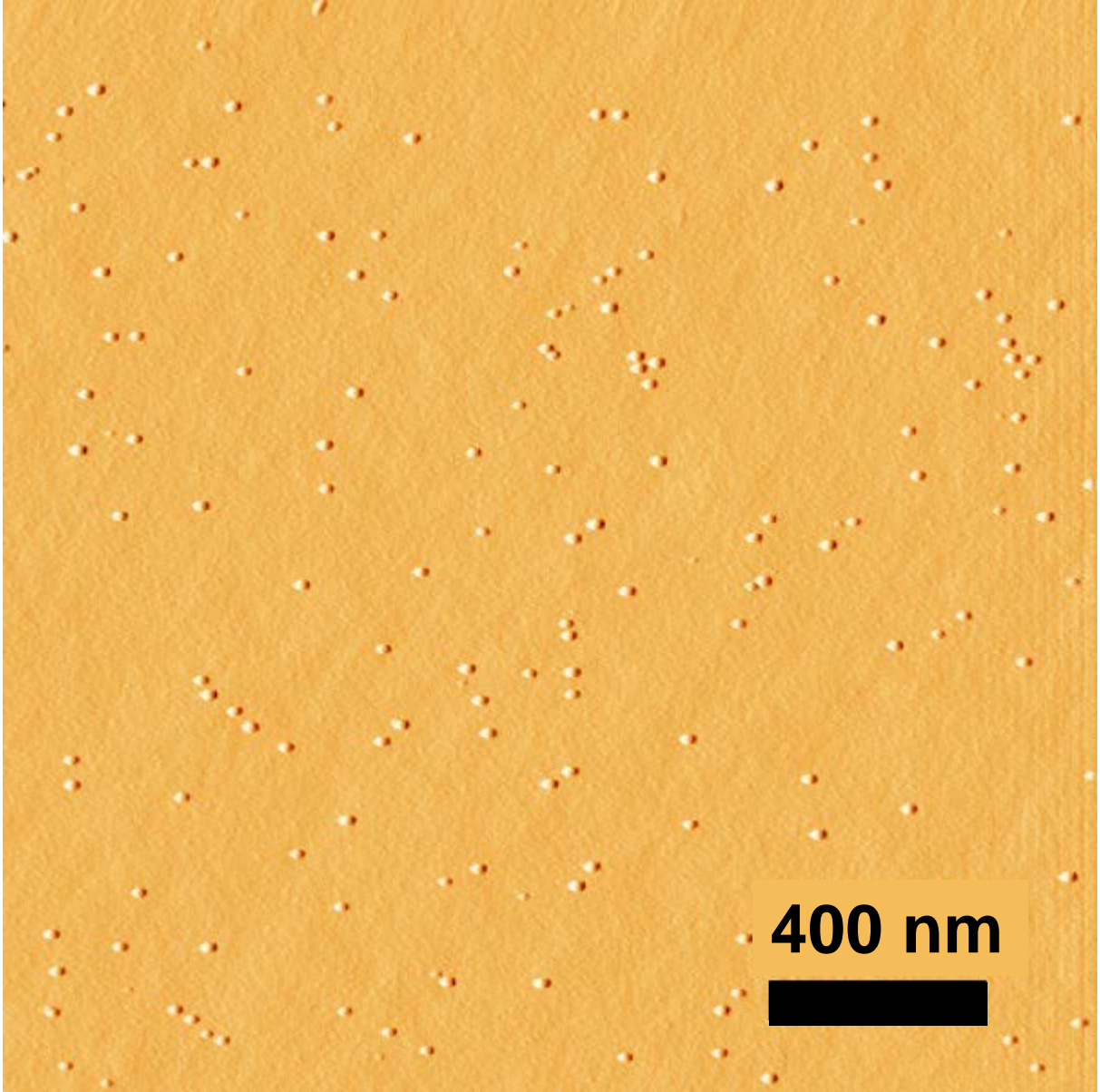


Figure 5.9 AFM of Ge quantum dots in un-patterned region.

The experiment of growing Ge quantum dots on patterned substrate was also investigated. The patterning parameter for the template was 30 kv with 1 pA beam current and the dosage was $20 \times 10^{15}/\text{cm}^2$. The growth condition of Ge quantum dots was still at 500 °C with 65 Å Si buffer layer. The thickness of the Ge thin film was 8 Å and the growth rate was 4 Å/s.

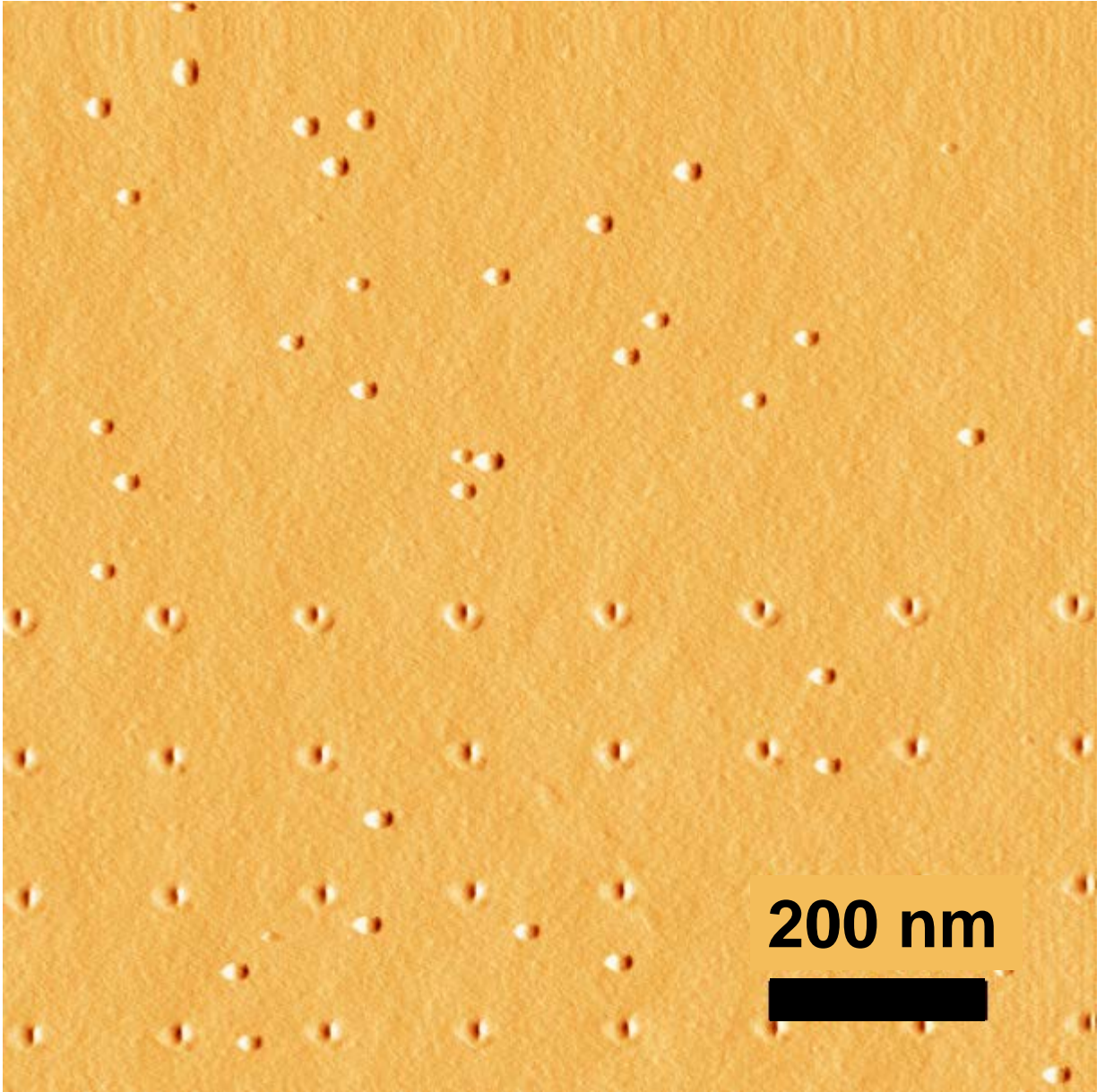


Figure 5.10 Growth of Ge quantum dots in patterned region.

The size of the Ge quantum dots that form on the template was the same as outside the template. The prospective attraction phenomena of larger Ge quantum dots forming at the energetically preferred FIB pattern sites was not observed as expected. The original design of

this experiment was trying to use the FIB to create surface defects on the Si surface. During the sputtering process, the Ge atoms reach the substrate with energy and mobility. To minimize the energy of the whole system (consider “new arrived” Ge atoms and Si substrate), the Ge quantum dots tended to form on or at the edge of the “damaged” sites as we have observed in section 5.3 and 5.4. However, from the results we observed here, that hypothesis can’t explain what happened. In figure 5.10, there was no preference of the location for Ge quantum dots to form. That can be explained in this way: the energy difference between the “damaged” sites and the un-patterned region is very small comparing to the energy of the “new arrived” Ge atoms. Therefore, islanding from occurring everywhere on the surface of the wafer, as opposed to just at the patterned sites is what we obtained at this given conditions.

Lower growth temperature (450 °C) will yield rough surface rather than continuous flat thin film.

(More Ge growth conditions can be found in Appendix A3.)

5.6 CONCLUSIONS FOR SIGE NANOISLANDS

Focused ion beam patterning can be used to influence the growth of SiGe islands deposited by magnetron sputtering, but only under certain growth conditions. However, these growth conditions may not result in single crystal films. By increasing the growth temperature, it appears that single crystal growth based on RHEED pattern analysis is achievable. However, it is still not clear that these conditions will allow for the limited kinetics necessary to suppress islanding from occurring everywhere on the surface of the wafer, as opposed to just at the patterned sites.

Therefore, more experiments are necessary to explore the effect of other growth conditions other than temperature on resulting surface morphology.

6.0 SUMMARY AND FUTURE WORK

As evident from previous sections of the dissertation, successful growth of nanostructure on Si substrates has been demonstrated. However, additional work needs to be done to investigate the different temperature regimes for Ga nanodots growth for better size control. The GaN growth is another topic that also needs to be investigated. It has also been shown through our experiments that the rock-salt structure can be achieved. The effect of the gas ratio, reaction temperature and N source on GaN formation also merits further study. The ultimate goal in growing size and position controllable nanostructure is to tailor them to suit potential applications such as LED devices or nano laser diodes.

6.1 SUMMARY OF RESULTS AND CONCLUSIONS

The ultimate goal for this doctoral dissertation is to understand the underlying mechanisms that yield the best possible conditions for locating controllable nanostructures on Si substrates using a focused ion beam. In the first approach, we were using the implanted Ga directly for nanoisland formation. These experiments allowed us to obtain a fundamental understanding of how the FIB patterning parameters affect the Ga island nucleation and requirements for achieving site specific growth.

Formation of crystallized gallium nanodots on silicon substrates has been achieved with the aid of a focused ion beam system using the gallium ion beam as the source of gallium. There were different ranges of dosages and templates that were used to investigate the size of the Ga nanodots within the trenches. In contrast, Ga nanodots were not detected when the same procedure was repeated using a bit map dot array technique, which could be due to the insufficient area available within the individual dots in the array. The insufficient area means at each patterned site, the total amount of Ga is not enough. Our conclusions at this point are that the Ga nanodots can be observed after one hour vacuum annealing at 600 °C. The concept of a linear relationship between the diameter of Ga nanodots and the dosages or trench width of the patterned area is also demonstrated in our study.

The contrast in HAADF images observed from the trenches indicates that crystallized Ga nanodots have been formed. The lattice fringes in the HRTEM images also provide evidence of crystallized Ga nanodot formation. We also observe a difference in the size of the Ga nanodots when comparing AFM and TEM data. This change could possibly arise from differences in the surface diffusion mechanism of the Ga atoms on the Si substrates that are either crystalline or amorphous. Our experimental observations also agree with the Monte Carlo simulations that were performed using the appropriate parameters.

We have demonstrated that nucleation of gallium nanoislands directly on commercial silicon (001) substrates can be achieved with the aid of a FIB system using the Ga ion beam as the source of gallium. For proper FIB milling conditions, Ga nanoislands can be observed to form after one hour vacuum annealing at 600 °C. A single discrete Ga surface island can be achieved by carefully reducing the pattern size. Preferential chemical wet etching and TEM analysis provide substantial proof of the nanocrystalline Ga formation at the surface of the

silicon. We have also shown that the substantial decrease in accelerating voltage of the Ga ions has little effect on the island nucleation process. These results confirm the feasibility of using the FIB as means of directly forming nanocrystalline islands at specific surface locations on a commercial silicon substrate.

We have also developed a procedure converting these islands to GaN nanodots by recognizing the effect of other growth variables such as the dosage and Ar/N₂ ratio. Detailed TEM analysis is necessary to understand how the resulting structure is influenced by these parameters. We are able to convert the Ga to a rock-salt cubic GaN structure, which has previously be found to form under high pressure conditions, based on TEM diffraction pattern analysis of plan view samples. These results confirm the feasibility of using the FIB as a means of directly forming nanocrystalline islands of Ga-based compounds at specific surface locations on a commercial silicon substrate.

In the third approach, we use the topography of the FIB patterned substrate to attempt to influence island formation during heteroepitaxial growth of SiGe films. We have demonstrated that we believe we can achieve epitaxial growth using sputtering. In further experiments we will seek to understand how growth rate and composition can be used to limit island growth's occurrence at FIB patterned sites.

6.2 FUTURE WORK

The experiments described in this body of work have opened up many exciting avenues for further exploration. As has been shown, there is wide range of potentially useful nanostructures

in the Ga/Si and GaN/Si system to be used in applications like photo detectors or LED devices. However, it is important to know which growth condition will result in the formation of a specific structure and why. The growth window for GaN could be rather wider than what we have discussed in the previous sections. The optical properties of GaN on Si substrates should be measured for potential applications as LEDs in the electronics industry. In addition, the growth of SiGe quantum dots still has open questions need answers. The thickness of Si buffer layer, the effect of higher and lower SiGe alloy growth rate and the combination with different growth temperature deserve further investigation. All of these issues need to be addressed in order to use nanostructures formed by these methods in useful applications.

6.2.1 Formation of Gallium Nitride with different structure and different reaction gas

The results shown in Chapter 4 have demonstrated the formation of GaN with rock-salt structure. As reported in the literature,^{6,46-49,108} most of the devices employ the wurtzite structure of GaN. To achieve that structure, some growth conditions or even FIB patterning parameters need to be changed to explore the possibility to synthesize wurtzite GaN.

First of all, since we have mastered the method to precisely control the location of Ga nanoislands, we can also use rough or Ultra-rough beam conditions (larger beam diameter and larger beam current) in the FIB to scan the substrate surface. In this way, we can control the formation of many islands at one time over a larger area.

Secondly, in all the previous experiment, we only investigated one annealing temperature to enable the Ga atoms to diffuse to the surface to form the Ga nanoislands. We can use different annealing temperatures to observe the diffusion behavior of the Ga atoms to investigate the

possible morphology change in Ga nanoislands. Furthermore, the annealing time is also worth varying. New results may be possible to be observed with longer diffusion time combining with different annealing temperatures.

In the nitridation process, we have only used one fixed reaction temperature and three different gas ratios. To synthesize the wurtzite structure GaN, a higher reaction temperature may be helpful for Ga atoms to overcome the constraints from the preformed Ga nanocrystals. Another bold hypothesis can also to be carried out. We can skip the annealing step and directly load the sample into the vacuum chamber to start the nitridation process after directly taking them out from the FIB. This may also make differences in the final results.

To investigate the formation of GaN, we can try to nitrogenize the Ga in the TEM with the reaction gas as ammonia (NH_3). With the help of in-situ TEM, the change of the crystal structure from doped-Ga to Ga nanoislands and finally to GaN can be recorded. For this step, we can use the same method we used while preparing the plan-view TEM samples with the help of FIB as discussed in section 2.8.3. The sample prepared in this way can be thin enough to be electron transparent and ready for TEM characterization.

Ex-situ characterization of the samples post nitridation can be done using AFM to determine any changes in the surface topography. TEM-EDS (Energy-dispersive X-ray spectroscopy) and SAD measurements can be done to characterize the elemental and structural information of GaN.

6.2.2 GaN optical characterization

As we discussed in chapter 1, there are extensive applications of GaN in various devices. One major area is to use GaN in LEDs or laser diodes. It is therefore very natural to investigate the optical properties of GaN nanostructures. Photoluminescence (PL) studies would be a very helpful tool to obtain the optical properties of GaN. ^{109–113}

The radiation effects can be evaluated by micro-PL and Raman spectroscopic techniques. The refractive-index region can be observed both along the tracks and at the projected range of ions. The PL mapping measurements can reveal the bands at different wavelengths with different lateral and depth distributions. ¹⁰⁹

UV-Visible-NIR Micro-spectrophotometer can be used to perform this characterization in our NFCF lab. It has the ability to measure UV-visible-NIR range transmission, absorbance, reflectance, emission and fluorescence spectra of samples ranging from the sub-micron to well over 100 microns across. And while microspectra are being acquired, the sample may be simultaneously viewed with a high-resolution digital imaging system or through eyepieces.

6.2.3 SiGe and Ge quantum dots growth

Ultra high growth rates like 2.0 \AA/ s with Si can also be tried via the magnetron sputtering system in our collaborator-Dr. Jerry Floro's lab, who is an associate Professor in the Department of Materials Science and Engineering in University of Virginia.

To guide the formation of pure Ge quantum dots in the FIB patterned templates, we can change some parameters in the process. Thinner buffer layer which have shown epitaxial growth

for SiGe can be mimicked in this approach. Since Ge has a larger lattice mismatch than SiGe alloy; we will need to use a lower growth temperature or higher growth rate ($>4 \text{ \AA/s}$) and thinner Ge film thickness (16 \AA) in order to suppress the Ge nanodots formation outside the patterned pit.

AFM topography analysis can be performed on the samples to investigate the formation of SiGe and Ge quantum dots under different dosages and different growth parameters. RHEED (Reflection high energy electron diffraction), TEM and SAD techniques can be employed to characterize the epitaxial growth.

APPENDIX A

SI BUFFER LAYER, SIGE, GE GROWTH CONDITIONS

A.1 SI BUFFER GROWTH CONDITIONS

Table Appendix 1

Height	Base Pressure	Buffer Watts/time/T	Buffer thickness	Si T	Si watts/time	Si thickness	FIB parameters	Results summary
6"	1.6E-09	50W/10min/750	60Å	750	180W/18min/18sec	??	bare wafer	
6"	1.2E-09	50W/11min/750	65Å	N/A	N/A	N/A	bare wafer	very flat
6"	1.9E-09	50W/1min27Sec/750	65Å (GR=0.75Å/s)				patterned	
6"	1.9E-09	N/A	N/A	RT	50W/2hr46min40sec	1400Å	bare wafer	growth rate retest
6"	1.0E-09	50W/7min44Sec/750	65Å (GR=0.14Å/s)	N/A	N/A	N/A	patterned	
6"	1.2E-09	50W/7min44Sec/750	65Å	N/A	N/A	N/A	bare wafer	rough
6"	1.0E-09	50W/7min44Sec/750	65Å	N/A	N/A	N/A		
6"	1.2E-09	50W/7min44Sec/700	65Å	N/A	N/A	N/A	bare wafer	chemical clean without final step, plasma is not stable at 3.0E-3, process prussure is 3.3E-3, AFM data is rough
6"	1.0E-09	50W/7min44Sec/500	65Å	N/A	N/A	N/A	bare wafer	200 degree overnight baking, process pressure is 3.6E-3, AFM data is flat

A.2 SIGE GRWOTH CONDITIONS

Height	Base P	Buffer Watts/timeT	Buffer est	Process	Sige T	Ge watts/Si watts	Time	Film thickness	FIB parameters
5"	1.8E-09	50W/11min/750	65 A		500	10/215	1min/42s	100	patterned
5"	1.2E-09	50W/11min/750	65 A		500	10/215	3min/42sec	200	patterned
5"	1.8E-09	50W/16min/40sec/750	100 A		500	10/250	1min/40sec	100	patterned
5"	2.2E-09	50W/16min/40sec/750	100 A		500	5/215	1min/16sec	50A	patterned
5"	2.3E-09	50W/11min/750	65 A		500	10/215	1hr32min/35sec	5000A	bare water(cleaned)
5"	1.0E-09	50W/7min/44sec/500	65A		500	10/215	1min/51sec	100A	patterned
5"	9.5E-10	50W/7min/44sec/550	65A	0.0038	550	10/215	1min/51sec	100A	patterned
5"	9.5E-10	50W/7min/44sec/500	65A	0.0038	500	5/108	3min/42sec	100A	bare water(cleaned)
5"	1.1E-09	50W/7min/44sec/500	65A	0.0036	500	5/108	3min/42sec	100A	patterned
5"	1.0E-09	50W/7min/44sec/450	65A	0.0033	450	5/108	3min/42sec	100A	patterned
5"	1.2E-09	50W/2min/8sec/550	18A	0.003	550	5/108	3min/42sec	100A	bare water(cleaned)
5"	1.3E-09	50W/2min/8sec/550	18A	0.003	550	10/215	36.8sec	32.9A	bare water(cleaned)
5"	1.5E-09	50W/2min/8sec/550	18A	0.003	550	10/215	111.2sec	100A	bare water(cleaned)
5"	1.3E-09	50W/2min/8sec/550	18A	0.0013	550	10/215	111.2sec	100A	bare water(cleaned)
5"	1.4E-09	50W/2min/8sec/550	18A	0.003	550	5/108	112.sec	50A	patterned(cleaned)
5"	1.7E-09	50W/2min/8sec/550	18A	0.003	550	10/215	55.6sec	50A	patterned(cleaned)

A.3 GE QUANTUM DOTS GRWOTH CONDITIONS

Table Appendix 3 Ge quantum dots growth conditions

Height	Base P	Buffer Watts/time/T	Buffer thickness	Ge T	Ge watts/time	Ge est thickness	FIB parameters	Results summary
6"	1.2E-09	50W/11min/750	65 Å	500	158 W/2 s	8 Å	bare wafer	
6"	1.1E-09	50W/11min/750	65 Å	450	158 W/2 s	8 Å	bare wafer	
6"	1.8E-09	50W/11min/750	65Å	550	158 W/2 s	8 Å	bare wafer	Better than 450, worse than 500 degree
6"	2.4E-09	50W/11min/750	65Å	500	158 W/2 s	8Å	patterned	

BIBLIOGRAPHY

1. M. Kammler, R. Hull, M.C. Reuter, and F.M. Ross, *Appl. Phys. Lett.* 82, 1093 (2003).
2. H. Hojo, T. Mizoguchi, H. Ohta, S.D. Findlay, N. Shibata, T. Yamamoto, and Y. Ikuhara, *Nano Lett.* 10, 4668–4672 (2010).
3. B. Damilano, N. Grandjean, F. Semond, J. Massies, and M. Leroux, *Applied Physics Letters* 75, 962 (1999).
4. S.J. Pearton, J.C. Zolper, R.J. Shul, and F. Ren, *J. Appl. Phys.* 86, 1 (1999).
5. S. Nakamura, *Semiconductor Science and Technology* 14, R27 (1999).
6. X. Jun-Jun, C. Dun-Jun, L. Bin, X. Zi-Li, J. Ruo-Lian, Z. Rong, and Z. You-Dou, *Chin. Phys. Lett.* 26, 098102 (2009).
7. J.L. Gray, R. Hull, and J.A. Floro, *J. Appl. Phys.* 100, 084312 (2006).
8. M. Borgstrom, V. Zela, and W. Seifert, *Nanotechnology* 14, 264–267 (2003).
9. G. Chen, H. Lichtenberger, G. Bauer, W. Jantsch, and F. Schäffler, *Phys. Rev. B* 74, (2006).
10. M. Borgstrom, J. Johansson, L. Samuelson, and W. Seifert, *Appl. Phys. Lett.* 78, 1367 (2001).
11. M. Kammler, R. Hull, M.C. Reuter, and F.M. Ross, *Appl. Phys. Lett.* 82, 1093 (2003).
12. C.K. Hyon, S.C. Choi, S.-H. Song, S.W. Hwang, M.H. Son, D. Ahn, Y.J. Park, and E.K. Kim, *Appl. Phys. Lett.* 77, 2607 (2000).
13. J.L. Gray, R. Hull, and J.A. Floro, *J. Appl. Phys.* 100, 084312 (2006).
14. H. Hojo, T. Mizoguchi, H. Ohta, S.D. Findlay, N. Shibata, T. Yamamoto, and Y. Ikuhara, *Nano Lett.* 10, 4668–4672 (2010).
15. B. Damilano, N. Grandjean, F. Semond, J. Massies, and M. Leroux, *Applied Physics Letters* 75, 962 (1999).
16. S.J. Pearton, J.C. Zolper, R.J. Shul, and F. Ren, *J. Appl. Phys.* 86, 1 (1999).

17. S. Nakamura, *Semiconductor Science and Technology* 14, R27 (1999).
18. J. Xu, D. Chen, B. Liu, Z. Xie, R. Jiang, R. Zhang, and Y. Zheng, *Chinese Physics Letters* 26, 098102 (2009).
19. O. Moshe, D.H. Rich, S. Birner, M. Povolotskyi, B. Damilano, and J. Massies, *J. Appl. Phys.* 108, 083510 (2010).
20. O. Moshe, D.H. Rich, B. Damilano, and J. Massies, *Appl. Phys. Lett.* 98, 061903 (2011).
21. D. Rudloff, T. Riemann, J. Christen, Q.K.K. Liu, A. Kaschner, A. Hoffmann, C. Thomsen, K. Vogeler, M. Diesselberg, S. Einfeldt, and D. Hommel, *Appl. Phys. Lett.* 82, 367 (2003).
22. J.M. Fernandez, L. Hart, X.M. Zhang, M.H. Xie, J. Zhang, and B.A. Joyce, *J Mater Sci: Mater Electron* 7, (1996).
23. I.H. Khan, *J. Appl. Phys.* 44, 14 (1973).
24. C.J. Delerue and M. Lannoo, *Nanostructures: Theory and Modelling* (Springer, 2004).
25. A.I. Nikiforov, V.A. Timofeev, S.A. Teys, A.K. Gutakovsky, and O.P. Pchelyakov, *Nanoscale Research Letters* 7, 561 (2012).
26. R.K. Akchurin, I.A. Boginskaya, N.T. Vagapova, A.A. Marmalyuk, and M.A. Ladugin, *Tech. Phys. Lett.* 36, 724–726 (2010).
27. M.Y. Barabanenkov, *Journal of Applied Physics* 80, 4896 (1996).
28. P.S. Sklad, C.J. McHargue, C.W. White, and G.C. Farlow, *Journal of Materials Science* 27, 5895–5904 (1992).
29. R. Buckmaster, T. Hanada, Y. Kawazoe, M. Cho, T. Yao, N. Urushihara, and A. Yamamoto, *Nano Lett.* 5, 771–776 (2005).
30. J.A. Floro, E. Chason, L.B. Freund, R.D. Twesten, R.Q. Hwang, and G.A. Lucadamo, *Phys. Rev. B* 59, 1990 (1999).
31. F.M. Ross, *Science* 286, 1931–1934 (1999).
32. J. Gray, R. Hull, C.-H. Lam, P. Sutter, J. Means, and J. Floro, *Phys. Rev. B* 72, (2005).
33. P. Sutter and M.G. Lagally, *Phys. Rev. Lett.* 84, 4637 (2000).
34. Y. Du, J.F. Groves, I. Lyubinetsky, and D.R. Baer, *J. Appl. Phys.* 100, 094315 (2006).
35. H. McKay, P. Rudzinski, A. Dehne, and J.M. Millunchick, *Nanotechnology* 18, 455303 (2007).

36. J. Gray, N. Singh, D. Elzey, R. Hull, and J. Floro, *Phys. Rev. Lett.* 92, (2004).
37. J.L. Gray, S. Atha, R. Hull, and J.A. Floro, *Nano Lett.* 4, 2447–2450 (2004).
38. A. Portavoce, R. Hull, M. Reuter, and F. Ross, *Phys. Rev. B* 76, (2007).
39. P. Sutter, D. Groten, E. Muller, M. Lenz, and H. von Kanel, *Applied Physics Letters* 67, 3954–3956 (2009).
40. P. Sutter, E. Müller, S. Tao, C. Schwarz, M. Filzmoser, M. Lenz, and H. von Känel, *Journal of Crystal Growth* 157, 172–176 (1995).
41. P. Sutter, C. Schwarz, E. Muller, V. Zelezny, S. Goncalves- Conto, and H. von Kanel, *Applied Physics Letters* 65, 2220–2222 (1994).
42. P. Sutter, B. Vögeli, E. Müller, H. Von Kaenel, and A. Dommann, *Applied Surface Science* 102, 33–37 (1996).
43. A. Rastelli, M. Kummer, and H. von Känel, *Phys. Rev. Lett.* 87, 256101 (2001).
44. A. Rastelli and H. von Känel, *Surface Science* 532-535, 769–773 (2003).
45. Rastelli A. and von Kanel H., *Surface Science* 515, 493–498 (2002).
46. S.J. Pearton, J.C. Zolper, R.J. Shul, and F. Ren, *J. Appl. Phys.* 86, 1 (1999).
47. G. Fasol, *Science(Washington)* 272, 1751–1751 (1996).
48. S. Nakamura, *Science* 281, 956 (1998).
49. S. Nakamura, *Semiconductor Science and Technology* 14, R27 (1999).
50. X.C. Liu and D.R. Leadley, *J. Phys. D: Appl. Phys.* 43, 505303 (2010).
51. C. Teichert, M.G. Lagally, L.J. Peticolas, J.C. Bean, and J. Tersoff, *Phys. Rev. B* 53, 16334 (1996).
52. J.A. Floro, E. Chason, R.D. Twisten, R.Q. Hwang, and L.B. Freund, *Phys. Rev. Lett.* 79, 3946–3949 (1997).
53. J. Xia, Y. Takeda, N. Usami, T. Maruizumi, and Y. Shiraki, *Opt. Express* 18, 13945–13950 (2010).
54. E. Palange and G. Capellini, *Applied Physics Letters* 68, 2982 (1996).
55. Y.W. Mo, D.E. Savage, B.S. Swartzentruber, and M.G. Lagally, *Phys. Rev. Lett.* 65, 1020 (1990).
56. J.N. Gillet and S. Volz, *Journal of Elec Materi* 39, 2154–2161 (2009).

57. C.A. Volkert and A.M. Minor, MRS bulletin 32, 389–399 (2007).
58. S. Reyntjens and R. Puers, Journal of Micromechanics and Microengineering 11, 287 (2001).
59. Y. Du, J.F. Groves, I. Lyubinetsky, and D.R. Baer, J. Appl. Phys. 100, 094315 (2006).
60. M.Y. Ali, W. Hung, and F. Yongqi, International Journal of Precision Engineering and Manufacturing 11, 157–170 (2010).
61. D.P. Woodruff and T.A. Delchar, Modern Techniques of Surface Science - Second Edition (Cambridge University Press, Cambridge, UK, 1994).
62. A. Ichimiya and P.I. Cohen, Reflection High-Energy Electron Diffraction (Cambridge University Press, 2004).
63. C. Hartfield, M. Hammer, G. Amador, and T. Moore, Microscopy and Microanalysis 16, 16–17 (2010).
64. Y. Kotaka, K. Honda, T. Yamazaki, K. Watanabe, H. Fujisawa, and M. Shimizu, Microsc. Microanal 12, 1352 (2006).
65. J.F. Ziegler, The Stopping and Range of Ions in Solids, First Edition (Pergamon Pr, New York, 1985).
66. H. Wang, G.C. Hartman, J. Williams, and J.L. Gray, Mater. Res. Soc. Symp. Proc. 1228, KK12 (2009).
67. C. Lehrer, L. Frey, S. Petersen, and H. Ryssel, J. Vac. Sci. Technol. B 19, 2533 (2001).
68. J.F. Ziegler, The Stopping and Range of Ions in Solids, First Edition (Pergamon Pr, New York, 1985).
69. P.M. Fahey, P.B. Griffin, and J.D. Plummer, Rev. Mod. Phys. 61, 289 (1989).
70. J.S. Makris, J. Appl. Phys. 42, 3750 (1971).
71. J. Falta, M. Copel, F.K. LeGoues, and R.M. Tromp, Appl. Phys. Lett. 62, 2962 (1993).
72. H. Nakahara and M. Ichikawa, Surf. Sci. 298, 440–449 (1993).
73. J. Ushio, K. Nakagawa, M. Miyao, and T. Maruizumi, Journal of Crystal Growth 201-202, 81–84 (1999).
74. M.Y. Tsai, B.G. Streetman, V.R. Deline, and C.A. Evans, JEM 8, 111–126 (1979).
75. R. Elliman and G. Carter, Nuclear Instruments and Methods in Physics Research 209-210, 663–669 (1983).
76. C.W. White, S.R. Wilson, B.R. Appleton, and F.W. Young, J. Appl. Phys. 51, 738 (1980).

77. A. Portavoce, R. Hull, M. Reuter, and F. Ross, *Phys. Rev. B* 76, 235301 (2007).
78. P. Walker and W.H. Tarn, *CRC handbook of metal etchants* (CRC Press, 1991).
79. Y. Kotaka, K. Honda, T. Yamazaki, K. Watanabe, H. Fujisawa, and M. Shimizu, *Microsc. Microanal* 12, 1352 (2006).
80. J. Ghatak, M. Umananda Bhatta, B. Sundaravel, K.G.M. Nair, S.-C. Liou, C.-H. Chen, Y.-L. Wang, and P.V. Satyam, *Nanotechnology* 19, 325602 (2008).
81. V. Heine, *Journal of Physics C: Solid State Physics* 1, 222 (1968).
82. J.L. Gray, R. Hull, and J.A. Floro, *Appl. Phys. Lett.* 81, 2445 (2002).
83. T. Schupp, T. Meisch, B. Neuschl, M. Feneberg, K. Thonke, K. Lischka, and D.J. As, *Journal of Crystal Growth* 312, 3235–3237 (2010).
84. E. Borsella, M.A. Garcia, G. Mattei, C. Maurizio, P. Mazzoldi, E. Cattaruzza, F. Gonella, G. Battaglin, A. Quaranta, and F. D'Acapito, *Journal of Applied Physics* 90, 4467–4473 (2001).
85. S.A. Almeida, S.R.P. Silva, B.J. Sealy, and J.F. Watts, *Thin Solid Films* 343–344, 632–636 (1999).
86. J. Yanagisawa, H. Matsumoto, T. Fukuyama, Y. Shiraishi, T. Yodo, and Y. Akasaka, *Nuclear Instruments and Methods in Physics Research Section B: Beam Interactions with Materials and Atoms* 257, 348–351 (2007).
87. S. De Rinaldis, I. D'Amico, E. Biolatti, R. Rinaldi, R. Cingolani, and F. Rossi, *Phys. Rev. B* 65, (2002).
88. S. Tanaka, S. Iwai, and Y. Aoyagi, *Applied Physics Letters* 69, 4096–4098 (1996).
89. B. Daudin, F. Widmann, G. Feuillet, Y. Samson, M. Arlery, and J.L. Rouvière, *Phys. Rev. B* 56, R7069–R7072 (1997).
90. L. Samuelson, C. Thelander, M.T. Björk, M. Borgström, K. Deppert, K.A. Dick, A.E. Hansen, T. Mårtensson, N. Panev, A.I. Persson, W. Seifert, N. Sköld, M.W. Larsson, and L.R. Wallenberg, *Physica E: Low-dimensional Systems and Nanostructures* 25, 313–318 (2004).
91. H. Wang and J.L. Gray, *Nanotechnology* 22, 425602 (2011).
92. A. Portavoce, R. Hull, M. Reuter, and F. Ross, *Phys. Rev. B* 76, (2007).
93. M.C. Yoo, T.I. Kim, K. Kim, K.H. Shim, and J. Verdeyen, *Optical and Quantum Electronics* 27, 427–434 (1995).

94. E. Butter, G. Fitzl, D. Hirsch, G. Leonhardt, W. Seifert, and G. Preschel, *Thin Solid Films* 59, 25–31 (1979).
95. H. Xia, Q. Xia, and A.L. Ruoff, *Phys. Rev. B* 47, 12925 (1993).
96. T. Miyazaki, T. Fujimaki, S. Adachi, and K. Ohtsuka, *J. Appl. Phys.* 89, 8316 (2001).
97. Q. Liu, Y. Bando, and J. Hu, *Journal of Crystal Growth* 306, 288–291 (2007).
98. X.M. Teng, H.T. Fan, S.S. Pan, C. Ye, and G.H. Li, *J. Vac. Sci. Technol. A* 24, 1714 (2006).
99. E. Calleja, M.A. Sánchez-García, F.J. Sánchez, F. Calle, F.B. Naranjo, E. Muñoz, U. Jahn, and K. Ploog, *Phys. Rev. B* 62, 16826–16834 (2000).
100. B. Daudin, C. Adelmann, N. Gogneau, E. Sarigiannidou, E. Monroy, F. Fossard, and J.L. Rouvière, *Physica E: Low-dimensional Systems and Nanostructures* 21, 540–545 (2004).
101. W. Kern, *J. Electrochem. Soc* 137, 1887–1892 (1990).
102. Y.W. Mo, D.E. Savage, B.S. Swartzentruber, and M.G. Lagally, *Phys. Rev. Lett.* 65, 1020 (1990).
103. R.B. Marcus and N.J. Soucek, *Vacuum* 18, 148 (1968).
104. W. Braun, *Applied RHEED: Reflection High-energy Electron Diffraction During Crystal Growth* (Springer, 1999).
105. O. Auciello and A.R. Krauss, *In Situ Real Time Characterization of Thin Films: Edited by Orlando Auciello, Alan R. Krauss* (Wiley-IEEE, 2001).
106. A. Portavoce, R. Hull, M. Reuter, and F. Ross, *Phys. Rev. B* 76, (2007).
107. P. Sutter, D. Groten, E. Müller, M. Lenz, and H. von Känel, *Appl. Phys. Lett.* 67, 3954 (1995).
108. B. Damilano, N. Grandjean, F. Semond, J. Massies, and M. Leroux, *Applied Physics Letters* 75, 962 (1999).
109. T. Souno, *Nuclear Instruments and Methods in Physics Research Section B: Beam Interactions with Materials and Atoms* 210, 277–280 (2003).
110. M. Tchernycheva, C. Sartel, G. Cirlin, L. Travers, G. Patriarche, J.C. Harmand, L.S. Dang, J. Renard, B. Gayral, L. Nevou, and others, *Nanotechnology* 18, 385306 (2007).
111. H. Zhou, S. Chua, K. Zang, L. Wang, S. Tripathy, N. Yakovlev, and O. Thomas, *Journal of Crystal Growth* 298, 511–514 (2007).
112. K. Sebald, H. Lohmeyer, J. Gutowski, T. Yamaguchi, and D. Hommel, *phys. stat. sol. (b)* 243, 1661–1664 (2006).

113. T. Onuma, A. Uedono, H. Asamizu, H. Sato, J.F. Kaeding, M. Iza, S.P. DenBaars, S. Nakamura, and S.F. Chichibu, *Applied Physics Letters* 96, 091913 (2010).